CuInS$_2$ Thin Films for Photovoltaic: RF Reactive Sputter Deposition and Characterization

Dissertation

Yunbin He

JUSTUS-LIEBIG-
UNIVERSITÄT
GIESSEN

CuInS$_2$ Thin Films for Photovoltaic:
RF Reactive Sputter Deposition and Characterization

vorgelegte Dissertation

von

Yunbin He

im Fachbereich 07 (Physik) der Justus-Liebig-Universität Gießen

zur Erlangung des akademischen Grades Dr. rer. nat.

Berichterstatter: Prof. Dr. Bruno K. Meyer

Prof. Dr. Claus-Dieter Kohl

I. Physikalisches Institut

Justus-Liebig-Universität Gießen

Gießen, Mai 2003

Contents

Publications.. 111

Curriculum vitae 115

Acknowledgements... 117

1   Introduction

As the environmental and energy resource concerns have become more and more imperative, great efforts have been put in the development of renewable energy resources, among which photovoltaic solar power is the most desirable one and holds great potential and promise.

Photovoltaic (PV) solar power converts directly the sunlight to electricity by using the photovoltaic effect, which was discovered in 1839 by Edmond Becquerel [1]. Compared to nonrenewable sources such as coal, gas, oil, and nuclear, the advantages of the PV solar power are clear: its source is entirely safe, free of charge, and non-exhausting, given a no-end life of the sun, and the power generation is totally non-polluting, i.e., causing no changes to the environment when generating power. Even compared to other renewable energy sources such as wind power, water power, and solar thermal power, PV solar power holds obvious advantages. Whereas wind and water electrical power generation, relying on turbines to turn generators with moving parts, are noisy and require maintenance, PV systems, with no moving parts, require virtually no maintenance, and have cells that can last for decades. In addition, the exclusive modular nature of PV enables designers to build PV systems with various power output in a distributed fashion, and allowing the power generation to keep in step with growing needs without having to overbuild generation capacity as is often the case with conventional large scale power systems. Since its first commercial use in powering orbital satellites in the 1950s, PV has been widely used in space and on the earth for several decades. Today's PV market is about 381 MW (in 2001) corresponding to a value of over US$1.4 billion [2].

Crystalline silicon was first used to produce PV cells (also known as solar cells), and still dominates the PV market today. This is mostly due to a well-established knowledge on silicon material science and engineering, an available abundant supply of silicon raw material, and the advantages of low ecological impact but high efficiencies. However, the relatively high price of crystalline silicon material, and additionally its too low optical absorption ($\sim 10^2$ cm^{-1}), due to an indirect transition, requiring a much larger raw material consumption and a complicated manufacturing, lead to a high installation cost for crystalline silicon-based PV technology. From this point of view, the PV power generation is not competitive in most urban areas where conventionally generated power is readily available. A substantial reduction of PV production costs is expected from the development of thin film solar cells, in which highly absorption layers with a few micrometer thickness can be produced by economical, high-volume manufacturing techniques. This lays down the background for the extensive research interest in materials

suitable for thin film solar cells. At present, several manufacturing facilities based on a-Si, CdTe, and $CuInSe_2$ are in the pilot-line stage. The latest developments in the field of thin film solar cells can be found in the recently published review articles [3-5].

I-III-VI$_2$ compounds, especially Cu-chalcopyrite thin films have played a major role in thin film PV technology. Typical Cu-chalcopyrite-based absorber materials are $CuInSe_2$, $CuInS_2$, $CuGaSe_2$ and their alloys with bandgaps ranging from 1.05 to 1.7 eV, which is favorable for absorbing the solar radiation. The high absorption coefficient of these materials of almost $10^5\,cm^{-1}$ assures a complete absorption of the incident photon flux in an absorber layer as thin as a few microns. Polycrystalline chalcopyrite-based thin film solar cells have recently reached conversion efficiencies as high as 18.8%, which is the highest value so far achieved for any polycrystalline thin film solar cell. This record device consists basically of a coevaporation-deposited p-type $Cu(InGa)Se_2$ absorber layer, an n-type thin CdS buffer, and an n-type ZnO window layer [6].

Compared to other selenium chalcopyrites such as $CuInSe_2$, $CuInS_2$ is even more favorable for PV solar power. Substituting the problematic selenium by non-toxic sulfur, $CuInS_2$ is more environment-friendly than $CuInSe_2$. The open circuit voltage of $CuInS_2$ solar cells is theoretically higher than that of $CuInSe_2$ and $Cu(InGa)Se_2$-based solar cells. Its photo current is lower, which is advantageous for the serial connection of multiple cells in a module. Due to a superior bandgap of about 1.5 eV, matching almost ideally to the solar spectrum, $CuInS_2$ has in principle the highest conversion efficiency among the Cu-chalcopyrite-based solar cells [7, 8]. However, the efficiency of $CuInS_2$ solar cells is so far limited by the open circuit voltage that is far below the theoretical value. The best conversion efficiency for polycrystalline $CuInS_2$ solar cells achieved to date is 12.7% [9, 10], considerably lower than that of cells based on $CuInSe_2$ (14.8%) [11] and $Cu(InGa)Se_2$ (18.8%) [6]. To improve further the solar cells' efficiencies a better understanding on the absorber itself is essential. Whereas $CuInSe_2$ has been widely studied for more than two decades, $CuInS_2$, especially as a thin film, has just attracted more attention recently. Great potential but limited material knowledge motivated us to focus the present study on $CuInS_2$ thin films.

Up to now, a number of methods have been performed to produce $CuInS_2$ films, including a rapid thermal process [10], single source evaporation [12], coevaporation from elemental sources [13], sulfurization of metallic precursors [14], chemical vapor deposition [15], sputtering [16], electrodeposition [17], and spray pyrolysis [18], etc. Among them, the sputtering technique holds in principle the advantage of simple and flexible control of the film stoichiometry over a large scale at relatively low cost. Its great potential for industrial application drove us to choose reactive sputtering as the technique for $CuInS_2$ thin film deposition. Usually the deposition of $CuInS_2$ film by sputtering consists of two steps, sputtering a precursor first, then, annealing or sulfurizing the sputtered precursor in a

second step. Simplification of the process is one of the key issues for industrial application. In the present study, we demonstrate that $CuInS_2$ films can be produced in one step by radio frequency (RF) reactive sputtering with a Cu-In alloy target and H_2S gas.

Normally a better understanding of the fundamental material properties can be expected from high-quality single-crystalline materials. However, it is well known that the controlled growth of high quality single crystals is a priori difficult for ternary compounds, and is additionally complicated by high temperature phase transitions that occur in many chalcopyrite compounds [19]. It is therefore of great importance to achieve crystalline $CuInS_2$ films e.g. by epitaxial growth. However, up to now such attempts have scarcely been reported in the literature. With the molecular beam epitaxy (MBE) technique Metzner and Hahn successfully grew $CuInS_2$ films heteroepitaxially on sulphur-terminated Si (111) and Si (100) [19, 20], while Hunger achieved epitaxial growth of $CuInS_2$ on hydrogen-terminated Si (111) [21]. In this work, we have succeeded in, to the best of our knowledge, the first epitaxial growth of $CuInS_2$ films on (0001)-sapphire by RF reactive sputtering.

This thesis is organized as follows.

Chapter 2 starts with an introduction of the established crystalline structure of $CuInS_2$, followed by a brief summary of the known physical properties such as electrical, electronical, optical properties of $CuInS_2$ material.

The working principle of the RF reactive sputter technique and the specific setup used in this work will shortly be described in *Chapter 3*.

Chapter 4 outlines the characterization techniques employed in this work, that is, photoemission spectroscopy (XPS and UPS), secondary ion mass spectrometry (SIMS), X-ray diffraction (XRD), X-ray reflectometry (XRR), transmission electron microscopy (TEM), atomic force microscopy (AFM), and scanning electron microscopy (SEM) for surface, structure and morphology characterization, and optical transmission and Hall effect measurement for optical and electrical properties, respectively.

As a preliminary step, we used a Cu-In inlay target for sputtering, which leads to films with in general good structural properties but strong deficiency in the In content. By using a Cu-In alloy target instead, one-stage growth of stoichiometric $CuInS_2$ films by RF reactive sputtering has been achieved, as reported in *Chapter 5*. To optimize the sputtering process, in section 5.1, we first investigated systematically the influence of the sputter parameters on the film properties. Section 5.2 focuses on the characterization of the surface of the sputtered films, its knowledge is significant for achieving high-efficiency $CuInS_2$ film solar cells. Although stoichiometric $CuInS_2$ films can be sputtered in one step, it is shown in section 5.3 that post-growth annealing improves significantly the properties of the sputtered films, and that the surface segregation of Cu_xS can be effectively removed by post-growth chemical etching. Section 5.3 presents the post-treatment effects on the $CuInS_2$ film properties.

In ***Chapter 6***, the present work is highlighted by the success of epitaxial growth of $CuInS_2$ films on crystalline (0001)-sapphire substrates. The structural characteristics of the sputtered thin $CuInS_2$ epilayers have been investigated, with special emphasis on elucidating the origin for the epitaxial growth (section 6.1). With a thin epilayer as buffer, thick $CuInS_2$ films grow quasi-epitaxially on sapphire. While the out-of-plane ordering of the films is significantly enhanced, the in-plane alignment shows a multi-domain feature in contrast to films sputtered without the buffer. Section 6.2 discusses the structural properties of such thick films with special efforts on illustrating the role of the thin buffer layer. The TEM characterization of the sputtered quasi-epitaxially grown $CuInS_2$ films is presented in section 6.3.

Finally, a brief summary and an outlook for future work are drawn in English in ***Chapter 7***, and in German in ***Chapter 8***, respectively.

2 CuInS₂ materials and properties: a brief review

CuInS₂ belongs to the family of ternary chalcopyrite compounds. In the early seventies a comprehensive review of chalcopyrite compounds was first provided by Shay and Wernick [1]. Whereas the earlier works were mainly on single crystalline specimens, motivated by their potential for non-linear optical applications, visible-light emitters, and photodetectors [2-5], the more recent experimental studies have been mostly devoted to thin films, due to their great perspectives for large area PV modules. The present work concentrates on the RF sputtering deposition and characterization of structural and physical properties such as electronical, optical, and electrical properties of CuInS₂ thin films, aiming to establish a sputtering-based method suitable for producing device grade CuInS₂ absorber films. In this chapter, a brief introduction to the well-established structural and physical properties of the material is provided as a basis for the analyses of the sputtered films, as will be presented in the following chapters in this study.

2.1 Crystal structure

The ternary chalcopyrite compounds $A^{I}B^{III}X^{VI}_2$ (A=Cu, Ag; B=Al, Ga, In, Tl; and X=S, Se, Te), similar with their isoelectronic II-VI binary analogues, derive from the tetrahedrally bounded class IV semiconductors. In the diamond structure of the class IV semiconductors, each atom has four neighbors situated at the corners of a regular tetrahedron bonded by hybridized sp^3 bonds. In Fig. 2.1(c), a unit cell of CuInS₂ of the chalcopyrite structure is illustrated, in comparison with the diamond (a) and zincblende (b) crystal structures. By arranging two units along a diagonal line through the cubes and shifting them, in terms of the basis vectors by (a/4, a/4, a/4) the diamond structure is created. The zincblende structure can be regarded as a superlattice structure of diamond, with one sublattice occupied by cations and the other by anions. In a ternary chalcopyrite structure whereas the anions remain at their sites the cations are furthermore replaced by one cation of lower valence (A) and one cation of higher valence (B) in the arrangement as shown in the figure.

The unique properties of the chalcopyrites are related to basically three structural differences with respect to the zincblende structure. Firstly, there are two cation sublattices

rather than one, leading to the existence of two basic chemical bonds *A-X* and *B-X*, in general with unequal bond lengths $R_{AX} \neq R_{BX}$. Secondly, the unit cell is tetragonally distorted with a distortion parameter $\eta \equiv c/2a \neq 1$. Thirdly, the anions are displaced from the ideal tetrahedral site by an amount *u* [6]. In the specific case of CuInS$_2$ the Cu-S bond length is 0.2335 nm, whereas the In-S one is 0.2464 nm [7]. The sulfur atom moves away from the In atoms towards the Cu atoms, resulting in a stretched unit cell with $\eta \equiv c/2a =$ 1.0065, associated with an anion displacement parameter $u = 0.214$ [8]. The structural and electronic properties of the chalcopyrites are governed by the added structural (η, *u*) and chemical ($A \neq B$) degrees of freedom relative to their binary analogues [6]. Structural and optical properties of some typical chalcopyrite materials are compared in table 2.2.
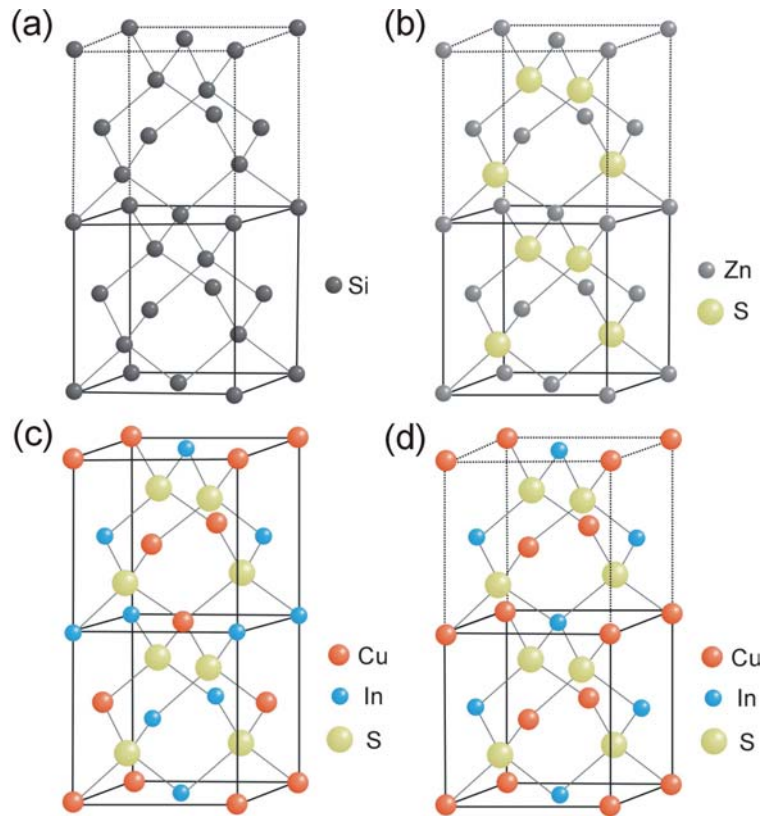
Fig. 2.1. Structures of (a) diamond Si, (b) zincblende ZnS, (c) chalcopyrite CuInS$_2$, and (d) CuAu ordered CuInS$_2$. Double unit cells are shown for (a) diamond Si, (b) zincblende ZnS, and (d) CuAu ordered CuInS$_2$, in comparison with the unit cell of chalcopyrite CuInS$_2$.

The reduced symmetry, due to two kinds of cations, leads to a primitive cell of eight atoms in the chalcopyrite structure compared to a primitive cell of two atoms in the zincblende structure. The Bravais lattice of the chalcopyrite is body centered tetragonal, belonging to space group $I\bar{4}2d$ [9]. Compared to the face centered cubic Bravais cell of

the zincblende the unit cell is doubled along the crystal c axis. At room temperature, the ternary compounds $A^{I}B^{III}X^{VI}_{2}$ stabilize in chalcopyrite, however, they may crystallize in zincblende structure at high temperature (975-1047°C) where the different cations are distributed randomly [10].

The polymorphism is referred to the phenomenon that a solid with the same composition can appear in different crystal structures under different thermodynamical conditions. A set of polytypes of the chalcopyrite structure were theoretically constructed such that the electron counting rule is obeyed. By first-principles calculations Wei *et al*. determined the formation energies and band structures of CuInSe$_2$ and CuInS$_2$ polytypes [11, 12]. It was shown that the CuAu-like ordered structure is the most likely to occur. An exceedingly small formation energy difference ΔE_{form}= -1.95 meV/atom was found between chalcopyrite and CuAu-like phases of CuInS$_2$. Similar results were obtained for CuInSe$_2$ where ΔE_{form}= -2.05 meV/atom. It was predicted that CuAu-like phases coexist in nominally chalcopyrites CuInS$_2$ and CuInSe$_2$. Band gap energies are affected slightly by the transition from chalcopyrite (CH) to polymorphous structures. Calculations resulted in E_{g} (CH)-E_{g} (CuAu) = 30 meV for CuInS$_2$ and in E_{g} (CH)-E_{g} (CuAu) = 46 meV for CuInSe$_2$. This suggests furthermore that formation of polytypes in these compounds has insignificant effect on their electrical and optical properties.

An illustration of the CuAu-like structure is given in Fig. 2.1 (d) in comparison to the chalcopyrite structure. The anion sublattice is conserved in the CuAu structure and the cation order is changed such that the A_2B_2 coordination is conserved. The lattice type of the CuAu-like structure is primitive tetragonal, corresponding to space group $P\bar{4}m2$ [13]. In table 2.1, chalcopyrite CuInS$_2$ is compared to typical materials of diamond and zincblende structures such as Si and ZnS, in terms of crystal structure, space group, Bravais lattice, and lattice constants.

Table 2.1 Summary of crystal structure, space group, Bravais lattice, and lattice constants of CuInS$_2$ in the Zincblende, chalcopyrite, and CuAu-like phases, in comparison with diamond Si and zincblende ZnS.

Material	Crystal Structure	Bravais Lattice	Space Group	Lattice Constants (nm)
Si	Diamond	fcc	$Fd3m$ (227)	$a=b=c=$ 0.543 [14]
ZnS	Zincblende	fcc	$F\bar{4}3m$ (216)	$a=b=c=$ 0.5406 [15]
CuInS$_2$	Zincblende	fcc	$F\bar{4}3m$ (216)	$a=b=c=$ 0.551 [16]
	Chalcopyrite	bc-tetragonal	$I\bar{4}2d$ (122)	$a=b=$ 0.5523 [8] $c = 1.1133$ $c/2a = 1.0079$
	CuAu-like	primitive tetragonal	$P\bar{4}2m$ (111)	$a=b\approx c$ [13] $c/a < 1$

2.2 Physical properties

2.2.1 Electronic and optical properties

The electronic band structures of the typical Cu-based ternary chalcopyrite semiconductors including $CuInS_2$ were theoretically studied by Jaffe and Zunger using a density-function formalism and a first-principles all-electron band-structure approach [6, 17]. It has been concluded that the band gaps of Cu-III-VI_2 chalcopyrites are controlled essentially by two factors. The first one is a pure structural factor, caused by the tetragonal distortion, $\eta = c/2a \neq 1$, and anion displacement from the ideal tetrahedral site, $u \neq 1/4$, occurring in the chalcopyrite structure. These parameters, particularly u, determine the band gap in the system. Even a small increase of u from its ideal zincblende value results in a substantial ionic polarization of the bonds and consequently in a remarkable increase of the band gap. The effect of this factor in shown in table 2.2 where u is listed together with the band gap energies of six typical Cu-III-VI_2 compounds.

The second one is an electronic factor. A great influence of the Cu $3d$ states on the valence band was found for Cu-III-VI_2 chalcopyrites. These states hybridize with the p states of the group VI components. As the d states are found in the upper half of the valence band they are responsible, in part, for the reduction of the band gap.

Table 2.2. List of the lattice constants a and c, the tetragonal distortion parameter $\eta = c/2a$, the anion displacement parameter u, and the observed lowest bandgaps at room temperature for typical Cu-III-VI_2 compounds [6, 17].

Ternary Compound	$a = b$ (nm)	c (nm)	η	u	E_g (eV)
$CuInS_2$	0.5523	1.1118	1.0065	0.214	1.53
$CuInSe_2$	0.5784	1.1614	1.004	0.224	1.04
$CuGaSe_2$	0.5614	1.1032	0.9825	0.250	1.68
$CuAlSe_2$	0.5602	1.0946	0.977	0.269	2.71
$CuGaS_2$	0.5356	1.0433	0.974	0.275	2.43
$CuAlS_2$	0.5334	1.0444	0.979	0.275	3.49

A schematic band structure of $CuInS_2$ is shown in Fig. 2.2, with notation of the contributions of the atomic orbitals. The valence band is separated into two parts, with the upper part reaching 5 eV and the lower one located around 7 eV. The Cu $3d$ and S $3p$ orbitals from the Cu-S bond contribute to the upper valence band whereas the S $3p$ and In $4p$ from the In-S bond form the lower valence band. At around 12 eV a band is built from S $3s$ states and a narrow band is set up near 17 eV by In $4d$ orbitals. The conduction band is

formed by S $3p$ and In $5s$ orbitals [6]. This theoretical calculation of the band structure of CuInS$_2$ is in good agreement with the experimental results of X-ray photoemission spectroscopy in respect of the valence band structure [18, 19]. However, it underestimates the optical band gap relative to the experiment.
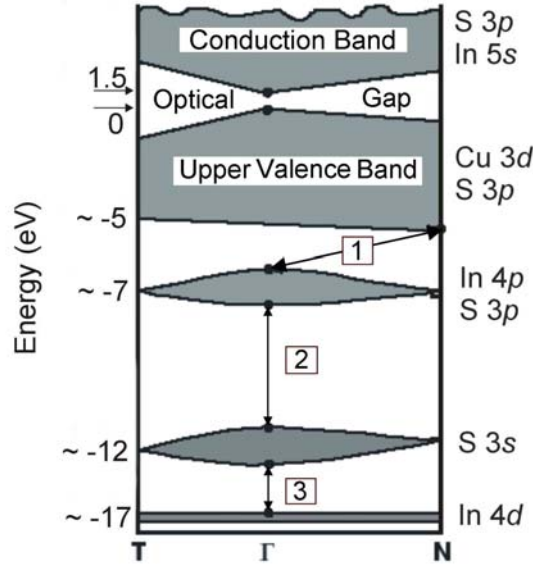

Fig. 2.2. Schematic band structure of CuInS$_2$, with indication of contributions of the atomic orbitals and the corresponding energy levels. Shade areas denote the major subbands, and the boxed numbers mark the three internal gaps [6].

Very recently, a detailed experimental work on optical functions and electronic structure of CuInS$_2$ crystals was carried out by Alonso *et al.* using spectroscopic ellipsometry [20]. A more realistic band structure based on experiments was proposed there with assignments for the transitions observed in the optical range. In addition, optical parameters such as refraction index *n* and extinction coefficient *k* can be found there. In the present study, we consider the optical properties of the sputtered CuInS$_2$ films mainly on bandgap and absorption coefficient, which are essential for absorbing the solar radiation.

CuInS$_2$ is a direct semiconductor. Whereas bandgaps of 1.55 and 1.53 eV were found for bulk single crystals at low (2 K) and room temperature, respectively, band gaps varying between 1.38 and 1.55 eV were reported for CuInS$_2$ thin films at RT depending on different deposition techniques used [1, 21-26]. As is normally expected for semiconductors, the bandgap of CuInS$_2$ films decreases with increasing temperature and can be characterized over the temperature range 300-77 K according to the relation

$$E_g = E_{g0} - \beta T^2 /(T + \alpha) \qquad (2.1)$$

with the initial bandgap E_{g0}=1.62 eV, two constants α =231.54 K and β = 4.3×10^{-4} eV/K, respectively [26]. Around the fundamental absorption edge, CuInS$_2$ has an absorption coefficient between 10^4 to 10^5 cm^{-1}, it can thus absorb the incident light with photon energies higher than the bandgap within a few microns.

2.2.2   Electrical properties

A number of studies on the electrical properties of CuInS$_2$ bulk single crystals and thin films have been reported [27-32]. Unlike its binary II-VI analogues that are normally *n*-type, CuInS$_2$ can be made both *n*- and *p*-type, depending upon its composition, i.e., deviation from molecularity and stoichiometry, defined as [Cu]/[In]-1 and 2[S]/([Cu]/3[In])-1, respectively [33]. It was generally observed that for CuInS$_2$ single crystals good *p*-type behavior (ρ ~1-5 Ωcm, μ ~ 15-20 cm^2/Vs) could be obtained by annealing in a sulfur overpressure, and good *n*-type characteristics (ρ ~1 Ωcm, μ ~ 100-200 cm^2/Vs), by annealing in indium or Cu + In with a minimum S pressure [27, 28]. Similar behavior was observed for CuInS$_2$ films. Excess-sulfur films were generally *p*-type while sulfur-deficient and indium-rich films were *n*-type [32].

Table 2.3. Summary of the defect levels of donors and acceptors reported for CuInS$_2$.

Defect nature	Defect assignment	Ionization energy (eV)	Refs
Acceptor	V$_{Cu}$	0.10	[34-37]
Acceptor	V$_{In}$	0.15	[10, 28, 38-40]
Donor	V$_S$ (or In$_{Cu}$)	0.035	[35, 38-41]
Donor	In$_i$ (or In$_{Cu}$)	0.072	[38, 39]
Donor	In$_{Cu}$	0.145 (0.16)	[33, 35]

The observed behavior of the conducting type of CuInS$_2$ can be understood based on the predicted defect energies and on the ternary Cu-In-S phase diagram. In table 2.3, the defect levels of donors and acceptors reported for CuInS$_2$ are summarized. A schematic Cu-In-S ternary phase diagram indicating the expected defects and majority-carrier type in the region around stoichiometric CuInS$_2$, derived from the Cu-In-Se system [42], is shown in Fig. 2.3. S-rich films containing both Cu and In vacancies (acceptors) should yield strongly *p*-type films. In-rich layers with a sulfur deficiency should be dominated by both antisite (In-on-Cu-site) donor defects and S vacancies (also donors), yielding the observed, highly conductive *n*-type layers. In Cu-rich films with sulfur contents near the pseudobinary tie line, antisite (Cu-on-In-site) acceptor defects and acceptors contributed by In vacancies are predominant, leading to a strong *p*-type conducting as observed. On the

other hand, In-rich layers with sulfur contents near the pseudobinary tie line, governed by antisite (In-on-Cu site) donor defects and Cu vacancies (acceptors), two oppositely charged defects, may be expected to behave, heavily compensated, intrinsic or high-resistivity *n*- or *p*-type conducting. In table 2.4, the electrical transport data of $CuInS_2$ single crystals and thin films reported so far are collected in terms of resistivity, carrier concentration, and Hall mobility.
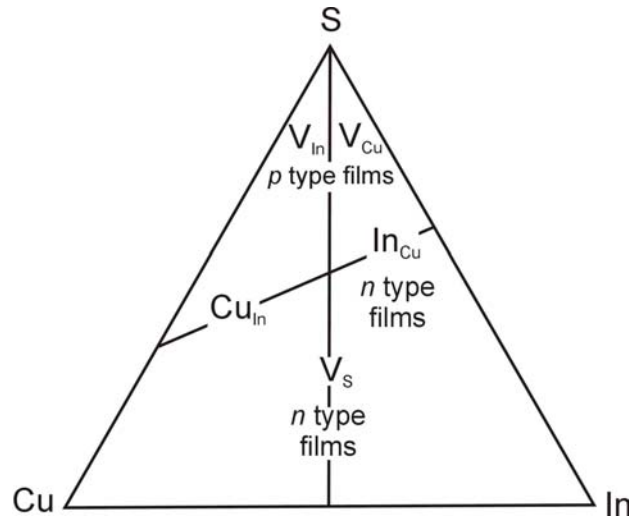

Fig. 2.3. A schematic Cu-In-S ternary phase diagram indicating the expected defects and majority-carrier type in the region around stoichiometric CuInS2, derived from the Cu-In-Se system [42].

Table 2.4. Summary of electrical transport data, such as resistivity, carrier concentration, and Hall mobility, reported for $CuInS_2$ single crystals and thin films.

	Single crystals			Films		
	ρ (Ωcm)	*n,p* (cm^{-3})	μ (cm^2/Vs)	ρ (Ωcm)	*n,p* (cm^{-3})	μ (cm^2/Vs)
n-type	1	3.7×10^{12}-3.5×10^{17}	100-200	0.01-4.9×10^4	4.0×10^{12}-10^{19}	0.032-240
p-type	1-5	5.2×10^{15}-1.0×10^{17}	15-20	0.01-500	10^{13}-10^{20}	0.025-95

3 Radio frequency sputtering: principle and film deposition

As outlined in the introduction, so far, various methods have been performed to produce CuInS$_2$ (CIS) films, including a rapid thermal process [1], single source evaporation [2], coevaporation from elemental sources [3], sulfurization of metallic precursors [4], chemical vapor deposition [5], sputtering [6], electrodeposition [7], and spray pyrolysis [8], etc. Compared to other techniques, sputtering has, in principle, the advantage of simple and flexible control of the film stoichiometry over a large scale at relatively low cost. In practice, the sputtering technique has already been utilized to produce a wide range of functional materials in industry. In this study, we therefore choose reactive sputtering technique for the deposition of CIS thin films. In the present chapter, we first introduce briefly the basic working principle of RF reactive sputtering and the specific setup used in this work, then describe the typical sputter parameters for the deposition of CIS films.

3.1 Sputtering principle and apparatus

Sputter deposition is one of the physical vapor deposition (PVD) techniques. In the basic sputtering process, the source material, named target, is bombarded by energetic positive ions (inert gas such as argon ions) generated in a glow discharge plasma situated in the front of the target. The bombardment process causes the removal, i.e., "sputtering", of target atoms, which may then condense in a thin film on a desired substrate. The positively charged gas ions from the plasma are attracted and accelerated towards the target by the electric field obtained as a result of applying a negative potential on the target with respect to the substrate electrode. Thus the source electrode for the target is known as cathode, and the substrate electrode anode.

If the applied potential between the cathode (target) and anode (substrate) is constant with time, the process is called DC (direct-current) sputtering, by which highly electrical conductive materials like metallic films can be well-deposited. It is, however, hardly possible to deposit insulating films by DC sputtering, since the poor conductivity of the target material leads to accumulation of positive charges on the target (cathode), which in turn eliminates the intentionally applied negative potential on the target. For deposition of insulating films, RF sputtering is designed, which avoids the positive charging on the

target by applying an alternating potential instead. If, during the sputter process, in addition to the inert sputtering gas (working gas), a reactive component (e.g. O_2 or N_2) is introduced, we generally define the process – RF reactive sputtering, which is just the case for the present study.
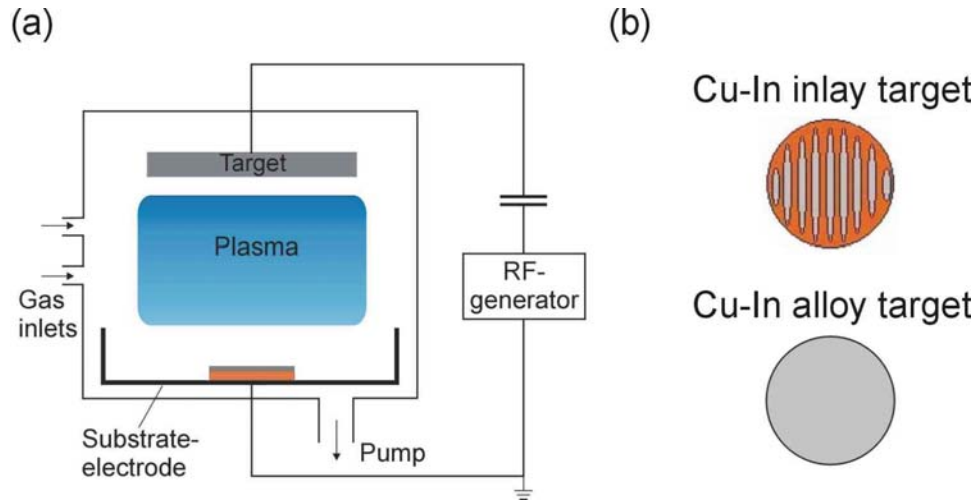

Fig. 3.1. Schematic representations of (a) the RF reactive sputter system, and (b) the two targets used in this study, a Cu-In inlay target (Cu: red; In: gray) with an area ratio Cu/In of approximately 1, and a Cu-In alloy target with Cu/In of 9/11.

Fig. 3.1 illustrates schematically the RF reactive sputter apparatus used in this work for depositing CIS films. The complete sputter system basically consists of five parts: a RF generator, a matching unit, the deposition chamber, a pumping system, and the gas inlet system. Each part plays a specific role in the sputter process as outlined below.

- RF generator: The RF generator is used to create a dense glow discharge between the target (cathode) and the substrate (anode), and to cause a bias potential to build up on the target surface. The positively charged ions in the plasma are, by several orders of magnitude, heavier than the negatively charged electrons. While the electrons can follow and neutralize positive charges, the ions no longer follow the high frequency switching, particularly in the radio freqency (13.56 MHz) regime, leading to an unaltered negative self biasing of the target relative to the substrate, as shown in Fig. 3.2. The negative bias potential of the traget with respect to the substrate results in the ion bombardment, i.e., sputtering of the target. A SG-1250 RF generator with a maximum output of 1250 W was used in our sputter apparatus.

- Deposition chamber: The deposition chamber (sputter chamber) is a glass-walled vacuum station, equipped mainly with water cooled target holder (cathode electrode) at the top and back shields, adjustable water cooled substrate holder (anode electrode),

and accessory base rings. In our sputter apparatus, the distance between the target and substrate is approximately 8 cm.

- Matching unit: A matching unit is designed and mounted normally on top of the sputter chamber, to achieve an efficient energy transfer from the RF generator at a nominal load of approximately 50 Ω, to the sputter chamber, which has a considerably higher impedance.

- Pumping system: There are two pumps, a mechanical rough pump and a molecular turbopump, together with a liquid nitrogen trap, connected to our sputter system. A pressure of 10^{-5} Pa could be achieved.

- Gas inlet system: There are several mass flow controllers (MFC) installed in our sputter apparatus, which enables individual control of the flow rates of the individual gases.
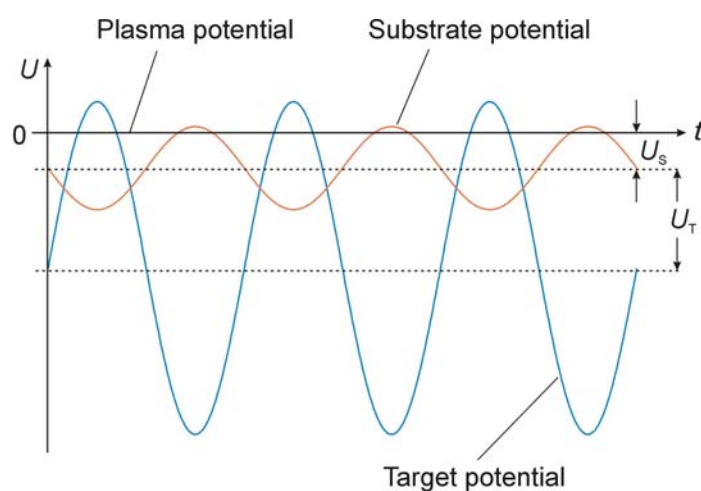
Fig. 3.2. The target, substrate, and plasma potentials in a RF sputter process as a function of time, and the self bias potentials of the target, U_T, and substrate, U_S, with respect to the plasma. There is an unaltered negative potential between the target and the substrate.

3.2   Film deposition

During the course of this study, CIS films were prepared on bare, Mo-, or ZnO-coated float glass and single crystalline sapphire substrates by RF reactive sputtering with the setup described above. Two kinds of targets, a Cu-In inlay target and a Cu-In alloy target, were used for sputter deposition of CIS films. Both targets were originally 4 inches in diameter and 0.25 inches thick, as illustrated in Fig. 3.1 (b). The Cu-In inlay target with an area ratio Cu/In of approximately unity resulted in films of good crystallinity and morphology, however, highly off-stoichiometry (extremely Cu-rich). Using instead a Cu-In alloy target

with Cu/In of 9/11, nearly stoichiometric CuInS$_2$ films were produced. In this thesis, if no special notation is given, the films are sputtered with the Cu-In alloy target.

Prior to film deposition the sputter chamber was normally evacuated to about 10^{-4} Pa. Immediately before the sputter process, the bare or coated float glass or sapphire substrates were cleaned ultrasonically in organic solvents: acetone and methanol, each for about 5 min, then dried by compressed nitrogen gas. Even for sapphire substrates used for epitaxial growth of CIS films, no chemical etching or heating treatments were further performed before film growth.
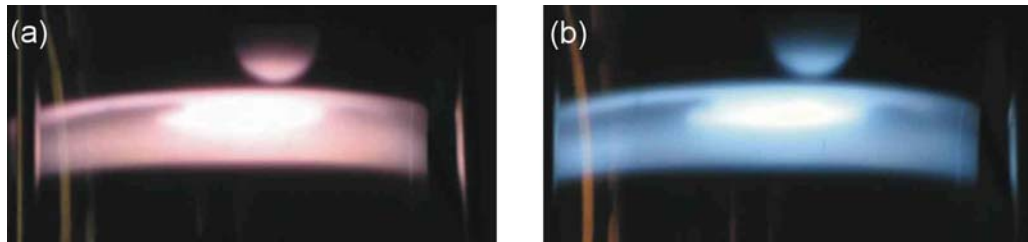

Fig. 3.3. (a) The plasma generated by a mixture gas Ar/H$_2$S, (b) the plasma generated by pure H$_2$S gas.

Pre-sputtering, i.e., cleaning of the target was generally performed with an argon (purity: 99.999%) plasma for 10 min. H$_2$S (purity: 98.0%) was introduced as reactive gas. At the beginning of this work, we sputtered CIS films in an Ar/H$_2$S mixture atmosphere. Cu-In secondary phases were usually found incorporated in the films sputtered in such an atmosphere. By introducing H$_2$S solely as both reactive and working gas during sputtering, nearly stoichiometric films with pure CIS phase were deposited. Interestingly, while the color of the Ar/H$_2$S plasma is pink-like, the plasma generated by pure H$_2$S is more like ice blue (see Fig. 3.3). As will be discussed in the following chapters, the deposition parameters have a strong influence on the properties of the sputtered films. In table 3.1, the general sputter parameters used in the present study are summarized.

Table 3.1. Summary of typical sputter parameters for deposition of CIS films in this work.

Substrate	Power (W)	Substrate temperature (°C)	H$_2$S flow rate (sccm)	p(H$_2$S) (Pa)	Ar flow rate (sccm)	p(total) (Pa)	Deposition rate (nm/min)
Float glass	200	400	10-17.5	1.04-1.87$\times10^{-1}$	1.5-2.3	2.0 - 2.67$\times10^{-1}$	-
Float glass	200	400	17.5-29	1.87-2.93$\times10^{-1}$	-	1.87-3.20$\times10^{-1}$	~ 32
Float glass	200	500	25-35	2.67-3.73$\times10^{-1}$	-	2.67-3.73$\times10^{-1}$	-
Float glass	300	400	20-40	1.93 - 4.0$\times10^{-1}$	-	1.93 - 4.0$\times10^{-1}$	-
Float glass	300	500	40-45	4.0 - 4.53$\times10^{-1}$	-	4.0 - 4.53$\times10^{-1}$	-
Sapphire	200	500	30	3.07$\times10^{-1}$	-	3.07$\times10^{-1}$	~ 40

For comparative studies, several binary compound and elemental films, such as Cu_2S, CuS, Cu-In, metallic Cu films, were prepared as well using the same sputter setup. Typical sputter parameters for these films are outlined in table 3.2, along with the typical deposition rates. Metallic Mo layers, typical back contacts for CIS-based solar cells, were sputtered also in this work, with the parameters given in table 3.2.

Table 3.2. Typical sputter conditions for Cu-In, Cu_2S, CuS, Cu, and Mo films in this study.

Film	Target	Power	Substrate temperature	H_2S flow rate	$p(H_2S)$	Ar flow rate	p(total)	Deposition rate
		(W)	(°C)	(sccm)	(Pa)	(sccm)	(Pa)	(nm/min)
Cu-In	Cu-In alloy [a]	100-200	RT	-	-	4.2	1.6×10^{-1}	~16 (200W)
Cu_2S	Cu [b]	100-300	RT-500	3.5-10	$0.4\text{-}1.07\times10^{-1}$	2.3	$1.25\text{-}1.93\times10^{-1}$	21~27
CuS	Cu	50-100	RT-200	10	1.07×10^{-1}	2.3	1.93×10^{-1}	~ 20
Cu	Cu	300	RT	-	-	4.2	1.6×10^{-1}	~ 24
Mo	Mo [c]	200-300	RT	-	-	4.2	1.6×10^{-1}	~11 (200W)

a) Purity: 99.99%; b) purity: 99.999%; c) purity: 99.95%.

4 Characterization methods: principles and instruments

Several methods have been used to characterize the sputtered films in this study. For structural characterization, the techniques such as X-ray diffraction (XRD), X-ray reflectometry (XRR), and transmission electron microscopy (TEM) were employed. The surface and morphology analyses were accomplished by photoemission spectroscopy (XPS and UPS) and secondary ion mass spectrometry (SIMS), atomic force microscopy (AFM) and scanning electron microscopy (SEM), including energy-dispersive X-ray analysis (EDX), respectively. SIMS and EDX were additionally utilized to examine the composition of the films in the bulk. The optical and electrical properties of the films were determined by optical transmission and Hall effect measurements, respectively. In this chapter, the main principles of these techniques, and the specific instruments and typical measuring conditions (parameters) used in this work are briefly described.

4.1 Structural characterization methods (XRD, XRR, and TEM)

4.1.1 X-ray diffraction

X-ray diffraction is a powerful non-destructive method for material characterization, by which the crystal structure, orientation, and grain size can be determined. The characterization is usually carried out with a typical X-ray wavelength that is comparable to the interatomic distance in a crystal (~ 0.1 nm). When X-rays impinge on a crystal, the individual atoms act as secondary radiation emitters and cause interference analogous to the diffraction of light from a grating. Constructive interferences give the diffraction peaks according to Bragg's law,

$$2d\sin\theta = n\lambda ,\tag{4.1}$$

which relates the distance between a set of planes, d, in a crystal and the angle, θ, at which these planes will diffract X-rays of a particular wavelength, λ.

In an X-ray diffractometer the X-ray source is usually in fixed position and the sample stage and the detector can be rotated individually or simultaneously. According to the

rotation possibility of the sample stage and detector, the X-ray diffractometers are generally classified as powder diffractometers, which are suited for probing powder or polycrystalline samples, and four-circle diffractometers, particularly designed for single crystalline specimens or texture analysis of oriented polycrystalline samples.

X-ray powder diffraction

Fig. 4.1 shows the schematic representation of a standard Bragg-Brentano powder diffractometer, Siemens D5000, in the First Physics Institute of Giessen University. In such a powder diffractometer, the sample stage and detector can only rotate in the same plane, along the same axis (diffractometer axis) perpendicular to the figure and located at the center of the sample stage, and thus it is also called two-circle diffractometer. Depending on the coupling of the sample and/or detector rotations during diffraction measurements, three scan modes, i.e., θ-2θ scan, rocking curve, and detector scan are used for structural characterizations.
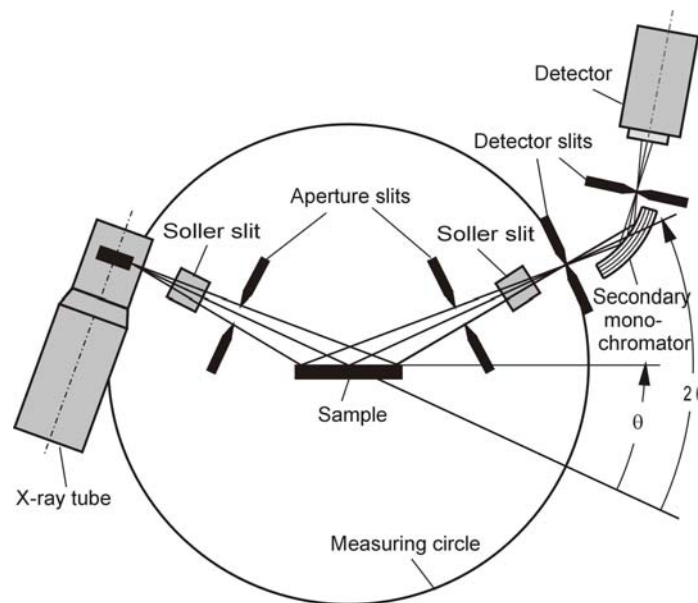

Fig. 4.1 Schematic representation of Bragg-Brentano powder diffractometer, Siemens D5000.

In the case of θ-2θ scan, when the sample is rotated the detector follows the sample motion in the same direction around the diffractometer axis by twice the speed of the sample. This technique is also called locked-coupled scan. In θ-2θ scan, the reflections from the planes parallel to the substrate surface are detected. This allows to determine the orientation along the growth direction of an epitaxial layer or preferentially oriented polycrystalline film with respect to the substrate. In addition, the full width at half maximum (FWHM) of the peak, $\Delta(2\theta)$ (in radians), is a measure of the size, b, of the

grains in a polycrystalline film or the mosaic blocks in an epitaxial layer, as described by Scherrer's formula [1]:

$$b = \frac{0.89\lambda}{\Delta(2\theta) \cdot \cos(\theta)},$$

(4.2)

where θ is the Bragg angle and λ the X-ray wavelength. When the grains are larger than the film thickness, h, then $b=h$.

In the rocking curve mode, known also as ω scan for four-circle diffractometer, the sample is "rocked" by a small angle around the Bragg angle θ with the detector remaining in a fixed position (2θ). The half width of the rocking curve is a direct measure of the range of orientation present in the crystal, thus, it is commonly used for evaluating the out-of-plane ordering of the epitaxial layers.

In detector scan (2θ scan), while the sample is fixed the detector rotates alone. For grazing incidence X-ray diffraction (GIXRD), the detector scan mode is always adopted. While the X-ray beam irradiates the sample at a constant grazing angle, e.g., 1.0°, the detector counts the diffracted signals in a set 2θ range.
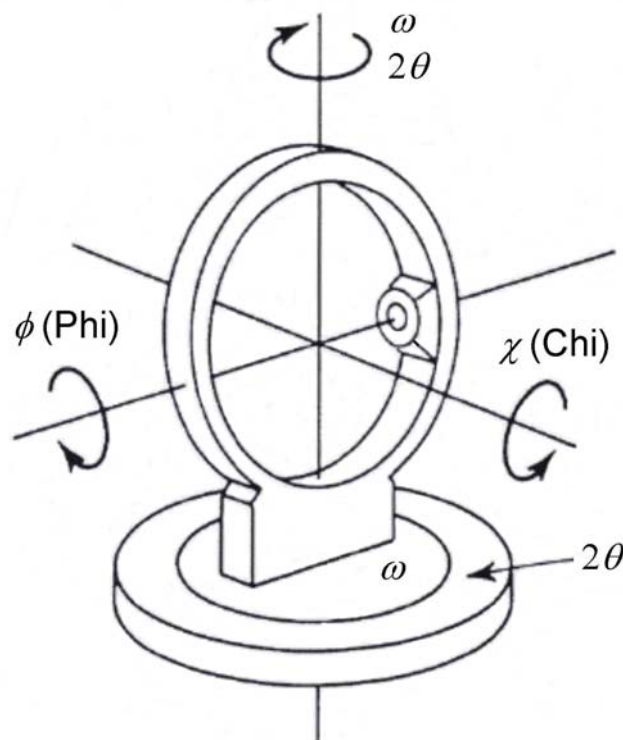

Fig. 4.2 Schematic illustration of the configuration of a four-circle X-ray diffractometer.

Four-circle X-ray diffraction

For assessment of the quality of an epitaxial layer or texture analysis of a preferentially oriented polycrystalline film, a four-circle X-ray diffractometer is necessarily required. In a four-circle X-ray diffractometer, the sample can rotate in three planes, i.e., ω, ϕ, and χ-circles, as indicated in Fig. 4.2, plus the 2θ-circle for detector rotation, the diffractometer is thus called four-circle diffractometer.

A material is called textured if the grains are aligned in a preferred orientation along certain directions. The textured state of a material (typically in thin films) can be viewed as an intermediate state in between a completely randomly distributed polycrystalline powder and a perfectly oriented single crystal. For texture analysis, a polefigure, typically Chi-Phi mapping, is carried out measuring the intensity of a given reflection (2θ is constant) at a large number of different angular orientations of the sample, i.e., various settings of Chi and Phi. Normally one measures all Phi (in-plane rotation) values for a given angle of Chi (azimuth angle), then changes Chi and repeats the process until the whole range of Chi and Phi is covered. For different specific purpose, one can perform also the Phi-2θ mapping while keeping Chi at a fixed angle, as we will demonstrate in chapter 6.

Under grazing incidence conditions, with an incident angle of typically 1° or lower, the incident X-ray beam is nearly parallel to the film surface, thus the reflections generated from the planes perpendicular to the surface are detected. By grazing incidence ω or ϕ-scans, the in-plane orientation of the films with respect to the substrates can be directly determined.

Experimental setups

For characterization of the sputtered polycrystalline films on float glass substrates, we used a Bragg-Brentano powder diffractometer, Siemens D5000, which is schematically illustrated in Fig. 4.1, with Cu K$_\alpha$ (λ= 0.15418 nm) radiation and a scintillation detector. The X-ray tube was typically operated at a voltage of 40 kV and a current of 20 mA.

A Siemens-Stoe AED2 four circle-diffractometer with Mo K$_\alpha$ (λ =0.71069 Å) radiation, in the Institute of Inorganic and Analytical Chemistry of Giessen University, was employed for characterization of epitaxially grown thin films on sapphire. X-ray diffraction measurements of thick CIS films sputtered with a thin buffer, grown quasi-epitaxially on sapphire, were mainly carried out at the Institute of Experimental Physics of Magdeburg University. For normal θ-2θ scans a standard Bragg-Brentano diffractometer, Siemens D5000, with a Cu K$_\alpha$ radiation and graphite secondary monochromator was used. A Seifert/FPM URD6/TZ6 four-circle X-ray diffractometer, with a Cu K$_\alpha$ X-ray source, Barthels primary monochromator, Eulerian cradle sample stage, and a Ge(220) secondary analyzer was applied for the Phi-Chi scan (polefigure) measurements. Grazing incidence diffraction was accomplished with a Seifert/FPM URD6 four-circle diffractometer,

equipped with a Cu K$_\alpha$ radiation source, a primary vertical Soller collimator (0.15°), a vertical translation sample holder, and a secondary vertical Soller collimator and LiF analyzer.

Further information on X-ray diffraction techniques is referred to [1-3].

4.1.2 X-ray reflectometry

Theoretical background

X-ray reflectometry is now a well suited method for the study of surfaces and thin layers, since it provides a wealth of information on thickness and interfacial properties on the nanometer scale, like layer thickness, the layer's electronic densities, surface and interface roughness and roughness morphology.

The measurement principle is based on the fact that the refractive index for all elements and compounds at short wavelengths of X-rays ($\sim$ 0.1 nm) is slightly smaller than 1:

$$n = 1 - \delta - i\beta \tag{4.3}$$

with δ describing the dispersion and β the absorption of a material at a certain wavelength. Consequently, external total reflection occurs when X-rays hit a sample at a grazing incidence angle. As the refractive index for the interesting wavelengths is very close to 1 (δ and β are positive and have values typically of the order 10^{-6}), total reflection occurs at very small incidence angles of the order of several tenths of a degree. The exact value for the critical angle of total reflection Θ_C can, in principle, be used to determine the density of a deposited film or the density at the surface of a bulk material according to:

$$\Theta_C = \sqrt{2\delta} \tag{4.4}$$

with

$$\delta = \frac{N_a r_e \rho}{2\pi A}(Z + f')\lambda^2 , \tag{4.5}$$

where N_a is the Avogadro's number, r_e the classical electron radius, ρ the mass density, A the atomic mass, Z the atomic number, f' the dispersion correction, and λ the X-ray wavelength.

At incidence angles slightly above the critical angle of total reflection of a thin film, some intensity penetrates into the film and is partly reflected at the interface between the film and the substrate. The radiation reflected from the interface interferes with that reflected directly from the film surface. Upon changing the incidence angle, the two

contributions give rise to interference fringes whose spacing is characteristic for the film thickness. The equation

$$\Theta_m^2 = \Theta_C^2 + \frac{\lambda^2}{4d^2}m^2$$ (4.6)

gives the position of the mth interference maximum as a function of the total reflection angle of Θ_C, with wavelength λ and the film thickness d, and therefore offers the possibility to determine the film thickness from the position of interference maxima [4].

Experimental procedures

In this study the XRR measurements were performed with the same diffractometer used for X-ray powder diffraction, equipped with a modified sample stage, designed specially for XRR by Bruker AXS. In addition to the main parts for XRD, a controllable beam stop and a metal absorber for reducing the too high intensity of the totally reflected X-rays at lower than the critical angle are added, as illustrated in Fig. 4.3. The XRR measurements, in grazing incidence θ-2θ scan mode, of our sputtered CIS films were typically carried out from 2θ = 0.35° to 3.0° with a scan step of 0.002°. Afterwards, the program "Refsim" [5]was used to simulate the experimental curve, to obtain thickness, surface density, and roughness of the layers and roughness of the interfaces between the layers and substrates. Although the described setup allows the measurement of film thickness up to about 300 nm for very smooth surface, we can, in practice, measure only films with thickness less than 100 nm, due to the rough surfaces of the sputtered CIS films.
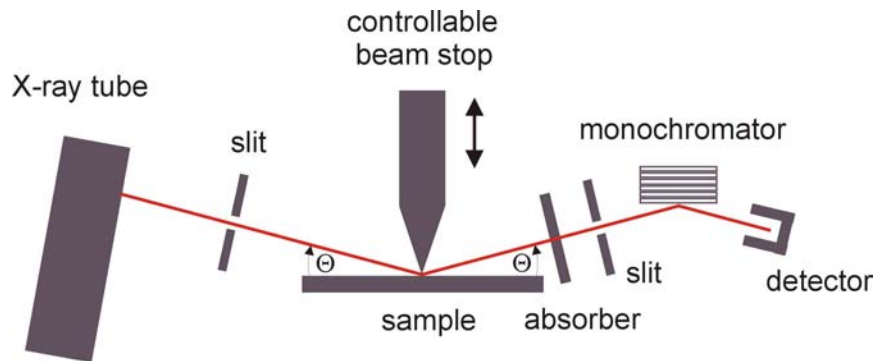

Fig. 4.3. Illustration of the setup for X-ray reflectometry.

More detailed theoretical background on X-ray reflectivity and introduction to practical X-ray reflectometry techniques can be found in [4, 6-12].

4.1.3   Transmission electron microscopy

Transmission electron microscopy is a versatile tool capable of characterizing the internal structure of a wide range of materials [13]. TEM characterization enables not only the direct imaging of the microstructure, but also the identification of the phases present in the specimen by either electron diffraction or spectroscopic chemical analysis. The results obtained from a typical TEM characterization offers a better understanding of the relation between the microstructure and properties of the materials.

There are various operation modes of the electron microscope. The bright field (BF) mode is usually used to image grains and defect structures within the specimen. It can also reveal secondary phases such as precipitates or inclusions. Similar in purpose to the BF technique, the dark field (DF) imaging mode uses the specific Bragg diffracted electrons to image the region from which they originated. The DF mode enables the connection between the crystallographic information and specific regions or phases in the sample. The principal function of the electron diffraction technique is to determine the crystallographic structure of the material being analyzed. By placing an aperture in the image plane, then projecting the diffraction pattern of that image onto the recording plate, the selected area diffraction pattern (SADP) is obtained.

For more detailed description of TEM techniques and practical applications in material research refer to [13-16].

4.2   Surface   and   morphology   characterization methods (XPS, UPS, SIMS, SEM, and AFM)

4.2.1   Photoemission spectroscopy (XPS and UPS)

X-ray photoelectron spectroscopy (XPS), known as electron spectroscopy for chemical analysis (ESCA), and ultraviolet photoelectron spectroscopy (UPS), are extreme surface-sensitive methods for chemical and electronic characterization of materials. Surface analysis by XPS or UPS is accomplished by irradiating a sample in vacuum with monoenergetic soft X-rays or ultraviolet radiation and analyzing the energy of the detected electrons. Mg K_α (1253.6 eV) or Al K_α (1486.6 eV) X-rays and He I (21.21 eV) or He II (40.84 eV) radiations are usually used for XPS and UPS, respectively. These photons interact with atoms in the surface region of the sample, causing electrons to be emitted by

the photoelectric effect. The emitted electrons have measured kinetic energies, E_K given by:

$$E_K = hv - E_B - \phi_s \, ,$$

(4.7)

where hv is the photon energy, E_B is the binding energy of the atomic orbital from which the electron originates, and ϕ_s is the spectrometer work function. The spectrum is obtained as a plot of the number of detected electrons per energy interval versus their kinetic energy. Since each element has a unique set of binding energies, XPS can be used to identify the elements in the surface qualitatively referring to the peak positions, and determine quantitatively the concentration of each element, C_x, according to its peak height or peak area, with the formula:

$$C_x = \frac{n_x}{\sum_i n_i} = \frac{I_x / S_x}{\sum_i I_i / S_i} \, ,$$

(4.8)

where I is the number of emitted photoelectrons, and S the atomic sensitivity factor. The chemical shifts, i.e., variations in the elemental binding energies, caused by differences in the chemical potential and polarizability of compounds, can be used to identify the chemical state of the materials. The UPS spectrum is sensitive to the valence band region, thus, gives insight in the density of filled states at and near the surface and allows the extraction of the valence band structure of the material.

photoemission spectroscopy experiments in the present study were carried out using a VG ESCALAB system with photon energy of 1253.6 eV (Mg K_α) for XPS and 21.21 eV (He I) for UPS, respectively, at a base pressure of about 2×10^{-10} mbar. Detailed XPS and UPS investigation on the sputtered CIS films in this work is discussed elsewhere [17]. More information about photoemission background and practical application of ESCA can be found for example in ref. [18-21].

4.2.2   Secondary ion mass spectrometry

Secondary ion mass spectrometry is frequently used to characterize the surface and near surface (~ 30 µm) region of solids and the surface of some liquids. The technique uses a beam of energetic (0.5-20 keV) primary ions, commonly Ar^+, O_2^+, Cs^+, and Ga^+, to sputter the sample surface, producing ionized secondary particles that are detected using a mass spectrometer (magnetic sector-, quadrupole-, or time-of-flight-spectrometers). Three types of SIMS data are generally achievable: mass spectra, depth profiles, and ion images.

A mass spectrum, describing the secondary ion intensities of the species detected as a function of mass, is produced by sputtering a sample while the mass spectrometer scans the

mass range. From the arising masses in the spectrum one recognizes the elements represented, thus, general information about the composition as well as impurities included in the sample surface is achieved. Depth profiles are obtained if, instead of scanning the mass spectrometer as the sputtering continues, one or more masses are monitored sequentially by switching rapidly among masses. Via a depth profile, one receives information about the concentration of selected elements into the depth, and thus the depth homogeneity of the sample is examined. When a mode of data collection analogous to SEM is operated for SIMS, element-specific images or maps can be generated by recording the secondary ions emitted from the sample that are detected with a mass spectrometer. Ion images of SIMS generally provide information about the uniformity of the lateral element distribution at the surface or in the bulk of the sample.

In the present work, SIMS measurements were accomplished with the plant MIQ 56A (CAMECA/Riber), using argon or oxygen primary ions. Mass spectra were recorded to survey the impurities at the surface of the films. Depth profiles were carried out to examine the depth homogeneity of the films.

For deeper insight into secondary ion mass spectrometry techniques see [22-24].

4.2.3   Scanning electron microscopy

Due to its versatility and the wide range of information it can provide, the scanning electron microscope is often the preferred starting tool for analytical microscopy. In SEM a finely focused electron beam scans the sample along closely spaced lines. As a result of the interaction between the electron beam and the specimen, a variety of signals, mainly secondary plus backscattered electrons and X-rays, are produced [25]. Using special detectors, these signals can be collected giving specific information about the irradiated volume.

Secondary electrons are emitted from the atoms occupying the top surface (~ 5 nm) and produce a readily interpretable image, the contrast of which is determined by the sample surface morphology. Backscattered electrons are primary beam electrons that are 'reflected' from atoms in the solid. As its contrast is determined by the atomic number of the elements in the sample, the image generated by backscattered electrons represents the distribution of different chemical phases in the sample.

Interaction of the primary electron beam with atoms in the sample causes shell transitions which result in the emission of X-rays. Detection and measure of the characteristic X-rays enables elemental analysis, i.e., so-called energy dispersive X-ray analysis (EDX). EDX provides rapid qualitative, or with adequate standards, quantitative analysis of elemental composition within a sampling depth of 1-2 microns. X-rays may

also be used to form maps or line profiles, showing the elemental distribution in a sample surface.

In the present study, a Philips XL20 SEM was applied to observe the surface as well as cross-sectional morphology of the films. The images were produced by detecting the secondary electrons, with a typical acceleration voltage of 10 or 30 kV. An EDX system, using a SiLi-detector with an ultrathin window (UTW), integrated with the SEM setup was used to analyze the composition of the sputtered films. Typical electron acceleration voltage for EDX operation is 10 kV.

General information on working principles of SEM and its versatile applications in materials science can be found for instance in [25-27].

4.2.4 Atomic force microscopy

The atomic force microscope probes the surface of a sample with a microfabricated tip (~10 nm in diameter) mounted on a flexible cantilever (100-200 μm long). Forces between the tip and the sample surface (van der Waals forces or Pauli exclusion forces, etc.) cause the cantilever to bend, or deflect. A detector measures the cantilever deflection as the tip is scanned over the sample. The measured cantilever deflections allow a computer to generate a map of surface topography with resolutions down to atomic and nanoscales. The lateral and vertical movements of the tip or sample are controlled by piezoelectric transducers and a feedback loop that produces voltage differences proportional to the movement.

The atomic force microscope can be operated under two different conditions, in air or in a vacuum, and via two primary modes, contact or non-contact, to produce surface imaging and three-dimensional profiling. Surface imaging by AFM, with a lateral resolution down to about 3 nm, can be used to determine the roughness, grain size, and features on the nanoscale and resolve individual holes, defects (such as pinholes), and atomic clusters on the sample surface. Three-dimensional profiling probes samples in real, three-dimensional space with vertical resolutions up to 0.01 nm. Via storage of digital information, the three-dimensional image may be manipulated and enhanced with color, filtered, enlarged, and displayed from any altitude or azimuth. AFM is suitable to investigate a wide range of materials, including insulators, semiconductors and electrical conductors.

In the course of this study, we used a home-built AFM, in addition to SEM, to characterize the surface morphology of the sputtered films. The AFM was operated in air in the contact mode. Two- as well as three-dimensional images were recorded to provide a

general view on the film surfaces and determine quantitatively the surface roughness and grain size of the films.

A review of AFM techniques can be found in [28].

4.3   Optical transmission

The optical properties of the sputtered CIS films were characterized by optical transmission spectrum measurements. The transmission spectra were recorded with a Varian 2300 spectrophotometer typically in the wavelength range of 350-2500 nm at room temperature.

According to the transmission spectra, the absorption coefficient α of the films was evaluated with the expression

$$T = e^{-\alpha t}, \tag{4.9}$$

which neglects the surface and multiple reflection effects. Here T is the transmission coefficient and t the film thickness. In this study, the thickness of the films was measured either directly by XRR or, for thick films, estimated via multiplying the sputter time by the average deposition rate determined by XRR.

Following the usual theoretical analysis [29], the energy dependent absorption coefficient $\alpha(hv)$ can be expressed by the relation for the allowed direct transition as

$$\alpha(hv) = A(hv - E)^{1/2}, \tag{4.10}$$

where A is a constant, hv the photon energy, and E refers to the direct band edge. By extrapolating along the linear portion of the α^2 versus hv curve to the hv axis, the direct bandgaps of the films, represented by the intercept at the hv axis, were deduced.

4.4   Hall effect measurements

The electrical properties of our sputtered CIS films were characterized by Hall effect measurements. Hall effect experiments were conducted with a Van der Pauw technique. Plated silver or pre-sputtered molybdenum were used for contacts. Typically the carrier concentration, resistivity, and Hall mobility, in dependence on temperature ranging from 77 to 400 K were measured to evaluate the electrical properties of the films. Hall effect investigation on the electrical properties of the sputtered CIS films in this study has been described in detail elsewhere [30]. Detailed measuring procedures for the CIS films and

more basic knowledge about Hall effect technique can be found there and references therein.

5 One-stage deposition of CuInS$_2$ films by RF reactive sputtering

Deposition of CuInS$_2$ film by sputtering usually consists of two steps. At first a precursor of Cu/In stacked multilayers, a Cu-In alloy film or Cu-In-S film is sputtered using, respectively, Cu and In elemental targets [1-3], a Cu-In inlay target [4], or mixed powder target of Cu$_2$S and In$_2$S$_3$ [5]. In a second step, the sputtered precursor is annealed or sulfurized in a H$_2$S or elemental S atmosphere. For industrial application, the simplification of the process is one of the key issues for low cost. The aim of this work is thus set to develop a one-stage process for the deposition of CuInS$_2$ films by RF reactive sputtering [6]. Along with this prospect, we first tried to sputter CuInS$_2$ films using a Cu-In inlay target and H$_2$S gas. Films with good crystallinity and morphology, however, highly off-stoichiometry (extremely Cu-rich) have been obtained [7]. By utilizing a Cu-In alloy target, nearly stoichiometric CuInS$_2$ films can be sputtered but additionally in-situ annealing is necessary due to the deficient H$_2$S flow amount during sputtering [6]. With an extended H$_2$S mass flow controller, we finally succeeded in deposition of CIS films by RF reactive sputtering in one step [8].

To optimize the sputtering process, we first investigated systematically the influence of sputter parameters on the film properties. Then, we focused our studies on the surface characterization of the sputtered films. Its properties are significant for achieving high-efficiency CIS film solar cells. Although stoichiometric CIS films can be sputtered in one step, we have found that post-growth treatments have significant influences on properties of the sputtered films, e.g., enhancement of the structural and optical properties by post-growth annealing, modification of the film surfaces by chemical etching. Detailed studies on these issues are the three main parts of the following chapter .

5.1 Influence of the sputter parameters on the properties of CuInS$_2$ films

5.1.1 Influence of the H$_2$S flow during sputtering

As usual, we began with argon as working gas for providing the plasma, introducing simultaneously the reactive gas H$_2$S for sputtering. In Fig. 5.1 XRD spectra of four films

sputtered at 400 °C with different H_2S flows are presented. Films (a), (b) and (c) were sputtered in a H_2S/Ar atmosphere, while film (d) was sputtered solely in H_2S. Besides peaks of CIS there are some additional peaks originating from Cu-In alloy phases, such as $Cu_{11}In_9$, Cu_4In, and CuIn, coexisting in the films sputtered with argon. We normalized the maximum intensity of each spectrum and chose the same scale, thus, the relative abundance of phases present in the films is represented by the intensity ratio of peaks from different phases. As can be seen, with a fixed Ar flow amount of 2.3 sccm but increasing the H_2S flow rate from 10 to 15 sccm, the secondary Cu-In phases are gradually depressed. In order to keep the total gas pressure during sputtering as low as possible, and since, we thought H_2S could be used as working gas as effectively as argon due to the comparable atomic mass, we decided to use H_2S solely as both working and reactive gas during sputtering [9]. With a H_2S flow rate of 20 sccm, 2.13×10^{-1} Pa in partial pressure, pure $CuInS_2$ phase films with a chalcopyrite structure were obtained (see Fig. 5.1(d)). Hereafter, all the studied films are sputtered with solely H_2S gas if no specific notation is given.
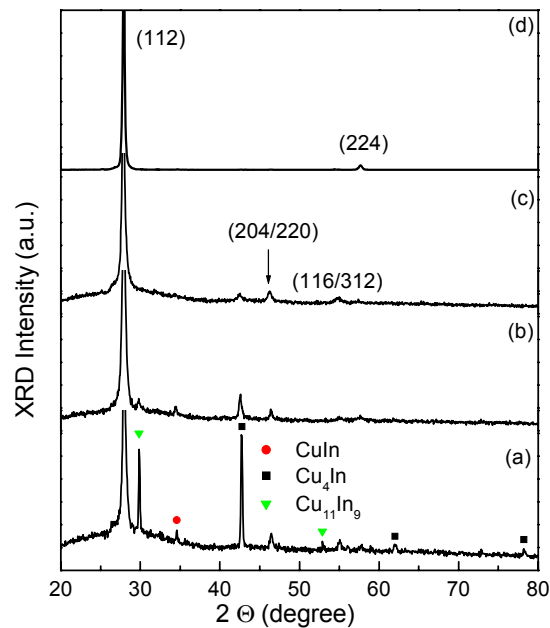
Fig. 5.1. XRD spectra of CIS films sputtered at 400°C and 200 W with different flow rates of H_2S and Ar, (a) $f(H_2S)$ = 10 sccm, $f(Ar)$ = 2.3 sccm; (b) $f(H_2S)$ = 12.5 sccm, $f(Ar)$ = 2.3 sccm; (c) $f(H_2S)$ = 15 sccm, $f(Ar)$ = 2.3 sccm; (d) $f(H_2S)$ = 20 sccm, $f(Ar)$ = 0 sccm.

These films have a highly (112) preferential orientation, since only the (112) and (224) diffraction peaks which originate from the same series of lattice planes of CIS were detected. It is useful to estimate quantitatively the preferred structural (112) orientation. According to the method for evaluating the magnitude of the preferred orientation factor *f*

employed in CuInSe$_2$ thin films and other materials [10, 11], we define the preferred orientation factor $f(112)$ for the (112) plane as

$$f = (p - p_0)/(1 - p_0) \tag{5.1}$$

with

$$p = \sum I_{nn2n} / \sum I_{hkl} \qquad \text{and} \qquad p_0 = \sum I^*_{nn2n} / \sum I^*_{hkl}, \tag{5.2}$$

where I_{hkl} is the measured intensity of (hkl) peak of the films, I^*_{hkl} the standard intensity for the randomly distributed powder CuInS$_2$, and n the diffraction order. For an increasing degree of orientation, p increases from the value p_0 for a nonoriented material to 1 for a totally oriented sample so that the orientation factor f increases from 0 (nonoriented) to 1 (totally oriented). Applying this formula, a preferential orientation factor $f(112)$ as high as approximately 0.96 has been deduced for films sputtered only with H$_2$S [8].
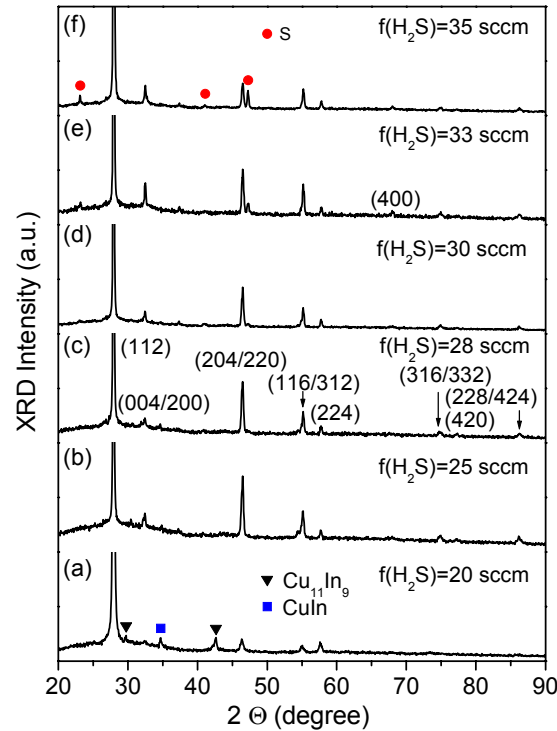
Fig. 5.2. XRD spectra of CIS films sputtered at 500°C and 200 W with different flow rates of H$_2$S.

A H$_2$S flow of 20 sccm is sufficient to sputter pure CuInS$_2$ phase film at 400 °C but not enough to avoid Cu-In alloy phases coexisting in the films sputtered at a substrate temperature of 500 °C [12]. Fig. 5.2 shows the XRD spectra of films sputtered at 500 °C with a power of 200 W but different H$_2$S flows. When the H$_2$S flow during sputtering increased to 25 sccm, the secondary Cu-In phases were suppressed, and nearly pure CuInS$_2$ phase films were obtained. It thus indicates that the higher the substrate temperature is, the

more H_2S is needed to avoid Cu-In alloy minor phases. However, when the H_2S flow is above 30 sccm, there are some additional peaks arising from elemental S present (see Fig. 5.2 (f)). Therefore, the suitable H_2S flow amount for sputtering at 500 °C and 200 W is in the range between 25 and 30 sccm, in contrast to a H_2S flow rate of 20-29 sccm which is suited for sputtering at 400 °C and 200 W, as listed in Table 5.1.
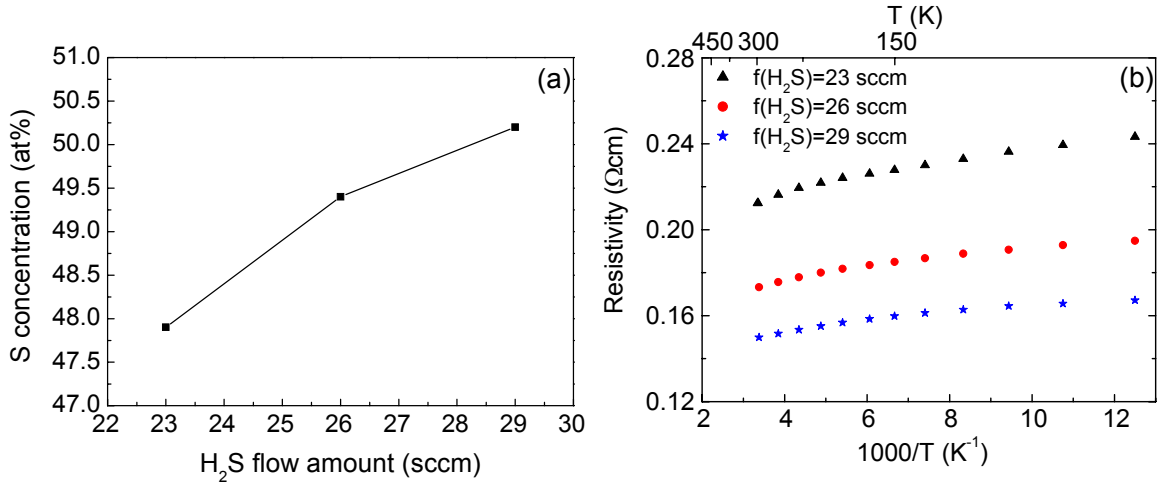

Fig. 5.3. (a) S concentration in the films sputtered at 400° and 200 W with different H_2S flows and (b) the temperature dependence of the resistivity of these films.

With a fixed sputter power and substrate temperature, a higher H_2S flow during sputtering, as expected, results in a higher S content in the sputtered films. Fig. 5.3 (a) shows the S content in the films (determined by EDX) sputtered at a RF power of 200 W and a substrate temperature of 400 °C with different H_2S flows. The S atomic concentration increases from 47.9% to 50.2% as the H_2S flow is increased from 23 sccm to 29 sccm. In Fig. 5.3 (b), the corresponding resistivities of these films are compared. The aged films (exposed to air for several weeks) are *p*-type as determined by Hall effect measurements. The higher S content reduces the S vacancies (favorable for *n*-type) in the films, thus enhancing the *p*-type conducting of the films and, consequently, leads to slightly higher hole concentrations and lower resistivities of the films [12].

5.1.2   Influence of the substrate temperature

We heated the substrates to different temperatures while keeping the other parameters constant to investigate the influence of the substrate temperature on the film properties. In Fig. 5.4 XRD spectra of two films sputtered with a same power of 200 W but different substrate temperatures of 400 and 500°C, respectively, are presented for comparison. A logarithmic scale is used for the XRD intensity in order to see more details. A higher

temperature of 500°C reduces the full width at half maximum (FWHM) of the (112) peak from 0.239° to 0.162°. Accordingly, the grain size increases from approximately 59 to 132 nm as deduced by the Scherrer formula [13], taking into account corrections for the instrumental line width of the X-ray diffractometer.
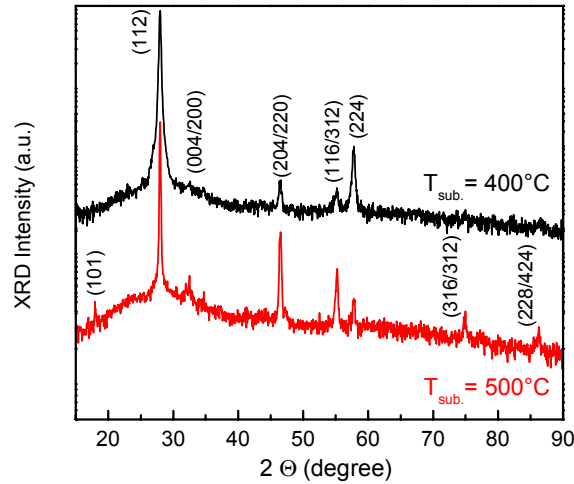

Fig. 5.4. XRD spectra of CIS films sputtered with the same power of 200 W but different substrate temperatures of 400 and 500°C.

In addition, aside from the peaks appearing in the layer sputtered at 400°C there are more peaks centered at 17.95°, 75°, and 86.3°, corresponding to CIS (101), (316/332), and (228/424) planes, respectively, shown in the 2θ spectrum of 500°C sputtered film. This indicates an improvement of the crystalline quality of the films. However, the film sputtered at 500°C has a much lower preferential orientation than the one sputtered at 400°C. According to the formula (5.1), we find a preferential orientation factor f(112) of only 0.41 for the 500°C sputtered layer, much lower than that of the film sputtered at 400°C. Since the sputtering is mainly occurring in one direction, the films in general grow preferentially along this sputter direction. The reduced preferential orientation in the films sputtered at higher temperature is presumably interpreted as follows. On the one hand, the in-plane transverse growth derived by elevated substrate heating (thermodynamic energy-derived) may eliminate the preferential growth governed by sputter direction (kinetic energy-derived). On the other hand, the higher temperature leads to bigger grains in the layer and greatly reduced grain boundaries, which is essential for releasing the stress caused by the preferential grain orientation [12].

Fig. 5.5 depicts the SEM images (surface and cross section) of the films sputtered at 400°C and 500°C. One can clearly see that the grains of film sputtered at 500°C are, indeed, much bigger (more than a factor 2) than those of the film sputtered at 400°C, directly confirming the XRD results described above. However, the thickness of both

layers are nearly identical, which may support our above conjecture — the in-plane transverse film growth (e.g. planar grain size) is derived by substrate heating while the film growth in vertical direction (e.g. thickness and orientation) is mainly governed by sputtering of the target, e.g. sputter power, time and direction [12].
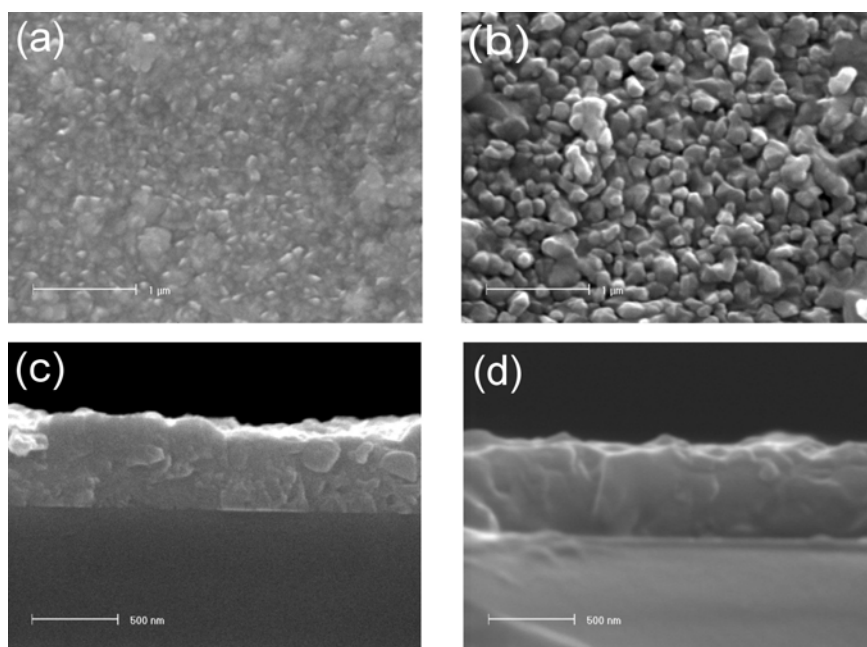

Fig. 5.5. SEM images from the surface (a) and cross section (c) of film sputtered at 400°C and the surface (b) and cross section (d) of film sputtered at 500°C.
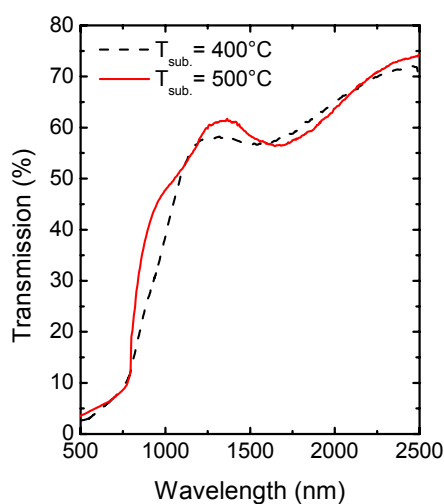

Fig. 5.6. Comparison of the optical transmission spectra of films sputtered at 400 and 500°C.

The promoted structural quality of the films sputtered at higher temperature further leads to a considerable improvement of the optical properties of the films. Fig. 5.6 shows

the room-temperature transmission spectra of two samples sputtered at 400 and 500°C, respectively. A higher substrate temperature (500°C) results in a much sharper absorption edge and shifts the optical bandgap from approximately 1.27 eV (400°C) to 1.44 eV (500°C). This can be attributed to a reduction of the defects in the grains and especially at the grain boundaries. The bandgap of 1.44 eV for a film sputtered at 500°C is slightly lower than that of CIS single crystals (~1.53 eV), but is in line with the value reported by other researchers for CIS films [1, 14].

5.1.3   Influence of the sputter power

We studied also the sputter power effect on the properties of the films. We found, in general, that the higher the sputter power is, the more H_2S flow is needed during sputtering to avoid secondary phases such as Cu-In alloy phases in the films. It can be reasonably understood that higher sputter power gives rise to a higher sputter rate of Cu-In from the target, and thus more reactive gas, i.e. H_2S, is needed. Unlike the substrate temperature effect, there is no strong influence of sputter power on the grain size of the films. In table 5.1 the typical sputter parameters as well as the structural and optical properties (bandgap) of sputtered films are summarized.

Table 5.1. Summary of sputter conditions used in one-stage RF reactive sputtering and the structural, optical properties of typical as-grown CIS films.

Sputter conditions			Structural properties			Optical properties
Power (W)	Substrate Temperature (°C)	H_2S flow [a] (sccm)	FWHM of (112) (°)	Grain size XRD (nm)	Grain size AFM/SEM (nm)	Optical bandgap (eV)
200	400	25 (20-29)	0.239	59	~95	1.24-1.37
200	500	28 (25-30)	0.162	132	~145	1.42-1.44
300	400	40	0.241	58	-	1.33
300	500	45	0.159	139	-	1.44

[a] The values in parentheses give the range of H_2S flow suitable to get pure $CuInS_2$ phase films.

5.1.4   Effect of coating the substrate

Since a low temperature process is more desirable for industrial applications, we tried to sputter CIS films at a temperature as low as possible. As found experimentally, pure CIS phase films can be sputtered on bare float glass at a substrate temperature as low as 200°C with an appropriate H_2S flow. However, the adhesion between the sputtered layers and substrates is poor when the substrate temperature during sputtering is lower than 350°C. Only at temperatures around 400°C or above high quality films with good adhesion can be achieved on bare glass substrates. To reduce substantially the temperature for deposition,

we tried coating the float glass substrates prior to sputtering of CIS with buffer layers such as metallic Mo or ZnO.

Molybdenum (Mo) layer is the commonly used back contact for CIS solar cells. It can be easily sputtered at room temperature by RF sputtering. The typical sputter parameters have been described in chapter 3.
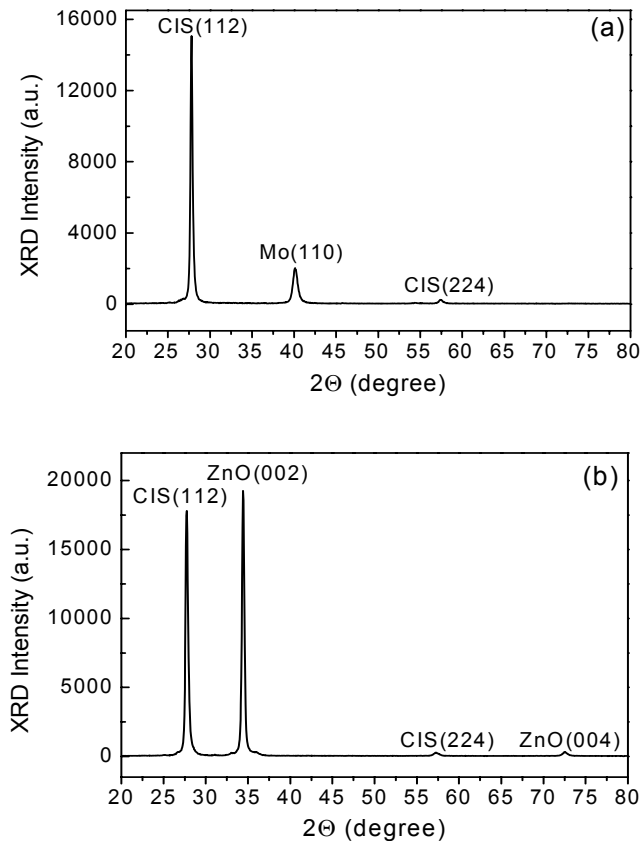

Fig. 5.7. Typical XRD spectra of CIS films sputtered on (a) Mo- and (b) ZnO-coated float glass substrates at a temperature of 200°C.

Pure and/or doped ZnO layers, transparent conducting oxide (TCO), are typical windows for CIS-based solar cells. Some groups demonstrated CIS solar cells in a superstrate configuration, i.e., metal/CIS/buffer/TCO/glass. In this study, we fabricated the simplest device-like structure, CIS/ZnO:Al/glass layer system, all by sputtering, on the one hand to investigate the CIS growth behaviour with an underlying ZnO buffer, and on the other hand to examine the possibility for *p-n* junction formation [15]. ZnO:Al (ZnO doped with 1.5-2.5 at% Al) were prepared on float glass substrates by reactive mid-frequency (MF) magnetron sputtering at a substrate temperature of 200°C in an O_2/Ar atmosphere, using a segmented Zn:Al-target. The MF sputtered ZnO:Al/glass layers were subsequently subjected to RF sputtering of CIS.

By the deposition of Mo or ZnO:Al layers as a buffer on the float glass, high quality CIS with good adhesion behavior can be sputtered at a relatively low temperature of 200°C. Fig. 5.7 shows the typical XRD spectra of CIS films sputtered on Mo-coated and ZnO:Al-coated float glass substrates. Along with peaks from Mo and ZnO, only (112) and (224) diffraction peaks of chalcopyrite CIS were unambiguously detected, indicating a strong preferential orientation of both films. Their preferential orientation factors f(112) are comparable to that of CIS films sputtered directly on float glass at a temperature of 400°C, as listed in table 5.2. The grain sizes of these films, estimated from the FWHM of the (112) peak by means of the Scherrer formula, are included also in table 5.2, in comparison with those estimated by AFM. In general, the average grain sizes estimated by AFM are much bigger than those by XRD. Such a difference was also found in grain size estimation with electron microscopy and XRD by other researchers in other materials [16, 17]. Ishikawa *et al* attributed the difference to two factors: twin structure and the tendency to overlook smaller particles in electron microscopy [17].

Table 5.2. Summary of substrate temperature, FWHM of the (112) peak, average grain size, and preferred orientation factor f(112) of different CIS film systems.

Layer system	Substrate temperature (°C)	FWHM of (112) peak (°)	Grain size		f(112)
			XRD	AFM	
			(nm)		
CIS/Glass	400	0.278	54	95	0.96
CIS/Mo/Glass	200	0.288	48	85	0.95
CIS/ZnO/Glass	200	0.352	34	55	0.95

In addition to the effect of lowering the substrate temperature for sputtering, the Mo or ZnO buffer layers are very effective to work as a barrier to prevent Na diffusion from the float glass into the sputtered CIS layers. This will be discussed in more detail in section 5.2.5. In general, the surface of CIS layers on ZnO-coated glass is smoother but the grains are smaller than those on Mo-coated or bare float glass as revealed by AFM. Films sputtered both on Mo-coated substrates and on bare float glass are covered by an incoherent top layer of Cu_xS as identified by SEM and EDX. These observations will be described in detail in the following section.

5.1.5   Conclusions

The quality of CIS films deposited by one-stage RF reactive sputtering can be controlled by parameters such as the injection rate of reactive gas (H_2S flow), the substrate temperature, and the sputter power. There are mainly secondary Cu-In phases coexisting in

the films when the H_2S flow is too low during sputtering, however, excessively injected H_2S causes an extra minor phase of elemental S in the sputtered films. With a RF power of 200 W and a H_2S flow in the range of 20-30 sccm, highly (112)-oriented good quality films with very good adhesion can be sputtered on bare float glass at a substrate temperature of 400°C or above. Raising the substrate temperature or sputter power needs a higher H_2S flow during sputtering. Increasing the substrate temperature from 400 to 500°C results in an improvement of the structural quality and subsequently enhances the optical properties, shifting the film bandgap from approximately 1.27 to 1.44 eV. Mo- or ZnO-coating of the substrates can help to reduce the substrate temperature to 200°C, and work effectively as a barrier to prevent Na diffusion from the substrates into the sputtered CIS layers.

5.2   Surface characterization of one-step sputtered CuInS$_2$ films

Knowledge of the stoichiometry as well as electronic structure of a semiconductor surface is very important for the development of a heterojunction device. We hence focus the following study on a survey of the surface with respect to the bulk of our sputtered CIS films.

5.2.1   Chemical analysis and valence band structure by photoemission spectroscopy (XPS and UPS)

Photoemission spectroscopy, including XPS and UPS, is a particularly sensitive method for surface characterization. We carried out XPS to accomplish qualitative analysis on the elemental and chemical identification of the film constituents and quantitative analysis of film surface composition with respect to the bulk. The UPS measurements were performed to achieve information about the valence band structure of the sputtered films.
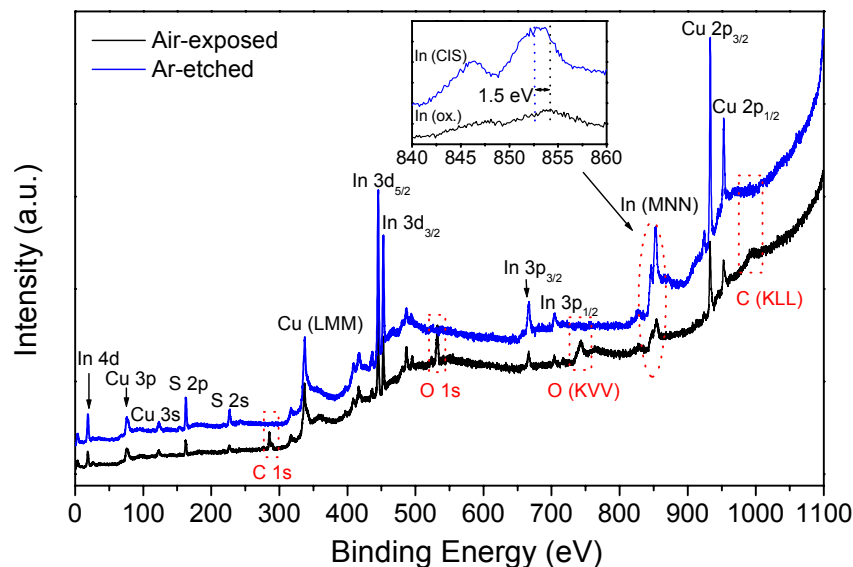
Fig. 5.8. Typical XPS survey spectra recorded on air-exposed and argon-sputter-cleaned surface of CIS films on Mo-coated glass substrates.

After deposition, the films were transferred in air to the analysis chamber of the ESCA setup. Sputter cleaning of the samples was performed with 2 keV Ar-ions. Fig. 5.8 shows

the typical survey spectra recorded on air-exposed and argon-sputter-cleaned surfaces of CIS films on Mo-coated glass substrates. In the spectrum of the air-exposed film, along with the peaks associated with the elements of CIS, there are additionally C and O related peaks, due to physical adsorbates of elemental carbon and oxygen and/or chemical adsorbates such as organic H-C species and various oxides. Detailed inspection shows that the surface exhibits, to different extent, oxidation of all the three elements of CIS. The Cu $2p$ and the S $2p$ lines shift a little while the surface is being sputter-cleaned. The strong oxidation of In can be seen from the Auger-lines (In MNN), as inserted in Fig. 5.8. The oxidized top layer has typically a thickness of about 5 nm, as estimated by the sputter rate. A sputter time of 20 min is normally sufficient to remove the surface phases completely.
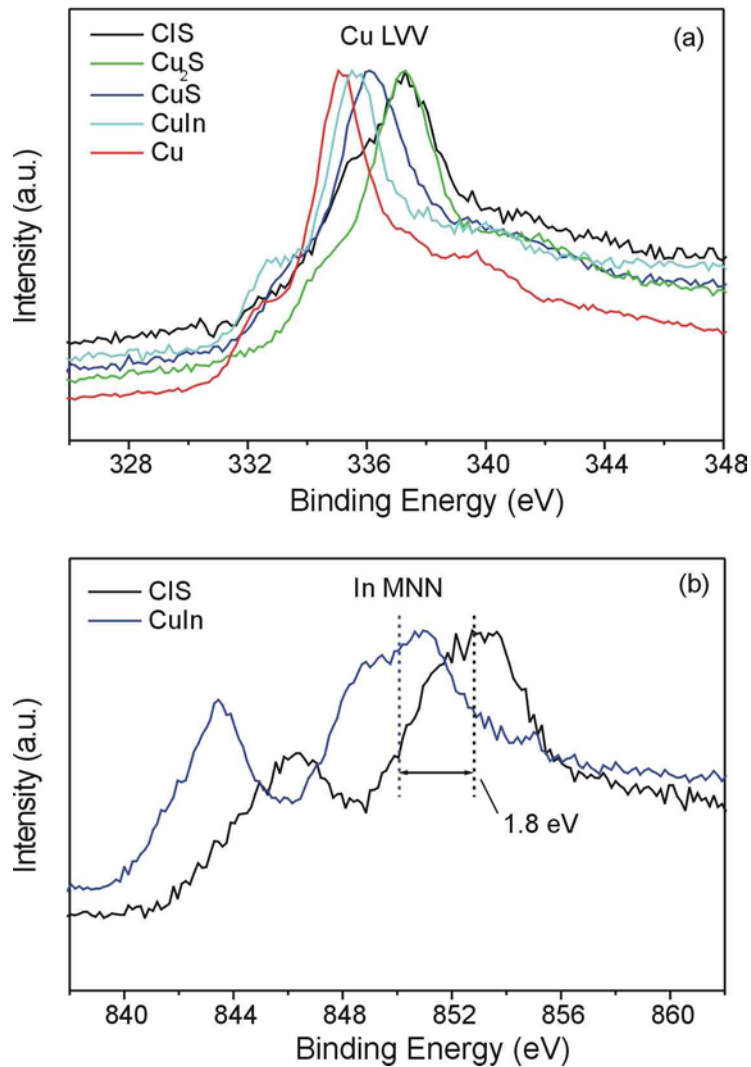
Fig. 5.9. (a) Comparison of Cu LVV lines of CIS, Cu_2S, CuS, CuIn, and pure Cu films sputtered with the same setup and comparable conditions. (b) Comparison of In MNN lines of CIS and CuIn films.

Table 5.3. Binding energies of recognizable XPS peaks of CIS, Cu_2S, CuS, CuIn, and elemental Cu films recorded before (in black) and after argon sputter cleaning (in blue).

XPS peaks	Thin Films									
	$CuInS_2$		CuIn		Cu_2S		CuS		Cu	
Cu $3p$	75.7	75.7	76.0	77.5	75.9	75.9	75.4	75.7	75.3	75.4
Cu $3s$	123.0	123.0	123.1	123.4	123.1	123.0	122.5	122.5	122.7	122.8
Cu LVV	337.3	336.7	335.5	335.8	337.3	337.3	336.1	336.1	335.1	336.7
Cu $2p_{3/2}$	933.2	932.9	933.3	--	933.2	932.9	932.4	932.6	932.7	932.6
Cu $2p_{1/2}$	952.8	952.5	953.3	--	953.0	952.7	952.5	952.2	952.5	952.5
In $4d$	18.7	18.4	17.5	18.7	--	--	--	--	--	--
In $3d_{5/2}$	445.3	445.0	444.0	445.2	--	--	--	--	--	--
In $3d_{3/2}$	452.8	452.7	451.6	452.4	--	--	--	--	--	--
In $3p_{3/2}$	666.8	666.2	665.4	666.5	--	--	--	--	--	--
In $3p_{1/2}$	704.7	704.0	704.1	704.2	--	--	--	--	--	--
In MNN	852.8	854.3	851.0	853.5	--	--	--	--	--	--
S $2p$	162.4	162.4	--	--	162.6	162.9	162.3	162.6	--	--
S $2s$	227.1	226.5	--	--	226.8	226.6	226.5	226.3	--	--
C $1s$	--	285.1	--	285.7	--	285.1	--	284.7	--	284.8
O $1s$	--	532.0	--	531.6	--	531.9	--	531.7	--	530.9

For chemical identification of the film constituents, we compared the sputtered CIS films with CuIn, Cu_2S, CuS, and elemental Cu films deposited with the same sputter setup. Fig. 5.9 (a) shows the Cu LVV peaks of these relevant films. Due to the same valence state (Cu^+), CIS has an identical binding energy of Cu LVV with Cu_2S. While the elemental Cu (Cu^0) has the lowest binding energy, CuS (Cu^{+2}) is in between CIS and elemental Cu. From the neutral Cu state to CIS, the binding energy shift is approximately 2.2 eV. Bonding to In, CuIn shifts a little toward $CuInS_2$ relative to atomic Cu. With the presence of S, the In MNN binding energy of $CuInS_2$ shifts upwards by approximately 1.8 eV with respect to CuIn, as shown in Fig. 5.9 (b). Interestingly, this shift is nearly identical with the Cu LVV shift upon S incorporation in CuIn. In table 5.3, all the recognizable peaks from the diverse films recorded before and after Ar sputter cleaning are listed out for comparison. These data are in good accordance with the previously reported data [18, 19]. The comparative study of the sputtered films with the relevant Cu- and/or In-containing films enable us to exclusively conclude that our sputtered films are of $CuInS_2$ phase in the bulk, distinct from any other phase such as CuIn, CuS, Cu_2S, and atomic Cu.
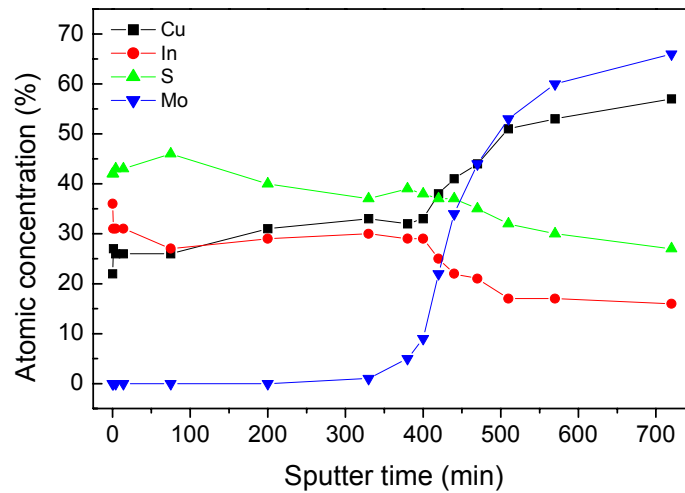
Fig. 5.10. XPS depth profile of a thin layer sputtered on Mo-coated float glass substrate.

We have taken the peak area of the Cu $2p_{3/2}$, In $3d_{5/2}$, and S $2p$ signals for a compositional quantitative analysis. Although there is Cu_xS surface segregation (see discussion below), the as-grown samples are generally In-rich on the surface, whereas in the underlying bulk the stoichiometry is close to ideal within experimental accuracy. A similar compositional behavior has been observed by Scheer *et al* in their coevaporation-deposited CIS films [20]. Fig. 5.10 shows the corresponding XPS depth profile of a layer sputtered on Mo-coated glass substrate at 200°C and 200 W with H_2S flow of 20 sccm.
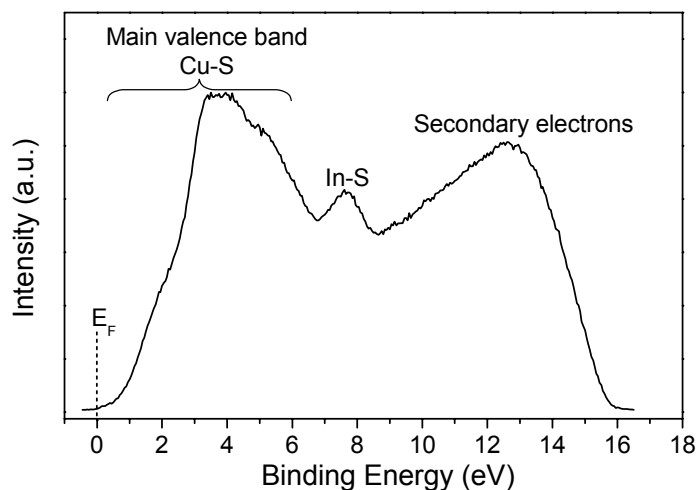
Fig. 5.11. Typical UPS spectrum of the CIS films sputtered on Mo-coated float glass substrates.

The UPS spectrum shown in Fig. 5.11 represents the typical valence band structure of the sputtered CIS films. It is in reasonable agreement with the reported experimental data

and theoretical calculations [21-23]. The measured spectrum has been identified, as shown in the figure, according to the theoretical prediction [23].

5.2.2   Surface morphology by AFM
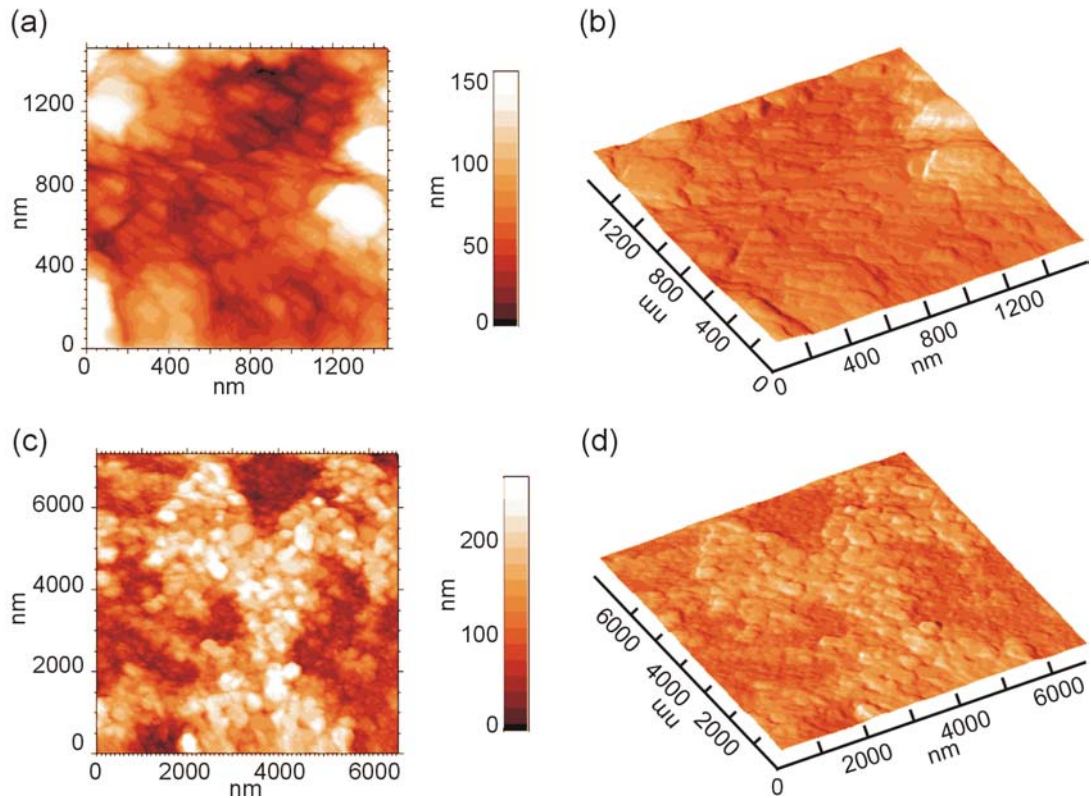
Fig. 5.12. AFM (two-and three-dimensional) images of the surface of the CIS matrix (a)+(b) and the top segregation (c)+(d) of a typical film sputtered on float glass at 400°C and 200W with a H_2S flow of 20 sccm.

The as-sputtered films directly on float glass have typically a rough surface due to an incoherently segregated top layer. Fig. 5.12 shows the representative AFM images (two- as well as three-dimensional) obtained from the surface of the CIS matrix and the top segregation of a typical film sputtered at 400°C and 200 W with a H_2S flow of 20 sccm. In the images (a) and (b) for the CIS matrix there is a clear preferential grain orientation, which may correspond to the (112) preferential orientation of the films as revealed by XRD (see fig. 5.1 (d)). From the AFM images one can see that the grains of the segregation (~ 350 nm) (Fig. 5.12 (c)+(d)) are much bigger than grains in the CIS matrix (~ 95 nm). For the films sputtered on Mo-coated glass, similar rough surfaces with segregation were observed. In contrast, the surface of CIS layers sputtered on ZnO-coated glass is smoother but the grains are much smaller than those on Mo-coated and bare float

glass. In Fig. 5.13 the typical AFM images (top-view and three-dimensional) of CIS layers on Mo- and ZnO-coated glass substrates, respectively, are presented for comparison. Where the mean value of grains of CIS layers on Mo-coated glass is about 85 nm the layers on ZnO-coated substrates have grains of approximately 55 nm, as listed in table 5.2.
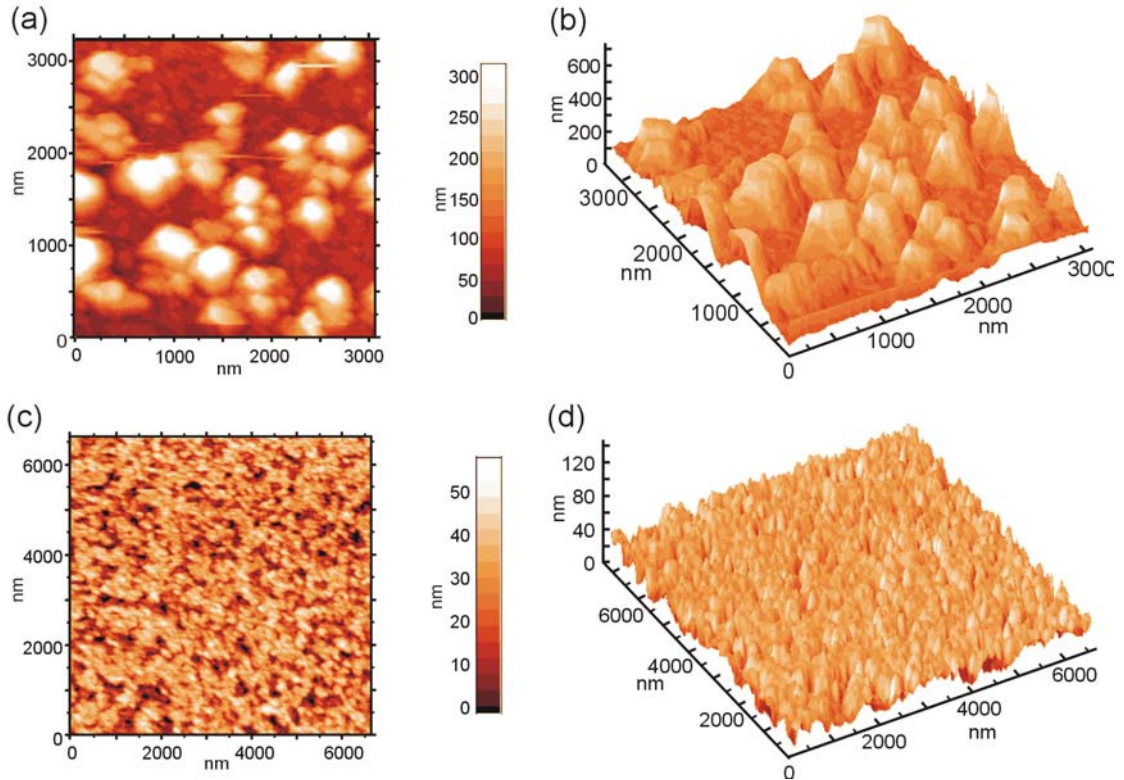

Fig. 5.13. Typical AFM images (top-view and three-dimensional) of surface of CIS layers sputtered on (a)+(b) Mo- and (c)+(d) ZnO-coated glass substrates.

It is well known that Cu_xS is the prevalent secondary phase segregating on Cu-rich CIS films, which results in an improved structure, i.e., enhanced grain sizes of the polycrystalline films. For the selenide films, Klenk *et al*., explained this phenomenon via the formation of a CuSe liquid on top of Cu-rich films [24, 25]. Since our as-sputtered films are on average Cu-rich at the surface (measured from the surface by EDX), we therefore speculate the segregation on our films is just Cu_xS. This has been confirmed by direct EDX compositional examination [26] and indirect approach by comparing the XRD spectra of as-grown and KCN etched films [27], as will be presented later.

5.2.3   Surface segregation analysis by SEM and EDX

As revealed by AFM, the as-sputtered films have typically a rough surface due to island-like precipitates on the film surface. It is very interesting and important to clarify the composition of the surface segregation with respect to the matrix. With integrated EDX function, SEM is very powerful for observation and identification of the surface segregation.
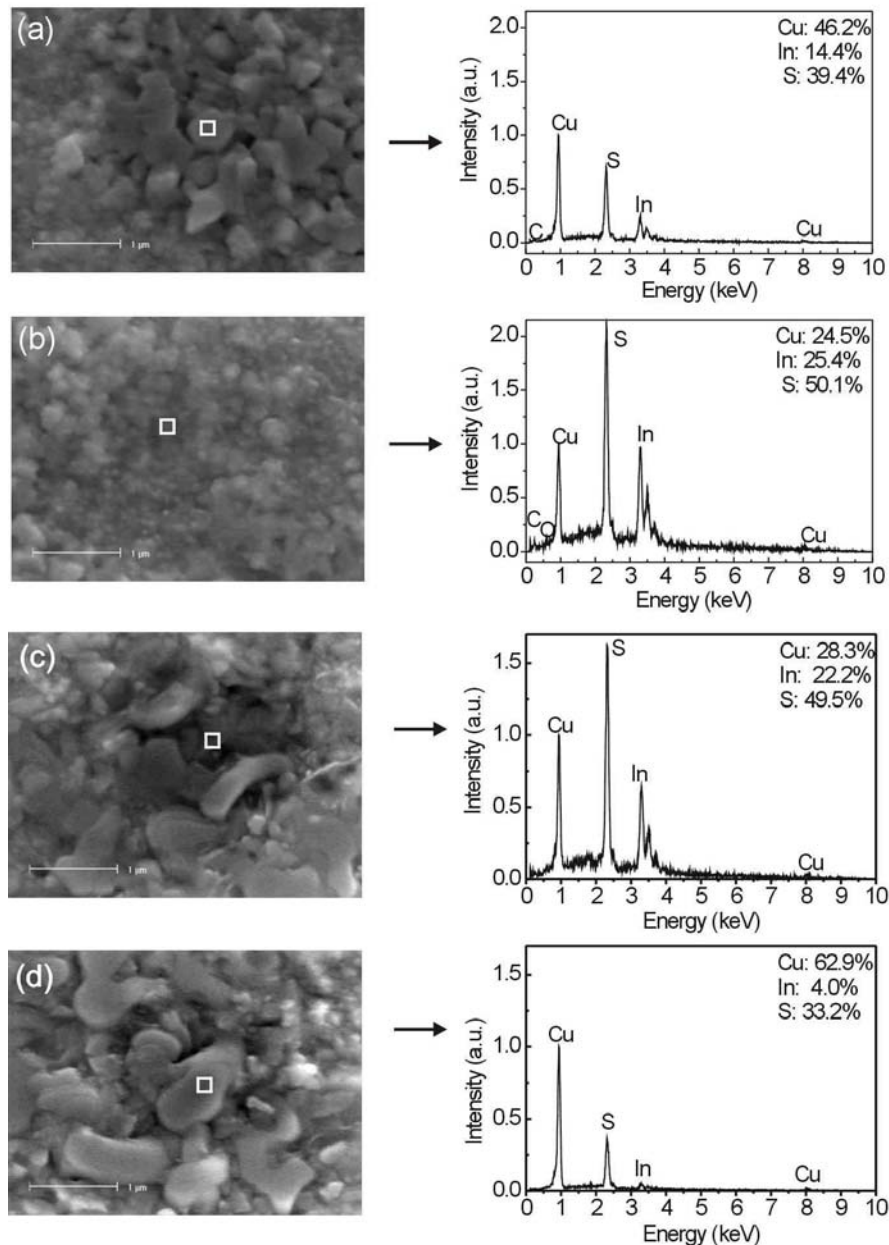

Fig. 5.14. SEM images of segregation (a) and CIS matrix (b), and the corresponding EDX spectra of a film sputtered at 400°C and 200 W with a H_2S flow of 25 sccm; SEM images of CIS matrix (c) and segregation (d), and the corresponding EDX spectra of a film sputtered at 500°C and 200 W with a H_2S flow of 28 sccm.

We focused our EDX measurements on "particles" of segregation and matrix, respectively. Fig. 5.14 (a) and (b) present the "particle" and matrix where we measured and the corresponding EDX spectra obtained for a film sputtered at 400°C and 200 W with a H_2S flow of 25 sccm. In order to see the difference between these two spectra easily, we normalized both spectra according to the Cu peak. There is a significant difference between these two spectra with respect to the Cu to In ratio. While EDX shows slightly In-rich stoichiometry in the matrix the "particle" in the segregation is extremely Cu-rich, strongly deviating from stoichiometry. Quantification results of EDX give: Cu 24.5%, In 25.4%, S 50.1% for the matrix, and Cu 46.2%, In 14.4%, S 39.4% for the "particle", respectively. Therefore, we concluded the segregation on our film surface is an extremely copper rich CIS phase, in which Cu-S binary compounds, e.g., Cu_2S or CuS, may coexist. This conclusion was further confirmed by the similar observation on typical films sputtered at 500°C and 200 W with H_2S flow of 28 sccm. As displayed in Fig. 5.14 (c) and (d), while the CIS matrix is just slightly Cu-rich, the "particle" in the segregation contains nearly no Indium. EDX gives quantitative composition of the "particle": Cu 62.9%, In 4.0%, S 33.2%, with a Cu/S nearly 2, indicating the segregation is Cu_2S rather than $CuInS_2$.

It is well established that potassium cyanide (KCN) is very effective for removing the segregation of Cu_xS on the CIS surface [28]. We used KCN to etch our films and measured SEM and EDX again for comparison. As will be discussed in detail below, within the accuracy of EDX, it revealed nearly identical composition of the etched "particles" with the matrix.

5.2.4   Surface structural properties by GIXRD and XRR

Since at small incident angles comparable to the critical angle of total reflection X-rays only penetrate into condensed matter by the order of hundreds angstroms [29], all X-ray techniques (like X-ray diffraction, absorption, fluorescence analysis, topography…) are surface sensitive when they are applied at grazing incidence. Our initial idea was to detect minor phases segregated on the films by GIXRD. Fig. 5.15 shows the GIXRD spectrum of a typically sputtered CIS film on float glass substrate, recorded with a grazing incidence angle of 0.31°, which is just slightly larger than the critical angle of total reflection (see below), in comparison with its spectrum recorded under normal θ-2θ scan. As previously discussed, the sputtered films are preferentially (112)-oriented. By the conventional θ-2θ scan, only peaks of (112) and (224), which originate from the same series of lattice planes of CIS, were unambiguously detected in the film. Due to probably too small abundance of the minor phase and /or limited resolution of our diffractometer, we failed to achieve our

initial goal to detect any segregated secondary phase at the surface. However, by using detector scan geometry instead of conventional θ-2θ scan, we got more peaks, well according to the standard spectrum of powder CIS, and thus, confirming that the two peaks in Fig. 5.15 (a) originate, indeed, from (112) and (224) of chalcopyrite CIS. Caused by the unfocused geometrical arrangement during detector scan, the peaks shown in the GIXRD spectrum are, as usual, much broader than those in normal XRD spectrum.
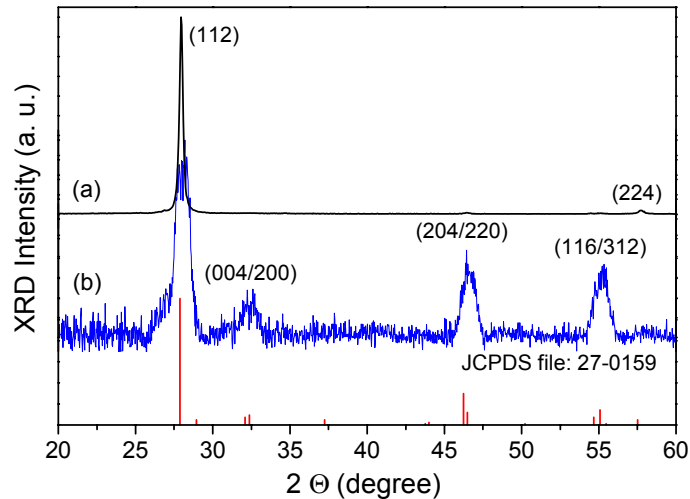
Fig. 5.15. XRD pattern of a film sputtered at 400°C and 200 W with a H_2S flow of 25 sccm, (a) conventional θ−2θ scan, (b) GIXRD with an incidence angle of 0.31°. A standard spectrum of CIS (JCPDS file 27-159) is inserted for comparison.

The XRR technique is now a well-established method for the determination of the thickness, density, surface and interface roughness of thin films and layered structures [30]. The XRR measurements (grazing incidence θ-2θ scan) on our CIS thin films were typically carried out from 2θ = 0.35° to 2.0° with a scan step of 0.002°. Fig. 5.16 shows the measured and simulated XRR spectra of a relatively thin CIS film sputtered at 400°C and 200 W with a H_2S flow of 25 sccm for 3 min. The simulated and measured curves are in good agreement with respect to the position of the total reflection angle (θ around 0.298°) and the maxima or minima of the oscillations. However, the amplitudes of both curves differ more or less, which is due to the limited resolution of the measurement system, and possibly to non-Gaussian roughness of the inhomogeneous film surface and the film/substrate interface [31]. The simulated surface density and roughness as well as film thickness are inserted in the figure. The surface density of 5.01 g/cm^3 is slightly higher than the theoretical value of CIS (4.74 g/cm^3), indicating some minor phases with a density higher than CIS, e.g., Cu_2S has 5.79 g/cm^3, segregated on the film surface. The sputtered

film has a rather rough surface with a root mean square (RMS)-roughness around 3.80 nm, which might imply also the surface segregation. These observations support our above conclusion on the films surface segregation. From the measured thickness we can calculate the deposition rate of our one-stage sputter process, which is approximately 33 nm/min. It is comparable or even higher than that in the case using argon as working gas, supporting our idea to use H_2S solely as both working and reactive gas during sputtering.
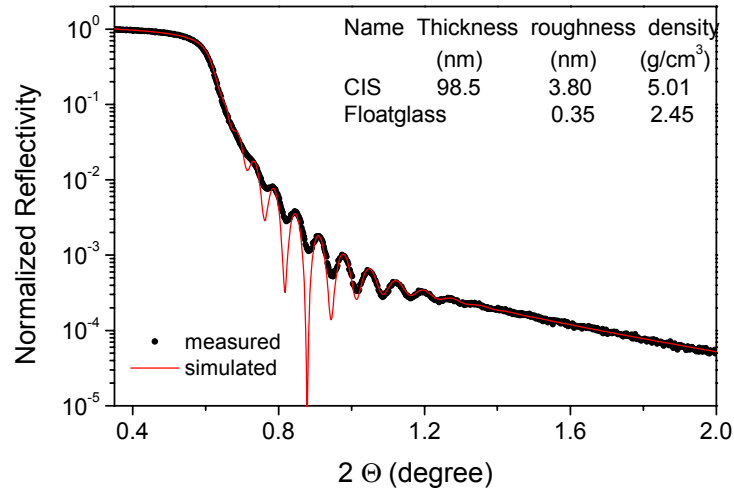
Fig. 5.16. Measured and simulated XRR spectra of a thin CIS film with simulation parameters for layer thickness, roughness, and density.

5.2.5 Surface survey and depth profile by SIMS
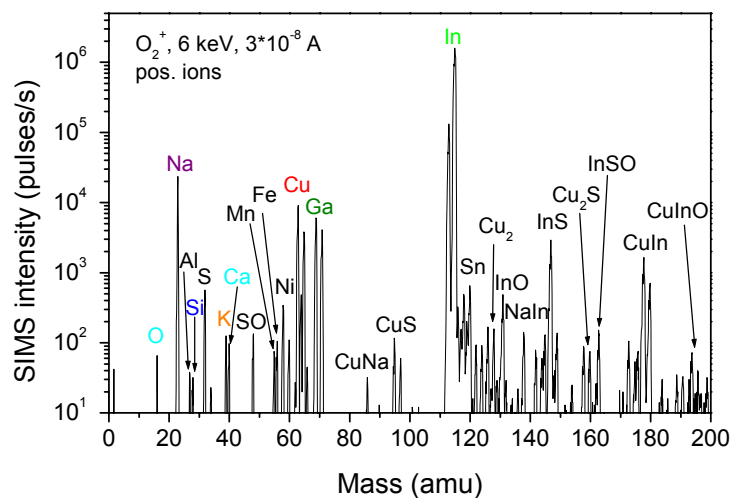
Fig. 5.17. Typical SIMS mass spectrum recorded for the surface of CIS films sputtered on float glass.
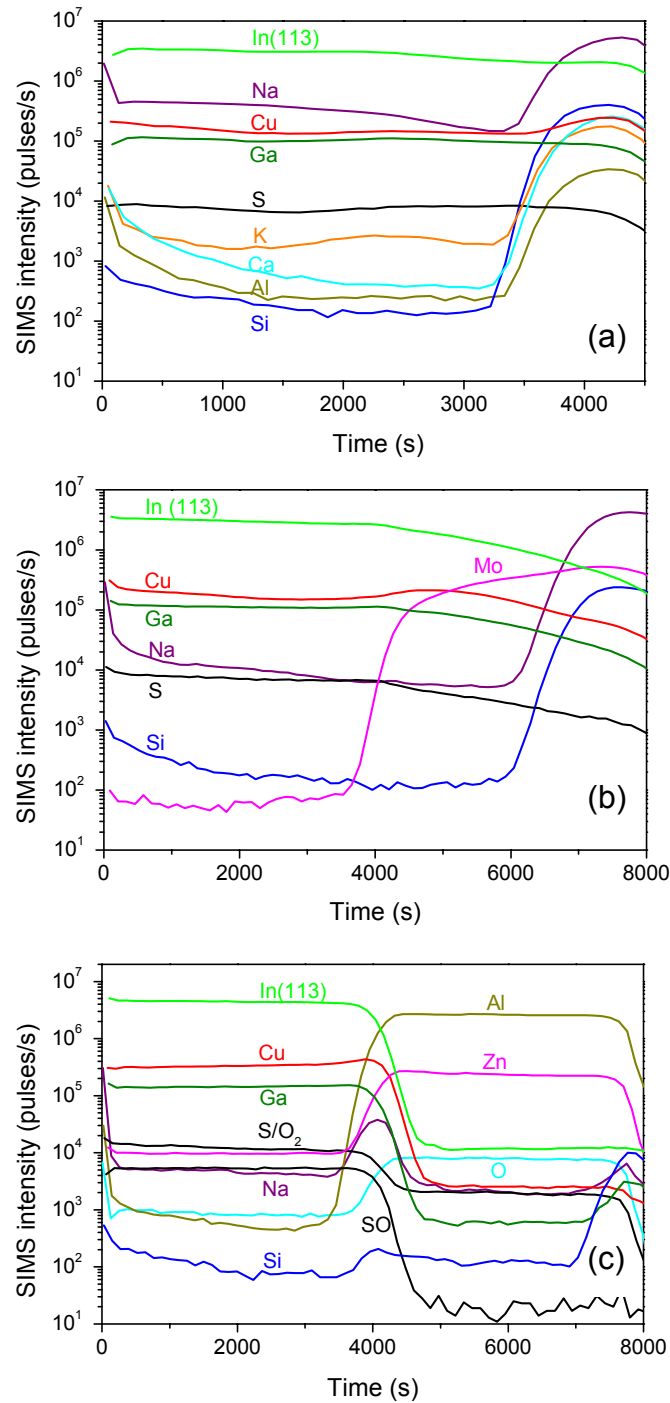
Fig. 5.18. SIMS depth profiles of CIS films sputtered on (a) bare, (b) Mo-, and (c) ZnO-coated float glass substrates, demonstrating a good depth homogeneity of the sputtered layers.

We performed SIMS to examine the surface impurities as well as the depth homogeneity of the sputtered films. Fig. 5.17 shows the positive ions mass spectrum for the surface of a typical film sputtered on float glass, recorded with a 6 keV O_2^+ ion beam and 3×10^{-8} A current. Apart from the main elements Cu, In, and S and their compounds, impurities such as O, Na, K, Ga, Ca, Al, Si, Mn, Ni, Fe, and Sn were detected at the surface. SIMS is

extremely sensitive to Na and K, thus, they can be detected at a very low concentration. Together with Ca, Al, and Si, Na and K diffused from the float glass substrate to the film surface. Ga is a common impurity of In, which also has a high sensitivity in SIMS. O was partly contaminated from the air and partly diffused from the float glass. Mn, Ni, and Fe could be caused by contamination of the sputter chamber and the target holder. Sn arises from the tin-side of the float glass substrates used for the sputtering.

The depth profile of the same sample is shown in Fig. 5.18 (a). Na was found as a major contamination throughout the film due to diffusion, since no diffusion barrier was pre-sputtered onto the float glass substrate. The depth profiles of all three elements Cu, In, and S are nearly constant throughout the film revealing a good homogeneity and constant composition of the sputtered film.

Similar depth distribution homogeneity was observed for films sputtered on Mo- and ZnO-coated glass substrates, as shown in Fig. 5.18 (b) and (c). In addition, as can be seen from the figure, the Na intensity in CIS layers on Mo-or ZnO-coated float glass is lower than that in CIS layers on bare glass by more than a factor of 20. Thus, the Mo or ZnO buffer layers act effectively as a barrier to prevent Na diffusion from the float glass into the sputtered CIS layers.

5.2.6   Conclusions

CIS films deposited by a one-stage RF reactive sputter process generally have a rough surface due to an incoherently segregated top layer, as observed by AFM. XRD reveals a (112) preferential orientation of the sputtered films. XRR measurement gives the film surface density around 5.01 g/cm^3, which is higher than the theoretical value for pure CIS, indicating a secondary phase existing in the film surface. Additionally, from the measured thickness by XRR the deposition rate of the one-stage sputter process was calculated to be approximately 33 nm/min. SEM and EDX were used to directly identify the segregation on the film surfaces, which disclosed that the Cu/In ratio in the surface precipitates deviated extremely from that in the matrix. Despite of the Cu$_x$S surface segregation, XPS revealed that the film surfaces remain In-rich with respect to the bulk, and the surface properties are dominated by oxidation after exposure to air. SIMS manifested a good depth homogeneity of all the films sputtered on bare, Mo- or ZnO-coated glass substrates.

5.3   Post-growth treatment effects on properties of the sputtered CuInS$_2$ films

In order to achieve high-efficiency solar cells, post-deposition treatments of the absorber layers are mostly required. For example, CuInSe$_2$-based thin film solar cells prepared by many techniques need a post-deposition annealing in air or O$_2$ to optimize their photovoltaic performance [32]. For fabrication of efficient CuInS$_2$-based thin film solar cells, Cu-rich films are usually grown, for which etching of the Cu-excessive absorber with the potassium cyanide (KCN) is necessary to remove the surface segregation of Cu$_x$S [33]. Although we have succeeded in depositing CIS films by RF reactive sputtering in one step, i.e., neither annealing nor sulfurization is necessarily needed after sputtering [8], there still remain some questions to our one-stage process. For instance, whether there is a further improvement of the film crystalline quality by post-growth annealing or whether KCN can substantially remove the Cu$_x$S secondary phases segregated on the sputtered film surfaces. In addition, how do they influence the optical as well as electrical properties of the sputtered films? Following these questions, we performed different post-deposition treatments on the as-grown films: annealing in vacuum, air, or H$_2$S environments for different periods, etching with KCN solution, as well as aging the films under normal atmosphere, and compared the structural, optical as well as electrical properties of the as-grown and post-treated films.

5.3.1   Post-growth annealing effect on the structural and optical properties

After the sputter deposition, the films used for the aging purpose were stored directly under normal air, while the others were kept in a roughly evacuated and Si gel-dried exsiccator. Several weeks later, the films were subjected to anneal in the same sputter chamber under vacuum around 10^{-4} Pa, air, or H$_2$S gas at a temperature between 200 and 500°C for durations of half to several hours. A 1% KCN aqueous solution was used to etch the films within 10 to 30 min at room temperature. After etching, the samples were rinsed in de-ionized water.

5.3.1.1 Annealing with H_2S

As we have previously discussed, there are mainly Cu-In alloy secondary phases coexisting in the films when the H_2S flow rate is insufficient during sputtering [12]. In this section, we demonstrate such Cu-In alloy phases can be eliminated by annealing the films with H_2S. Fig. 5.19 shows the XRD spectra recorded from a layer originally sputtered at 500°C and 300 W with a H_2S flow rate of 40 sccm. In the spectrum of as-grown film, additional peaks originating from Cu-In phases, such as $Cu_{11}In_9$ and CuIn, are seen. We annealed this film at 500°C in H_2S atmosphere with a H_2S flow rate of 30 sccm, 3.07×10^{-1} Pa in partial pressure. The peak around 42.7° of $Cu_{11}In_9$ still existed there, after 3 hours annealing/sulfurization. However, it diminished after two hours additional annealing, and finally vanished completely.
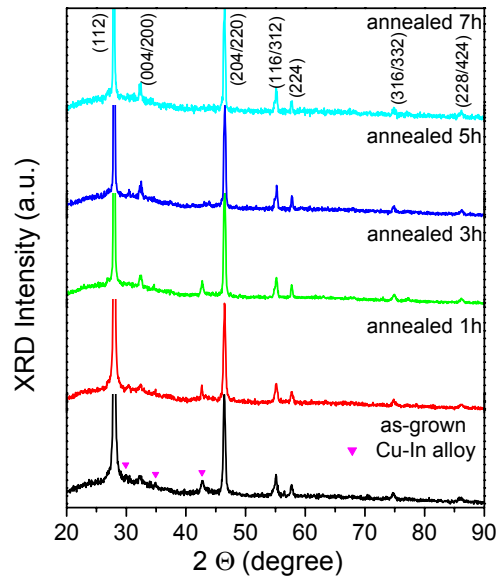
Fig. 5.19. XRD spectra of a CIS film originally sputtered at 500°C and 300 W with a H_2S flow of 40 sccm, recorded for as-grown and after annealing in H_2S atmosphere at 500°C for different periods.

In Fig. 5.20 the room temperature optical transmission spectra of this film with respect to different sulfurization periods are compared. At the as-grown stage, the film absorbs the light in a broad wavelength range, thus, it is hard to determine the absorption edge. The overall transmission is relatively low. This can be attributed, on the one hand, to incorporation of Cu-In metallic phase in the film and, on the other hand, to poor quality of the as-grown CIS phase base material. The grains in our as-grown films are rather small (~100 nm), giving rise to an abundant volume of grain boundaries in the film. By sulfurization at a high temperature of 500°C for 3 hours or more, the Cu-In alloy phase vanished and the grain boundaries were reduced significantly. Thus, the absorption edge

became sharper and the transmission increased. Following the approach usually used for evaluating the band gap by transmission data [34], we deduced the direct band gap of the sufficiently sulfurized film at room temperature to be 1.49 eV (see the insert in the figure), which is nearly identical to the value of bulk crystals, indicating a good quality of the film.
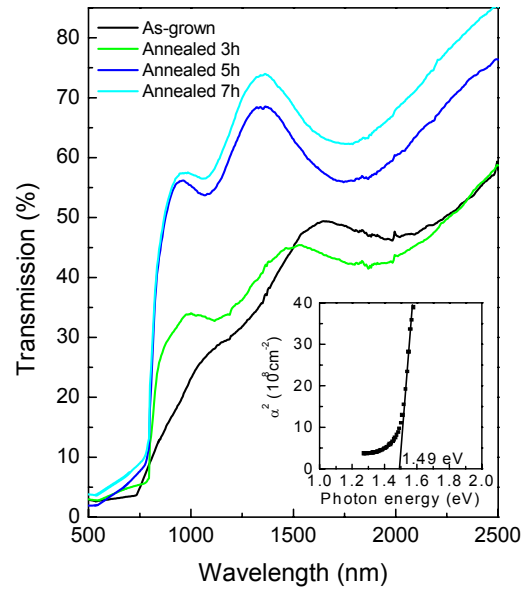

Fig. 5.20. Optical transmission spectra of the film in Fig. 5.19 with respect to annealing in H_2S atmosphere at 500°C for different periods. The bandgap estimation for the 7h annealed film is inserted.

5.3.1.2 Annealing under vacuum
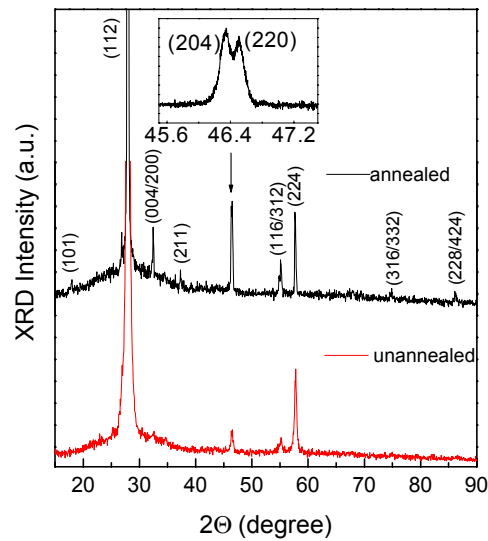
Fig. 5.21. XRD spectra of a KCN etched CIS film sputtered at 400°C and 200 W with a sufficient H_2S flow of 25 sccm, recorded before and after annealing in vacuum at 500°C for 2h.

With sufficient H_2S flow during sputtering, as described already in former sections, pure $CuInS_2$ phase films could be sputtered in one step. In this section, we study the post-growth anneal effect on these one-stage sputtered nearly stoichiometric CIS films. Fig. 5.21 depicts the XRD spectra of a KCN etched film recorded before and after annealing under vacuum at 500°C for 2 hours. From the spectrum recorded after annealing, one can clearly see, besides the peaks present in the unannealed film, there are more peaks from (101), (211), (316/332), and (228/424) reflections appearing, and the splitting of (004/200), (204/220) (see the insert), and (116/312) peaks is unambiguously discernable. It is worthy to note that the splitting of (204) and (220) planes is a characteristic sign for tetragonal structure, determining undoubtedly a tetragonal chalcopyrite structure of the sputtered films rather than cubic zincblende. In addition, upon annealing the FWHM of (112) peak was reduced from 0.239° to 0.133°, and the corresponding grain sizes increased from approximately 60 to 250 nm as deduced by the Scherrer formula [13]. It hence indicates that annealing at a high temperature (500°C) for a certain time causes recrystallization of the sputtered films and improves the structural properties of the films.
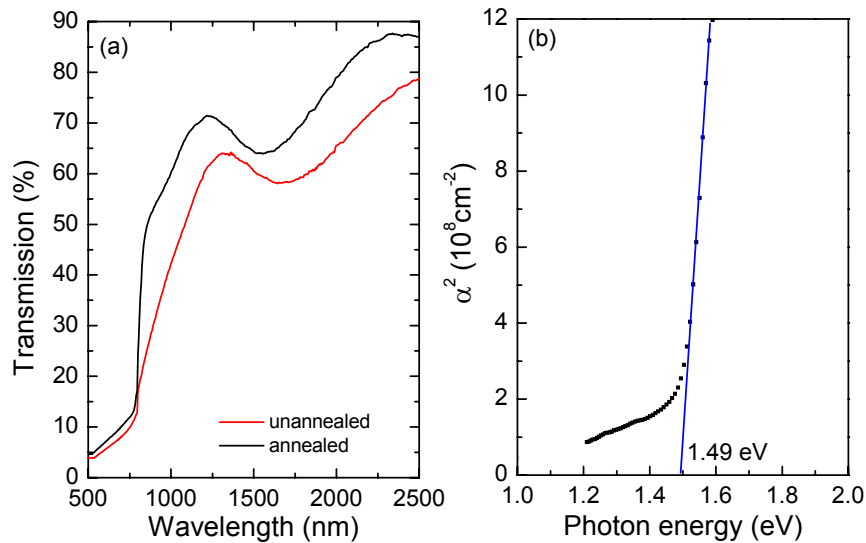

Fig. 5.22. (a) Optical transmission spectra of the film in Fig. 5.21 measured before and after annealing in vacuum at 500°C for 2h. (b) Bandgap estimation for the film after annealing.

The improved structural quality of the annealed films further leads to significant enhancement of the film optical properties. In Fig. 5.22 (a) the room temperature transmission spectra of this sample as measured before and after annealing are compared. Upon annealing, the absorption edge of the film became sharper and the overall transmission increased. Similar to the films annealed in H_2S, the films annealed under vacuum have a direct bandgap of approximately 1.49 eV, as illustrated in Fig. 5.22 (b).

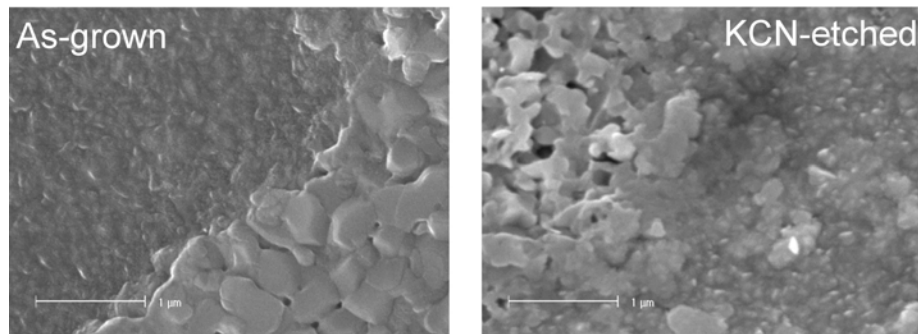## 5.3.2 Chemical etching of Cu$_x$S segregation by KCN

Fig. 5.23. SEM micrographs of the surface of a typical film sputtered on float glass substrate, imaged before and after KCN etching.

We performed SEM to survey directly the etching effect on the film surfaces. Fig. 5.23 shows two representative micrographs of a typically one-stage sputtered film imaged before and after etching with KCN. In the image of the as-grown film, there are densely compacted segregations on the film surface. In preceding sections, we have identified the surface segregations being of Cu$_x$S phases by EDX. After etching, the surface segregations became porous. We, hence, performed EDX measurements as well on the etched but maintained "particles" and the matrix to compare. The composition of the etched "particles" and the matrix is nearly identical within the accuracy of EDX, indicating a removal of Cu$_x$S surface phases.
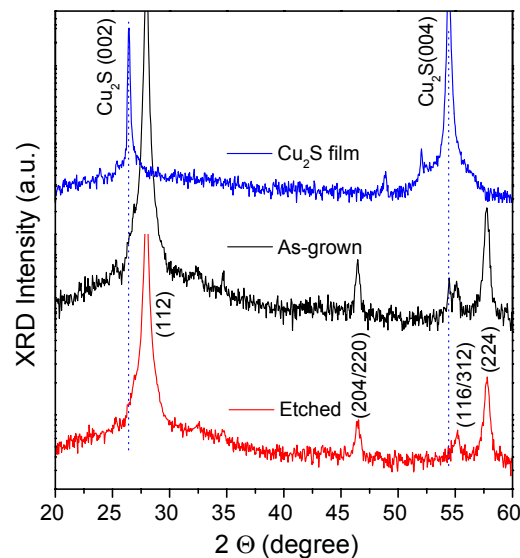

Fig. 5.24. XRD spectra of the same sample in Fig. 5.23 recorded before and after KCN etching. A spectrum of Cu$_2$S film sputtered with the same setup is included for comparison.

Removal of Cu_xS by KCN etching is further confirmed by XRD measurements on the etched and unetched films. Fig. 5. 24 displays the XRD spectra recorded for the same sample as in Fig. 5.23 before and after KCN etching. The spectrum of a Cu_2S film sputtered with the same setup and comparable conditions is included for comparison. In the spectrum of the as-grown film, there are two neighboring peaks centered around 55°, which seem to originate from the splitting of CIS (116/312). However, by comparing with the Cu_2S spectrum, it is clarified that the left peak arises actually from Cu_2S (004), which disappears completely after KCN etching. This observation allows us to conclude, indeed, there is a Cu_2S secondary phase segregated on the surface of the as-sputtered films, and this Cu_2S phase can be removed effectively by KCN etching.
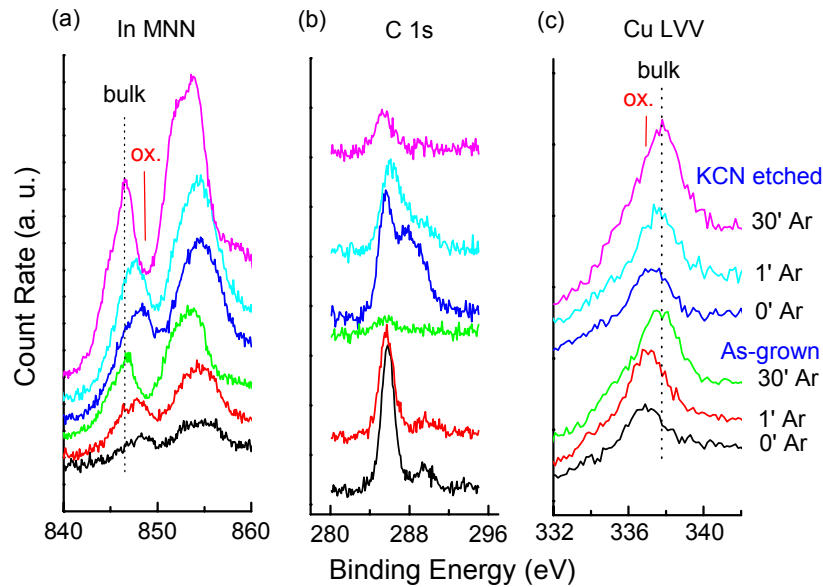

Fig. 5.25. XPS spectra of (a) In MNN, (b) C 1*s*, and (c) Cu LVV signals, recorded from a KCN etched film (upper three lines) and an unetched film (lower three lines) after different periods (0-30 min) of Ar-bombarding.

For further understanding of the KCN-treatment effect on the surface properties of our CIS films, we compared the surfaces of an etched and an unetched sample by XPS measurements. The comparison was done before and after sputter-cleaning the samples by Ar-ions with energy of 3 keV. The corresponding spectra are presented in Fig. 5.25. 20 min sputtering removed the surface phases completely. As both samples were exposed to air before transferring them into the vacuum chamber, the surface exhibits oxides of all the three elements. Whereas the Cu 2*p* and the S 2*p* lines at the surface shift a little with respect to in the bulk, the strong oxidation of In can be seen from the Auger-lines (In

MNN) (see Fig. 5.25 (a)) and decreases with Ar-bombarding. As shown in Fig. 5.25 (b), the carbon signal from the surface of the KCN-etched sample is much broader than that of the unetched one. Obviously the etching process induces carbon-compounds on the surface, whereas the air-exposed sample is covered only by carbon adsorbates. K and N residues from KCN were not found.

Special interest was put on the secondary copper phases. In ref. [20] it was reported that when there is a copper binary phase, e.g., CuS, incorporated in the CIS films the Cu-L_3VV-Auger spectrum will have a corresponding shift with respect to that of pure CIS films. Fig. 5.25 (c) shows the shifting of the Cu-L_3VV-Auger signals in our films. It is evident, that copper is in a different binding state on the surface compared to the bulk. The Cu surface signal could be attributed either to Cu-S or Cu-O or both compounds.

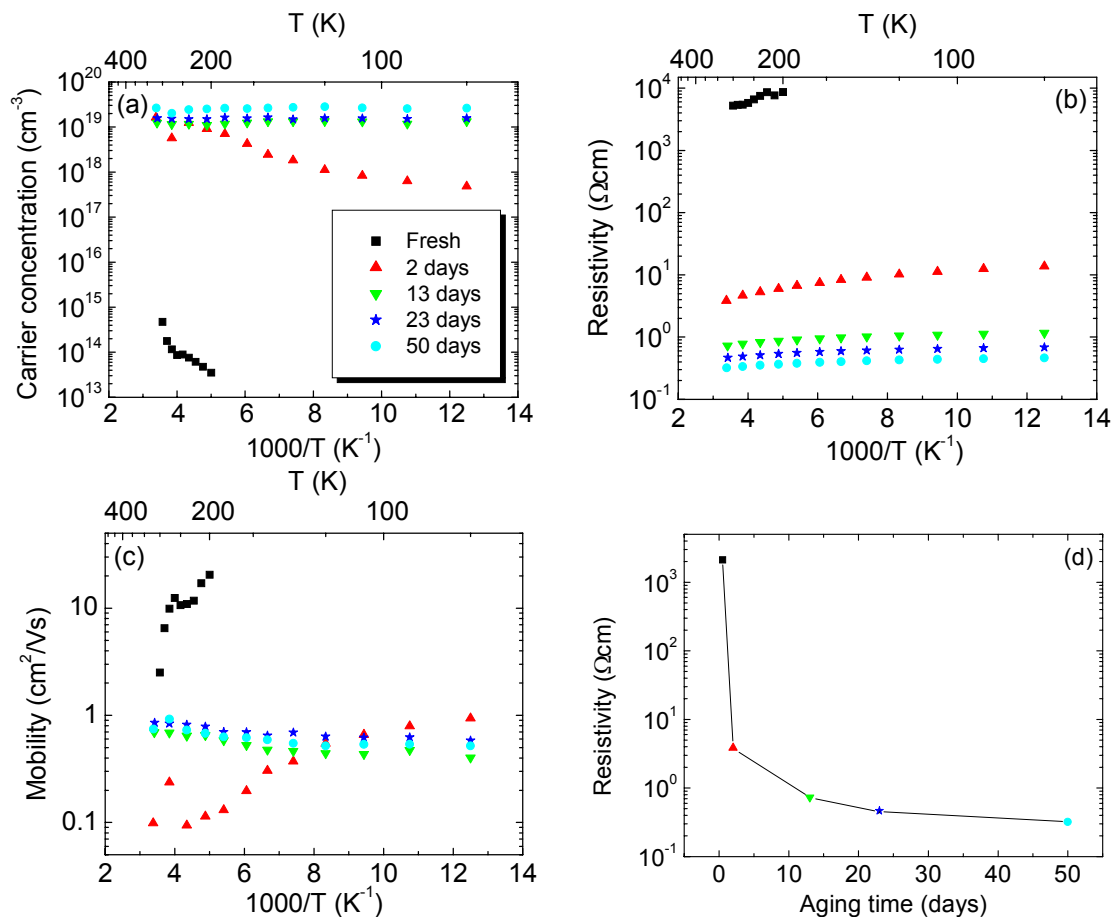## 5.3.3 Aging and etching effects on the electrical properties

Fig. 5.26. Carrier concentration (a), resistivity (b), and mobility (c) as a function of temperature and aging time in air of a film sputtered at 400°C and 200 W with H_2S flow of 25 sccm. Plot (d) demonstrates the rapid change of the film resistivity at room temperature with aging in air.

Hall effect measurements were implemented to characterize the electrical transport properties of the fresh and air-aged as-grown films, post-etched as well as annealed samples. The fresh films (directly after sputtering) are, in general, highly resistive n-type conducting, with the resistivity, carrier density, and mobility at RT in the range of 2×10^3-10^4 Ωcm, 3×10^{14}-10^{15} cm^{-3}, and 2-20 cm^2/Vs, respectively, as listed in table 5.4. After exposure to air for several weeks, they converted to be highly conductive p-type, and their resistivities, carrier densities, and mobilities approached values 0.1-2 Ωcm, 3×10^{19}-10^{20} cm^{-3} and 0.2-0.7 cm^2/Vs, respectively. Fig. 5.26 shows the carrier density, resistivity, and Hall mobility as a function of the temperature and the storage time in air of a typically sputtered film. At the fresh stage, the film was nearly intrinsic and could only be measured in a narrow temperature range around RT due to its very high resistivity. Its resistivity, carrier density, and mobility varied in the range of 8700-2100 Ωcm, 3.5×10^{13}-10^{15} cm^{-3} and 20.5-3.3 cm^2/Vs within the temperature of 200-295 K. After two days, it maintained electron (n-type) conduction. However, its resistivity and mobility decreased rapidly while its carrier density increased drastically by almost 5 orders of magnitude (Fig. 5.26 (a)). The temperature tendency of the Hall mobility suggests a predominant acoustic phonon scattering mechanism involved in the film. After aging in air for about two weeks, the film resistivity continued to decrease while its carrier density increased further, and even more strikingly, the film converted to hole conduction (p-type). Nearly one month later, its resistivity, carrier density and mobility tended to saturate and approached a stable level around 0.2 Ωcm, 3×10^{19} cm^{-3} and 0.7 cm^2/Vs, respectively, remaining p-type conducting. In Fig. 5.26 (d), the dramatic aging effect on the film resistivity at room temperature is demonstrated as a function of aging time. Similar aging effects on the resistivity were observed by Ogawa *et al.* in their sulfurized CIS films [14].
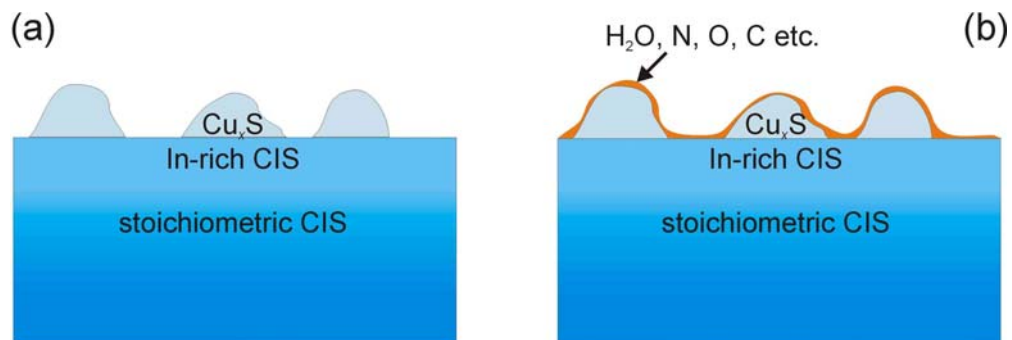

Fig. 5.27. Schematic model for the interpretation of electrical properties of sputtered films based on film stoichiometry and surface segregation.

Based on the previously described results of surface morphology by AFM, compositional analysis by EDX, RBS, and XPS, we suggest the following model to interpret the electrical properties we obtained for the sputtered CIS films. As illustrated in Fig. 5.27, there are islands of Cu_xS segregating on top of an In-rich surface layer, while our films are nearly stoichiometric in the bulk. At the very fresh stage, the In-rich layer together with the CIS matrix plays a major role in the electrical transport and gives rise to an *n*-type conducting of the films, since the top segregated Cu_xS islands are isolated from each other. After exposure to air, these Cu_xS islands have been activated by the connection of species adsorbed from air, e.g., oxygen, carbon, organic stuff, water vapor, and so on, and dominate the electrical transport in the films [9]. As we reported previously, Cu_xS, especially CuS, is a highly *p*-type conducting and metal-like semiconductor with a hole concentration as high as 10^{19} (Cu_2S) to 10^{22} cm^{-3} (CuS) at room temperature [35]. Showing a highly *p*-type conducting with a resistivity of 0.2 Ωcm and carrier density of 3×10^{19} cm^{-3} and being nearly constant with temperature, the sputtered films stored in air for a certain time behave just like Cu_xS. It thus means the electrical data we measured on those air-exposed samples are governed by the top segregated Cu_xS layers rather than the bulk CIS films. Annealing in air or vacuum at a moderate temperature of 200°C for 30 min, isolating again the Cu_xS segregation via releasing the adsorbates from the film surface and grain boundaries, leads to a reverse change of the film electrical properties in relation to aging in air. In particular, KCN etching removed the surface Cu_xS segregation and recovered almost completely the electrical properties to the initial as-grown values, supporting the above-proposed model.

In Fig. 5.28, the temperature dependence of carrier density, resistivity, and mobility of the same sample as in Fig. 5.26 measured after KCN etching is presented, in comparison with the unetched values. Upon etching, the film reverted from *p*-type conduction in the air-exposed state back to the initial *n*-type. Again its resistivity was high and could only be measured in a narrow range around room temperature. Its resistivity, electron density, and mobility are corresponding reasonably to the values of fresh as-grown film. The aging and etching behavior of this film is representative rather than occasional among our sputtered films. This can be seen from table 5.4, in which the typical room-temperature electrical properties of sputtered films at fresh stage, after exposure to air, and additional KCN etching are summarized.

We would note here that the aging effect occurred on our films might be responsible, in part, for the wide range of reported electrical transport data for CIS films deposited by various methods (see chapter 2). It indicates that the electrical properties correlate not only to the different deposition techniques used and the film stoichiometry, but also to the specific status of the measured samples, i.e., fresh, air-aged, or chemical etched. Thus,

attention should be paid to the measuring conditions when one compares the electrical data of CIS films, especially for films with Cu_xS segregations.
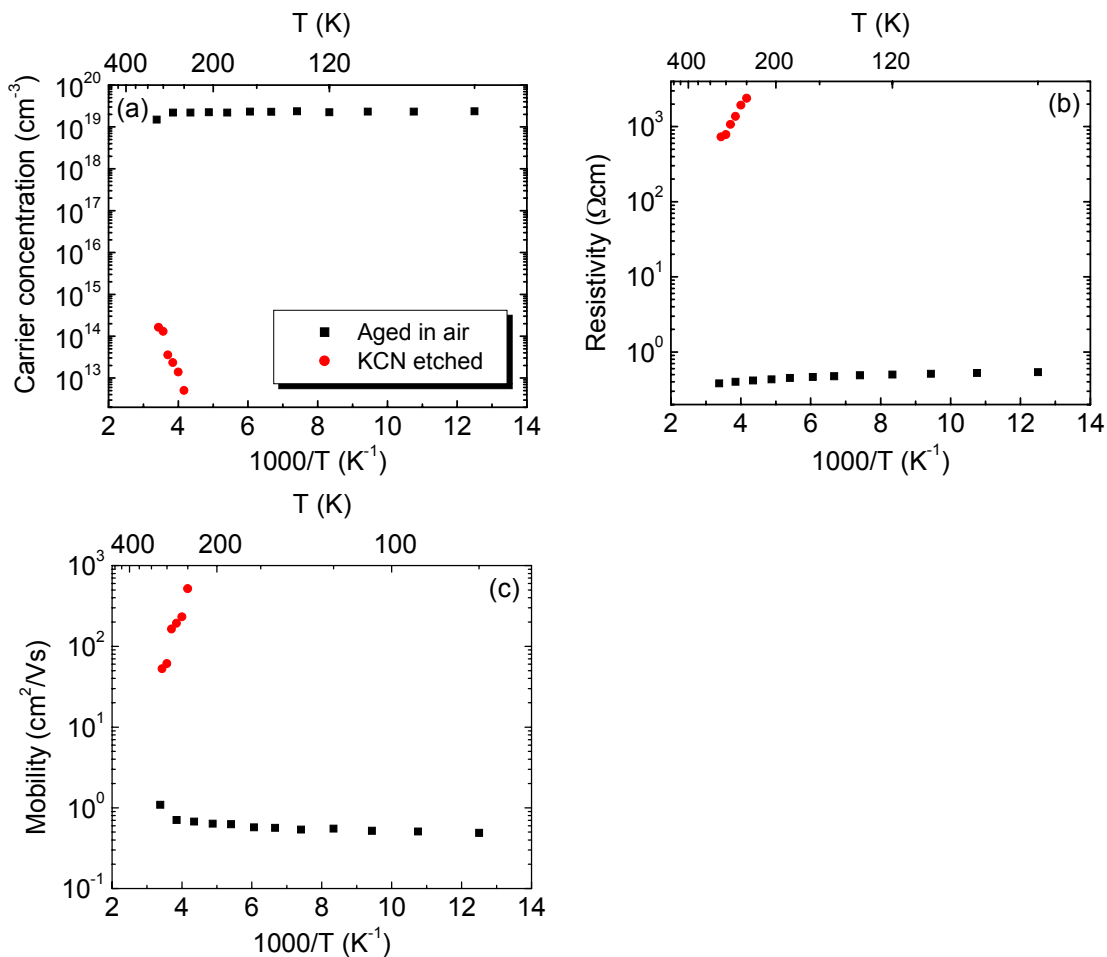

Fig. 5.28. Temperature dependence of carrier density (a), resistivity (b), and mobility (c) of the same sample as in Fig. 5.26 measured after KCN etching, in comparison to air-aged values.

Table 5.4. Summary of the typical room temperature electrical properties of sputtered films at fresh stage, after exposure to air, and additional KCN etching.

Film	Resistivity (Ωcm)	Carrier density (cm^{-3})	Hall mobility (cm^2/Vs)	Conduction type
Fresh	2×10^3-10^4	3×10^{14}-10^{15}	2-20	*n*
Aged in air	0.1-2	10^{19}-10^{20}	0.2-0.7	*p*
KCN etched	6×10^2-2.5×10^4	4×10^{13}-3×10^{15}	2-100	*n*

5.3.4 Conclusions

Although stoichiometric pure $CuInS_2$ phase films can be produced in one step by RF reactive sputtering, post-deposition treatments affect significantly the structural, optical, and electrical properties of the sputtered films. Heating under vacuum at a temperature of 500°C for 2 hours causes recrystallization of the as-sputtered films and consequently improves the optical properties. Annealing in H_2S atmosphere at 500°C for suitable duration results in the elimination of the secondary Cu-In phases coexisting in the films sputtered with an insufficient H_2S flow during sputter deposition, meanwhile, enhancing the film structural as well as optical properties. The direct band gap of the annealed films is evaluated to be 1.49 eV at room temperature, nearly identical to the value of bulk material. Upon exposure to air, the electrical properties of the as-grown films change tremendously, switching from highly resistive electron dominated (*n*-type) conducting to highly *p*-type conducting. KCN etching removed effectively the Cu_xS segregation on the film surfaces and recovered the film electrical properties to the initial state.

6 Quasi-epitaxial growth of CuInS$_2$ films on sapphire

As described in the introduction (chapter 1), the ternary compound semiconductors CuXY_2 (X= In, Ga; Y= S, Se) and their multinary alloys have recently attracted considerable interest due to their applications in optoelectronic devices, especially for solar cells [1]. CuInS$_2$ has theoretically the highest conversion efficiency among the chalcopyrite Cu(InGa)(SeS)$_2$-based solar cells [2, 3] primarily due to its direct bandgap of 1.55 eV [4], a superior matching to the solar spectrum, and its high absorption coefficient of almost 10^5 cm^{-1}. It has practically achieved, however, only 11.4% total area conversion efficiency so far [5], considerably less than other chalcopyrite-based solar cells (CuInSe$_2$: 14.8% [6]; Cu(InGa)Se$_2$: 18.8% [7]). To dig up fully its potential a better understanding of the fundamental properties of the absorber itself is essential, which could be achieved from high-quality single-crystalline materials. However, it is well known that the controlled growth of high quality single crystals is a priori difficult for ternary compounds, and is additionally complicated by high temperature phase transitions that occur in many chalcopyrite compounds [8]. It is therefore of great importance to achieve crystalline CuInS$_2$ films alternatively by epitaxial growth. However, such attempts have so far scarcely been reported in the literature. The first successful heteroepitaxial growth of CuInS$_2$ films was reported by Metzner, Hahn and their coworkers on sulphur-terminated Si (111) and Si (100), using the molecular beam epitaxy (MBE) technique [8, 9]. With the same technique, Hunger *et al.* achieved epitaxial growth of CuInS$_2$ on hydrogen-terminated Si (111) [10]. Compared with MBE, sputtering is not a typical technique for epitaxial growth. Nevertheless, with sputtering the "quasi-epitaxial" growth of a wide range of functional materials has been demonstrated, such as semiconductor materials like ZnO [11], GaN [12], AlN [13], superconductors like YBa$_2$Cu$_3$O$_7$ [14, 15] and Bi$_2$Sr$_2$Ca$_2$Cu$_3$O$_x$ [16], ferroelectric films like PZT [17] and BST [18], and rare-earth-transition-metal (RE-TM) films like Sm-Fe [19], Sm-Co [20], and so on. In this study, we demonstrate, to the best of our knowledge, the first "quasi-epitaxial" growth of CuInS$_2$ films on sapphire (0001) by RF reactive sputtering with a Cu-In alloy target and H$_2$S gas.

6.1   Heteroepitaxial growth of very thin CuInS$_2$ films on sapphire

Single-crystalline (0001)-oriented sapphire was used as substrate. Prior to film deposition the sputter chamber was evacuated to about 10^{-4} Pa using a turbomolecular pump together with a liquid nitrogen trap. The sapphire substrates were cleaned ultrasonically in organic solvents, with no further etching and heating treatments before film growth. Like in the case of sputtering CuInS$_2$ films on float glass substrates, the Cu-In alloy disk target was employed, and H$_2$S (purity: 98.0%) was solely introduced as both reactive and working gas during sputtering. While the H$_2$S flow was varied in the range of 30-35 sccm, the RF power was fixed at 200 W (2.47 W/cm^2), and the substrate temperature was kept constant at 500°C. The sputtered CIS layer thicknesses were mainly controlled by varying the sputter time with a typical growth rate of approximately 40 nm/min.
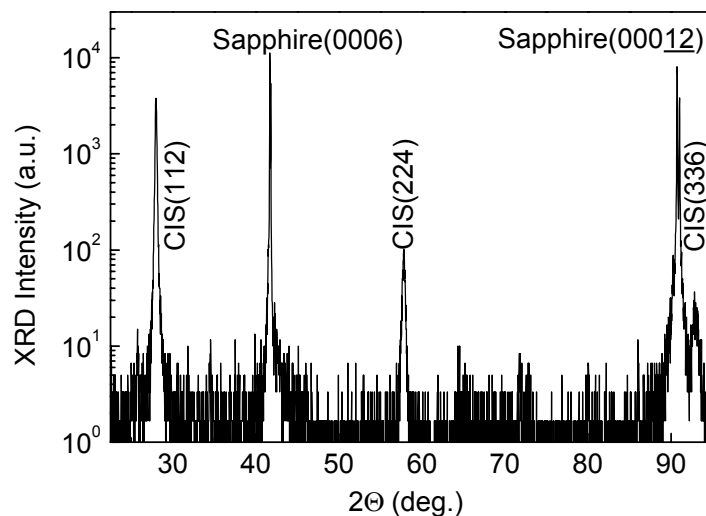

Fig. 6.1. Typical XRD spectrum of sputtered thin CIS films on sapphire.

The crystalline structure of the layers was studied by X-ray diffraction (XRD). Fig. 6.1 shows a typical θ-2θ spectrum of the sputtered films. As can be seen, along with well-known diffraction peaks of the sapphire substrate, the (112), (224), and (336) peaks of the tetragonal chalcopyrite structure of the CIS film are clearly resolved, indicating a preferred

orientation of CIS (112) parallel to sapphire (0001). Despite the chosen logarithmic scale, the XRD spectrum shows no signs of polycrystalline CIS phases.
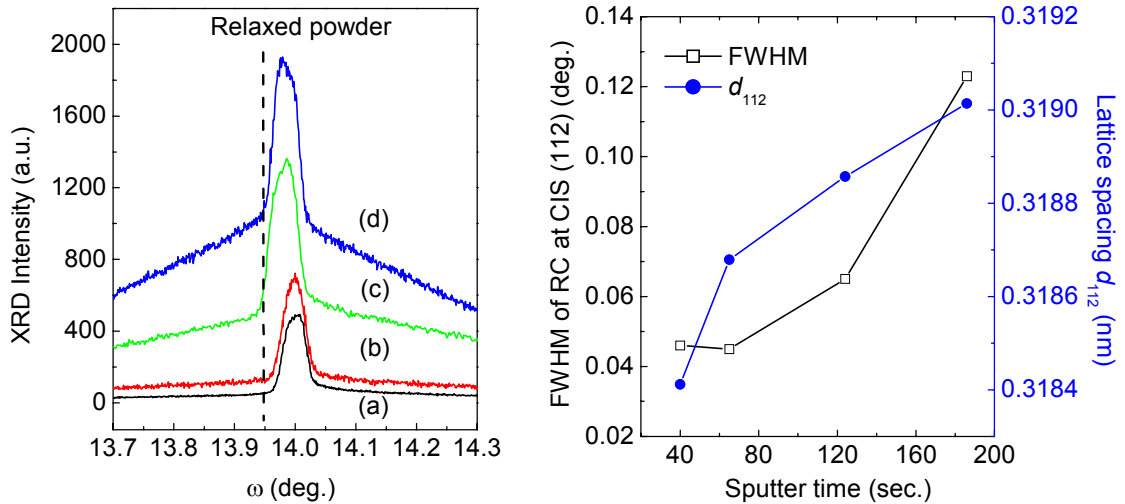

Fig. 6.2. Left: X-ray diffraction rocking curves at the (112) plane of CIS films sputtered with different times, (a) 40 sec., (b) 65 sec., (c) 124 sec., (d) 186 sec.; Right: FWHM values of curves shown in the left and lattice spacing d_{112} of the films.

The out-of-plane ordering of the sputtered films was further evaluated by rocking curve measurements. Shown in the left of Fig. 6.2 are the results of rocking curve measurements at CIS (112) of four films sputtered with different periods. The full width at half maximum (FWHM) of each curve, representative for the tilt of the crystallites in growth direction, is depicted in the right of the figure as a function of the sputter time. A FWHM value of less than 0.05° (180 arcsec), which is among the best reported values, manifests the epitaxial growth nature of the sputtered films. With an increase of the sputter time, the rocking curve becomes broader and the background intensity increases, indicating the enhancement of a mosaic structure. Compared to relaxed CIS powder, the diffraction angles and lattice spacing d_{112} of all the sputtered epilayers are larger and smaller, respectively. This indicates that the epilayers are under compressive stress along the growth direction. With increasing sputter time and thus layer thickness, the stress is gradually released and accordingly the lattice spacing d_{112} approaches the theoretical value of 0.3198 nm.

We performed XRR to measure the thickness of the thin epilayers. Fig. 6.3 plots the measured XRR spectra for the films sputtered with different times as shown in Fig. 6.2. With increasing sputter time, the angle interval between the maxima (minima) of the XRR curves decreases, showing an increase of the film thickness. In table 6.1, the simulated

thicknesses of these films are summarized along with their structural properties such as the rocking curve half width of the (112) peak and lattice spacing d_{112}.
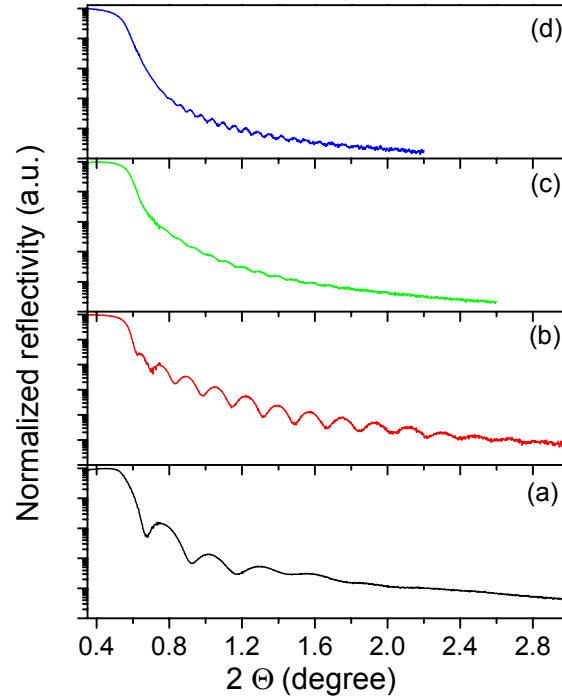

Fig. 6.3. XRR measurements of the films sputtered with different times corresponding to Fig. 6.2.

To achieve information on the in-plane ordering of the films a Siemens-Stoe AED2 four circle-diffractometer with Mo Kα (λ =0.71069 Å) radiation was applied. Curve (b) in Fig. 6.4 shows the Phi-scan spectrum recorded at CIS {204} with a tilt (Chi) angle of 35.5° for a typical film. Sharp distinct reflexes show up indicating a well-defined azimuthal alignment of the CIS lattice planes. Similar to CIS epilayers on Si (111), six peaks instead of three, as expected for single-crystalline CIS layers, are observed. Obviously two domains are coexisting in the sputtered epilayers, rotated by 180° to each other [10]. To obtain directly the in-plane orientation relationship between the CIS layer and the sapphire substrate, phi-scans with grazing incidence X-ray geometry were recorded. Under grazing incidence diffraction (GID) conditions, the incident X-ray beam is nearly parallel to the film surface, thus the reflections generated from the planes perpendicular to the surface are detected. The resultant spectra of the CIS epilayer and sapphire substrate are shown in Fig. 6.4, labeled as (a) and (c), respectively. Six peaks for both CIS and sapphire are observed. However, they are shifted by 30° to each other. It should be noted that the six peaks

displayed in GID represent the intrinsic six-fold symmetry in the CIS (112) plane, corresponding to six equivalent planes $\{2\bar{2}0\}$ (see below), two of which are exactly, the other four nearly (89.6°) perpendicular to CIS (112). In contrast, the six peaks that appeared in the tilted Phi-scan actually arise from a twinned structure of the epilayer. In the tilted Phi-scan of a single-crystalline film only a three-fold symmetry would be expected. Combining the Phi-scan and rocking curve measurements, it can thus be concluded that the sputtered CIS films grow epitaxially on the sapphire substrates with an orientation of CIS (112) sapphire (0001) and CIS $(2\bar{2}0)$ rotated by 30° with respect to sapphire $(1\bar{1}00)$.

Table 6.1. Summary of the sputter time, thickness, and structural properties of the sputtered CIS epilayers shown in Fig. 6.2.

Sample No.	Sputter time	Thickness	FWHM of rocking curve at (112)	θ	d_{112}
	(sec.)	(nm)	(arcsec)	(°)	(nm)
429-2 (a)	40	28	165.6	14.011	0.31841
427-2 (b)	65	47	162	13.999	0.31868
428-2 (c)	124	-	234	13.991	0.31886
430-2 (d)	186	119	442.8	13.984	0.31901

For heteroepitaxy the choice of the substrate is of great importance, in terms of crystal structure, lattice parameters and thermal expansion coefficients. While sapphire has a rhombohedral structure, CIS crystallizes tetragonal. It appears inconceivable to achieve epitaxial growth between these two materials. In Fig. 6.5 the projections of the CIS and sapphire unit cells on the (112) and (0001) planes, respectively, are shown. Although sapphire crystallizes in the rhombohedral structure, it can be described by a hexagonal unit cell, larger than the rhombohedral one [21]. The similarity of the hexagonal feature of both unit cells in the depicted projections reveals the possibility for heteroepitaxy. One finds two concentric hexagons in the (0001)-projected sapphire cell, when considering Al atoms only, and also two concentric hexagons in the CIS (112) projection. In both cases the bigger hexagon is rotated by 30° with respect to the smaller one. The side length of the bigger hexagon in the sapphire (0001) plane is 0.47587 nm, and 0.39222 nm in the CIS (112) plane, corresponding to a mismatch of approximately 17.6 %. However, the mismatch reduces to 1.1% if one considers a group of five sapphire and six CIS hexagons.

Similarly, the misfit along the growth direction between four (112) spacings of CIS and the sapphire lattice parameter c is only 1.55%. The similar in-plane hexagonal symmetry, well-matched lattice spacing, as well as comparable thermal expansion coefficients (α_c of CIS [22] and sapphire is 9.6 and 4.75×10^{-6} K^{-1}, respectively) enable the heteroepitaxial growth of CIS on sapphire as demonstrated in the present study.
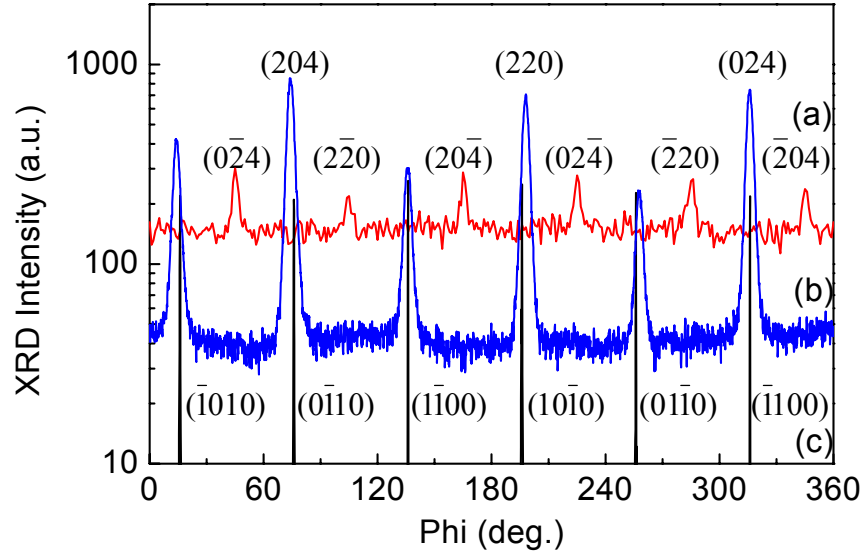

Fig. 6.4. In-plane Phi-scans of film (c) in Fig. 6.2 and sapphire substrate. (a) Recorded at CIS $\{2\bar{2}0\}$ with a grazing incidence angle of 1°; (b) recorded at CIS $\{204\}$ with a tilt angle (Chi) of 35.5°; (c) recorded at sapphire $\{10\bar{1}0\}$ with a grazing incidence angle of 1°.

Table 6.2. List of nine planes of CuInS$_2$ having nearly identical lattice spacing.

h	k	l	a (nm)	c (nm)	d_{hkl}(nm)	2θ (°)
0	2	4	0.5523	1.1141	0.19610	46.298
2	0	4	0.5523	1.1141	0.19610	46.298
2	2	0	0.5523	1.1141	0.19527	46.507
0	-2	4	0.5523	1.1141	0.19610	46.298
-2	0	4	0.5523	1.1141	0.19610	46.298
2	-2	0	0.5523	1.1141	0.19527	46.507
0	2	-4	0.5523	1.1141	0.19610	46.298
2	0	-4	0.5523	1.1141	0.19610	46.298
-2	2	0	0.5523	1.1141	0.19527	46.507

Due to the fact of c/a ≈ 2 of the $CuInS_2$ unit cell, the following conversions between the cubic and the tetragonal chalcopyrite notations are valid: $[uvw]_{cubic}$ = $[2u2vw]_{ch.}$, $(hkl)_{cubic}$ = $(hk2l)_{ch.}$. Like six equivalent lattice planes {101}: (101), (011), (110), (10$\bar{1}$), (1$\bar{1}$0), and (01$\bar{1}$), with the same lattice spacing in a cubic structure, nine planes in tetragonal chalcopyrite CIS have nearly identical lattice spacing, and thus corresponding 2θ values of XRD. The lattice spacing d_{hkl} for a plane (hkl) of tetragonal structure can be calculated by the formula,

$$\frac{1}{d_{hkl}^2} = \frac{h^2 + k^2}{a^2} + \frac{l^2}{c^2} , \tag{6.1}$$

where a, c are the lattice parameters. Using the standard lattice parameters of powder $CuInS_2$, a: 0.5523 nm and c: 1.1141 nm, we calculated and found theoretically nine planes with nearly identical lattice spacing in $CuInS_2$ as listed in table 6.2. These nine planes can be further divided into two groups, i.e., three equivalent planes {204}: (204), (024), (220), and six equivalent planes {2$\bar{2}$0}: (02$\bar{4}$), (20$\bar{4}$), (2$\bar{2}$0), (0$\bar{2}$4), ($\bar{2}$04), ($\bar{2}$20), in terms of lattice spacing and their inclination angles with plane (112). The angle ϕ between $(h_1k_1l_1)$ and $(h_2k_2l_2)$ planes of the tetragonal system can be generally derived from

$$\cos\phi = \frac{(h_1h_2 + k_1k_2)/a^2 + l_1l_2/c^2}{\sqrt{(h_1^2 + k_1^2)/a^2 + l_1^2/c^2} \sqrt{(h_2^2 + k_2^2)/a^2 + l_2^2/c^2}} , \tag{6.2}$$

where a, c are the lattice parameters. With still the standard a, c values of powder $CuInS_2$, we found that six planes {2$\bar{2}$0} are exactly or nearly perpendicular to CIS (112), whereas three planes {204} incline by approximately 35.5° from the CIS (112), as listed in table 6.3.
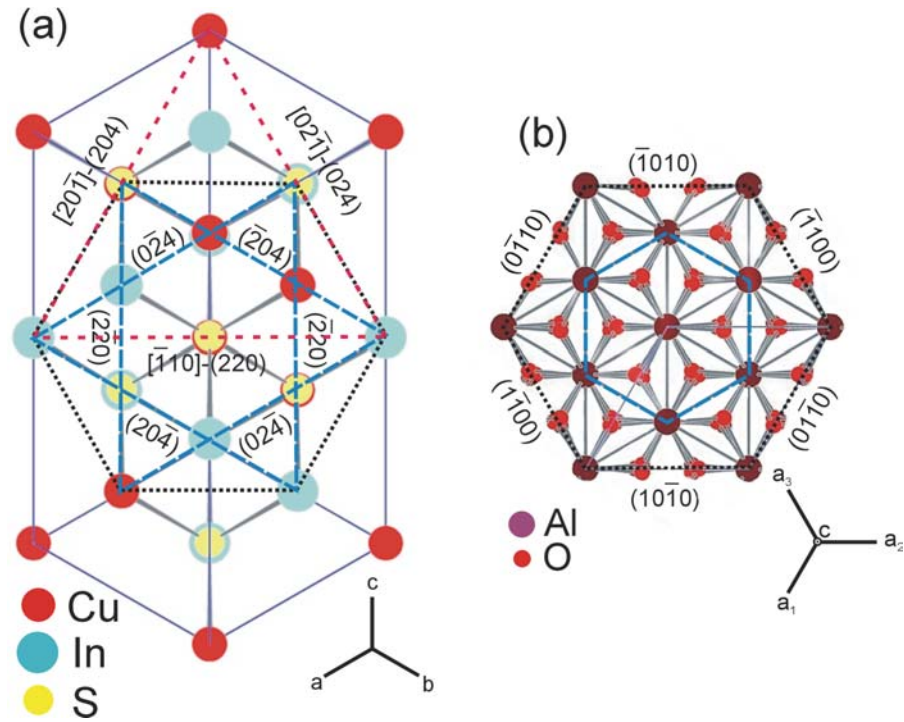
Fig. 6.5. Projections of (a) CIS to the (112) plane and (b) sapphire to (0001), illustrating the orientation relationship between the epilayer and substrate as revealed by XRD measurements. The planes $\{2\bar{2}0\}$ of CIS and $\{10\bar{1}0\}$ of sapphire, being perpendicular to the projection planes, are identified. For CIS, three equivalent planes $\{204\}$ that tilt by 35.5° from the (112) plane are marked by their common sides with (112), e.g., "$[20\bar{1}]$-(204)" means the common side of the planes (204) and (112) along the crystal line $[20\bar{1}]$.

Table 6.3. List of three equivalent planes $\{204\}$: (204), (024), (220), and six equivalent planes $\{2\bar{2}0\}$: $(02\bar{4})$, $(20\bar{4})$, $(2\bar{2}0)$, $(0\bar{2}4)$, $(\bar{2}04)$, $(\bar{2}20)$ of CuInS$_2$.

h_1	k_1	l_1	h_2	k_2	l_2	a (nm)	c (nm)	cos(ϕ)	ϕ (°)
0	2	4	1	1	2	0.5523	1.1141	0.81533	35.380
2	0	4	1	1	2	0.5523	1.1141	0.81533	35.380
2	2	0	1	1	2	0.5523	1.1141	0.81882	35.033
0	-2	4	1	1	2	0.5523	1.1141	-0.00698	90.400
-2	0	4	1	1	2	0.5523	1.1141	-0.00698	90.400
2	-2	0	1	1	2	0.5523	1.1141	0	90
0	2	-4	1	1	2	0.5523	1.1141	0.00698	89.600
2	0	-4	1	1	2	0.5523	1.1141	0.00698	89.600
-2	2	0	1	1	2	0.5523	1.1141	0	90

As illustrated in Fig. 6.5 (a), the inner smaller hexagon of the CIS lattice projection on the (112) plane is composed of six equivalent planes $\{2\bar{2}0\}$, perpendicular to (112). Three planes $\{204\}$ that tilt by about 35.5° from (112) are figured out by their lines of intersection with (112). Whereas the lines of intersection of the $\{204\}$ and (112) planes are parallel to three sides of the outer (bigger) hexagon, the inner hexagon is rotated by 30° with respect to the outer one, which is corresponding to the outer (bigger) hexagon in the sapphire (0001) projection. This illustrates clearly the orientation relationship as determined by XRD measurements.

Atomic force microscopy was used to further characterize the structural properties of the sputtered CIS epilayers. In Fig. 6.6 the AFM images (top view and three-dimensional) of a typical thin epilayer are displayed, which represent the surface morphology as well as microstructure of the sputtered films. The film had a very smooth surface with a root-mean-square (RMS) roughness of approximately 3.3 nm. Typical for thin films grown by sputter epitaxy, the sputtered CIS epilayers displayed granular surface structure [20, 23], suggesting a three-dimensional island-like growth mechanism.
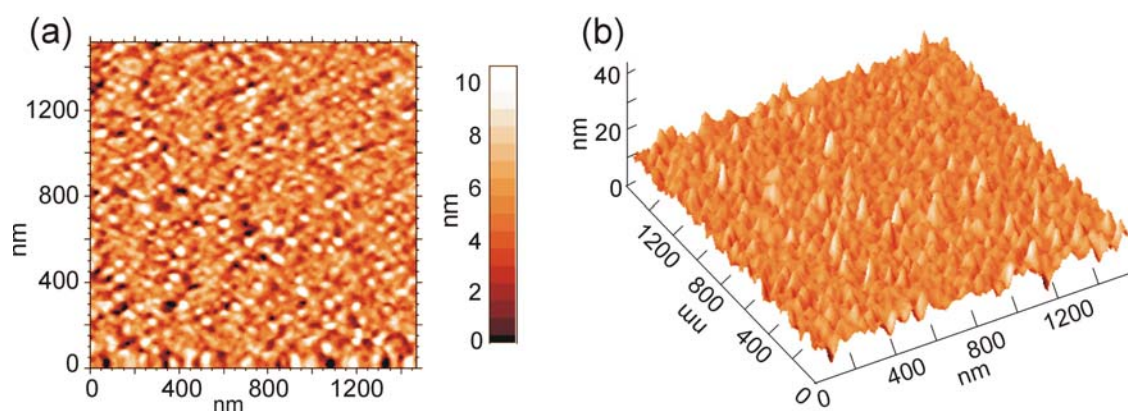
Fig. 6.6. AFM images of a typically sputtered CIS film on sapphire. (a) Top view; (b) three-dimensional view.

In conclusion, CuInS$_2$ films were grown epitaxially on single-crystalline sapphire substrates by RF reactive sputter epitaxy. Both rocking curve and Phi-scan of X-ray diffraction measurements reveal well-defined out-of-plane and in-plane lattice ordering, confirming the heteroepitaxial growth with the orientation relationship of CIS (112) sapphire (0001), CIS $[\bar{1}10]$ sapphire $(10\bar{1}0)$. AFM demonstrates a smooth surface of the resultant films and suggests a three-dimensional island-like growth mechanism. The success of epitaxial growth of CIS on sapphire indicates that heteroepitaxy may not only

occur in material systems with similar structural symmetry, e.g., cubic on cubic, tetragonal on cubic, or vice versa, but is also possible for materials with different symmetry, e.g., cubic on hexagonal, tetragonal on hexagonal, or vice versa, if a suitable growth direction is chosen [24].

6.2   Quasi-epitaxial growth of thick CuInS$_2$ films

Although very thin CIS films (25-100 nm thick) can be grown epitaxially on sapphire with a well-defined out-of-plane and in-plane ordering by RF reactive sputtering, it was found that upon increase of the sputter time and thus the thickness the films were characterized by pronounced mosaic structures, as will be described below. In an incidental way, we found that pre-sputtering an ultrathin CIS epilayer as a buffer (nucleation layer) could substantially depress the mosaic structure and consequently improve the out-of-plane ordering of the sputtered films. However, the in-plane alignment of the films becomes more complex with such an ultrathin buffer. In this section, we first present the structural characteristics of the directly sputtered thick CIS films on sapphire. Then, we concentrate on elucidation of the structural features of the CIS films sputtered with an ultrathin buffer layer by detailed X-ray diffraction investigation.

6.2.1   Structural characteristics of the thick CuInS$_2$ films sputtered directly on sapphire
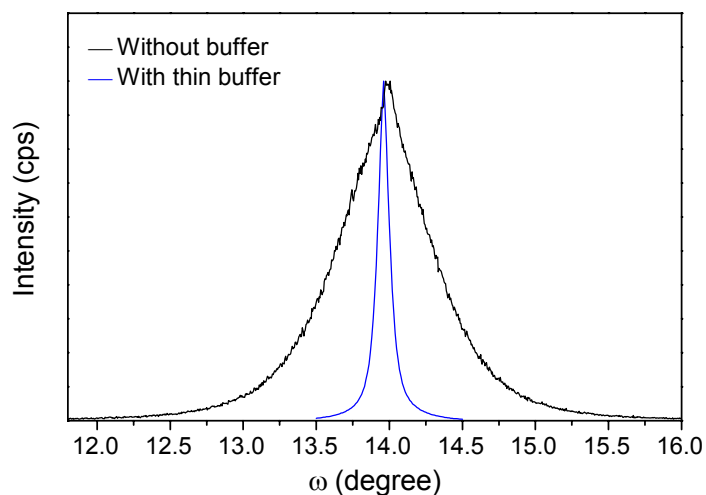
Fig. 6.7. Comparison of XRD rocking curves of (112) of thick CIS films sputtered directly on sapphire (black curve) and sputtered with an ultrathin buffer layer (blue curve).

Whereas the θ-2θ scan showed a similar preferred (112) orientation of the thick films with that of the thin epilayers, i.e., only (112), (224), and (336) peaks of CIS were detected, X-ray rocking curve measurements revealed a remarkable mosaic feature of the thick CIS

films sputtered directly on sapphire. Fig. 6.7 (black curve) shows the rocking curve of CIS (112) recorded for a typical film sputtered at 500°C and 200 W for 30 min with a thickness of approximately 1000 nm. Compared to the sputtered thin epilayer, the out-of-plane ordering of the thick films has drastically degraded. Whereas a 70-nm epilayer, sputtered in 2 min, has typically a rocking curve FWHM at CIS (112) of about 0.05° (180 arcsec), the rocking curve half width of the 30-min-sputtered film, approximately 1000 nm thick, is about 0.68° (2448 arcsec), indicating a pronounced mosaic structure.
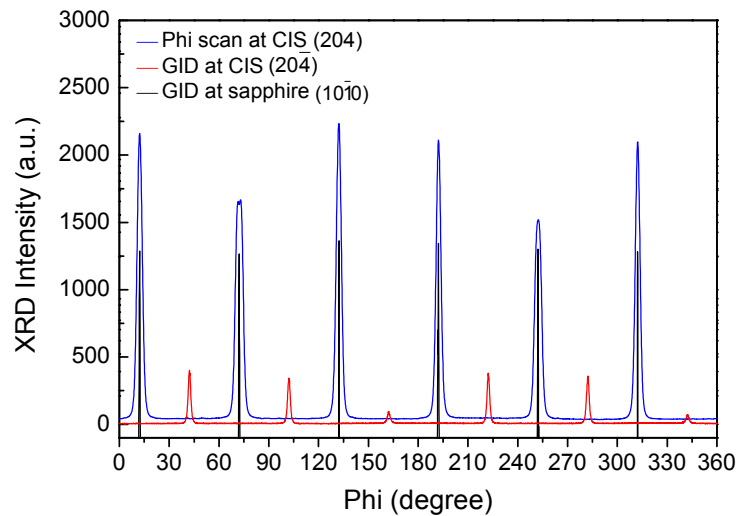
Fig. 6.8. Phi-scans of a thick CIS film and sapphire substrate, recorded at CIS {204} with a tilt angle (Chi) of 35.5° (blue curve), at CIS {20$\bar{4}$} with a grazing incidence angle of 1° (red curve), and at sapphire {10$\bar{1}$0} with a grazing incidence angle of 1° (black curve), respectively.

The in-plane alignment of the thick films remains, however, comparable with that of the thin epilayers. Fig. 6.8 displays the Phi scan spectra of the same film as in Fig. 6.7, recorded at {204} with a tilt angle (Chi) of 35.5° and at {20$\bar{4}$} with a grazing incidence angle of 1.0°, along with the grazing incidence Phi scan spectrum of sapphire (10$\bar{1}$0). Both tilted Phi scan and GID Phi scan show six sharp peaks, demonstrating well-ordered alignment of the sputtered thick films in the (112) plane. Like in the thin epilayer, while the six peaks shown in GID represent an intrinsic six-fold symmetry of CIS film in the (112) plane, the six peaks in the tilted Phi scan suggest a twinned structure, i.e., two domains rotated by 180° along [221], coexist in the films. Identification of the peaks shown in Fig. 6.8 can be accomplished according to Fig. 6.4.

Consistent with the pronounced mosaic structure revealed by XRD, a macroscopic rough surface is observed for the directly sputtered thick films. In Fig. 6.9 SEM

micrographs imaged at the surface (a) and cross section (b) of the same sample discussed above are depicted. Uniformly distributed grains are clearly seen, disclosing the polycrystalline nature of the sputtered thick films. In combination with the XRD results of both rocking curve and Phi scan measurements, it can be concluded that the thick CIS films sputtered directly on sapphire are highly (112)-textured polycrystalline films.
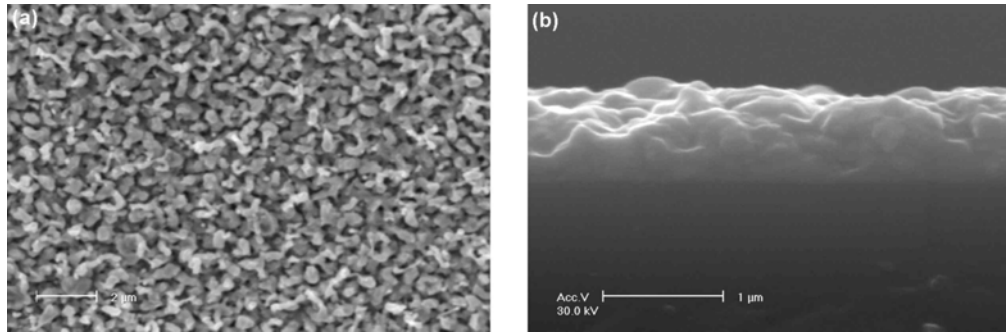

Fig. 6.9. SEM micrographs imaged at (a) the surface and (b) cross section of the thick CIS film sputtered directly on sapphire as shown in Fig. 6.8.

6.2.2 Quasi-epitaxial growth of thick $CuInS_2$ films on an ultrathin buffer-layer
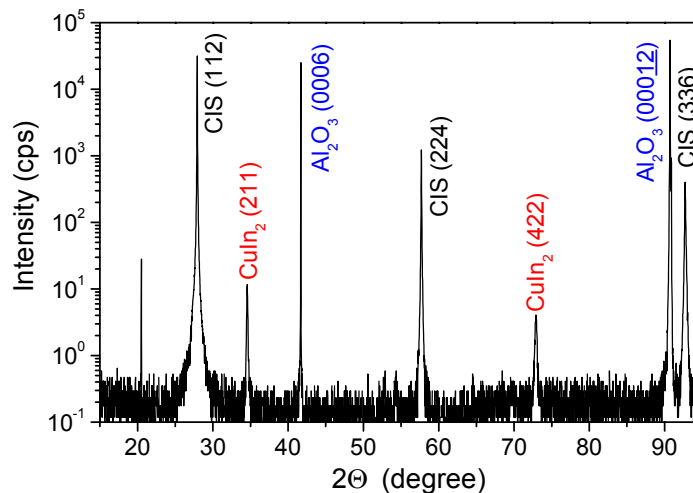
Fig. 6.10. XRD spectrum of a typical CIS thick film sputtered on an ultrathin buffer layer.

We first sputtered an ultrathin CIS epilayer on single-crystalline (0001) sapphire, using the same parameters described in the preceding section, i.e., at 500°C and 200 W with H_2S flow in the range of 30-35 sccm. The thin epilayers were typically sputtered for 1 min with a thickness of approximately 35 nm. Then, the epilayer was cooled down in situ in the sputter chamber till room temperature with duration of roughly 4 h. Subsequently, the thin epilayer along with the substrate was heated again up to 500°C, and we sputtered a thick layer with the same parameters on top of the pre-sputtered ultrathin layer.

Fig. 6.10 exhibits the θ-2θ scan spectrum of a sputtered thick film on an ultrathin buffer- layer. The spectrum shows only sharp reflections from (112), (224), (336) planes of CIS, demonstrating an orientation of the film with respect to the substrate of CIS (112) sapphire (0001). In addition, diffraction peaks corresponding to $CuIn_2$ (211) and (422) planes are present, which could arise from the In-rich composition of the sputter target.
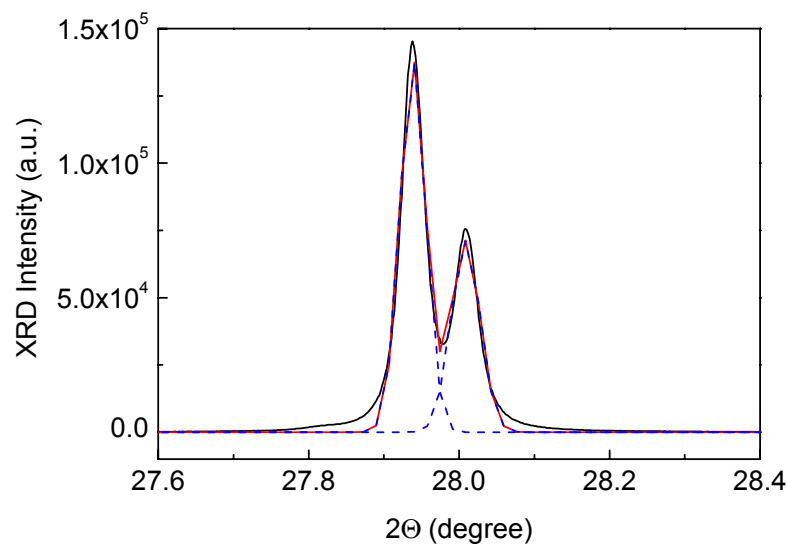

Fig. 6.11. Narrow-scan θ-2θ spectrum recorded near CIS (112) of the doublelayer film corresponding to Fig. 6.10.

Narrow-scan θ-2θ spectrum was recorded near $CuInS_2$ (112) on the same sample, as plotted in Fig. 6. 11. A well-resolved double-peak structure, i.e., two peaks corresponding to Cu $K_{\alpha1}$ and $K_{\alpha2}$ lines of X-ray source, reflects the highly ordered nature of these films. A Gaussian fitting yields two peaks, centered at 27.94 and 28.01, respectively, with a half width of approximately 0.035°.
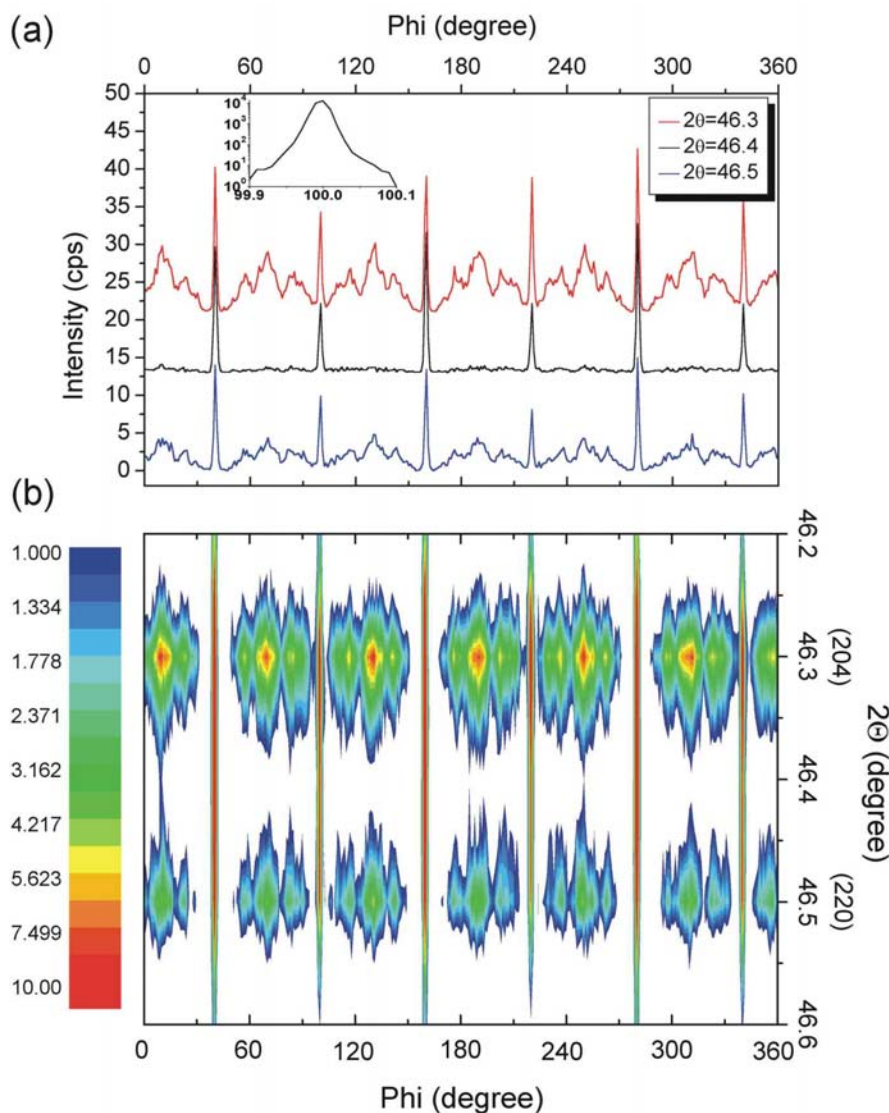
Fig. 6.12. (a) Phi-scans with a tilt angle (Chi) of 35.5° at specific 2θ of 46.3°, 46.4°, and 46.5°, (b) Phi-2θ map with a fixed Chi of 35.5°, recorded on the same sample as shown as Fig. 6.10.

As demonstrated in Fig. 6.7 (blue curve), the half width of the rocking curve at (112) of the thick film grown with a pre-sputtered thin buffer is much smaller than that of the film sputtered directly on the sapphire. Upon pre-sputtering of the ultrathin buffer-layer, the FWHM of rocking curve of CIS (112) was reduced from approximately 0.68° to 0.1° (360 arcsec), indicating a great improvement of the out-of-plane ordering of the sputtered films. While Metzner *et al.* reported a rocking curve half width of (224) of 0.2° (720 arcsec) for MBE grown films on sulphur-terminated Si (111) [8], Hunger *et al.* achieved CIS epilayers on hydrogen terminated Si (111) by the same technique with a rocking curve half width of (112) of 550 arcsec [10]. The 360-arcsec half width of our sputtered thick films thus manifests, that the perfection of the out-of-plane ordering of our sputtered films is even superior to that of epitaxial CIS layers grown on Si (111) by MBE.
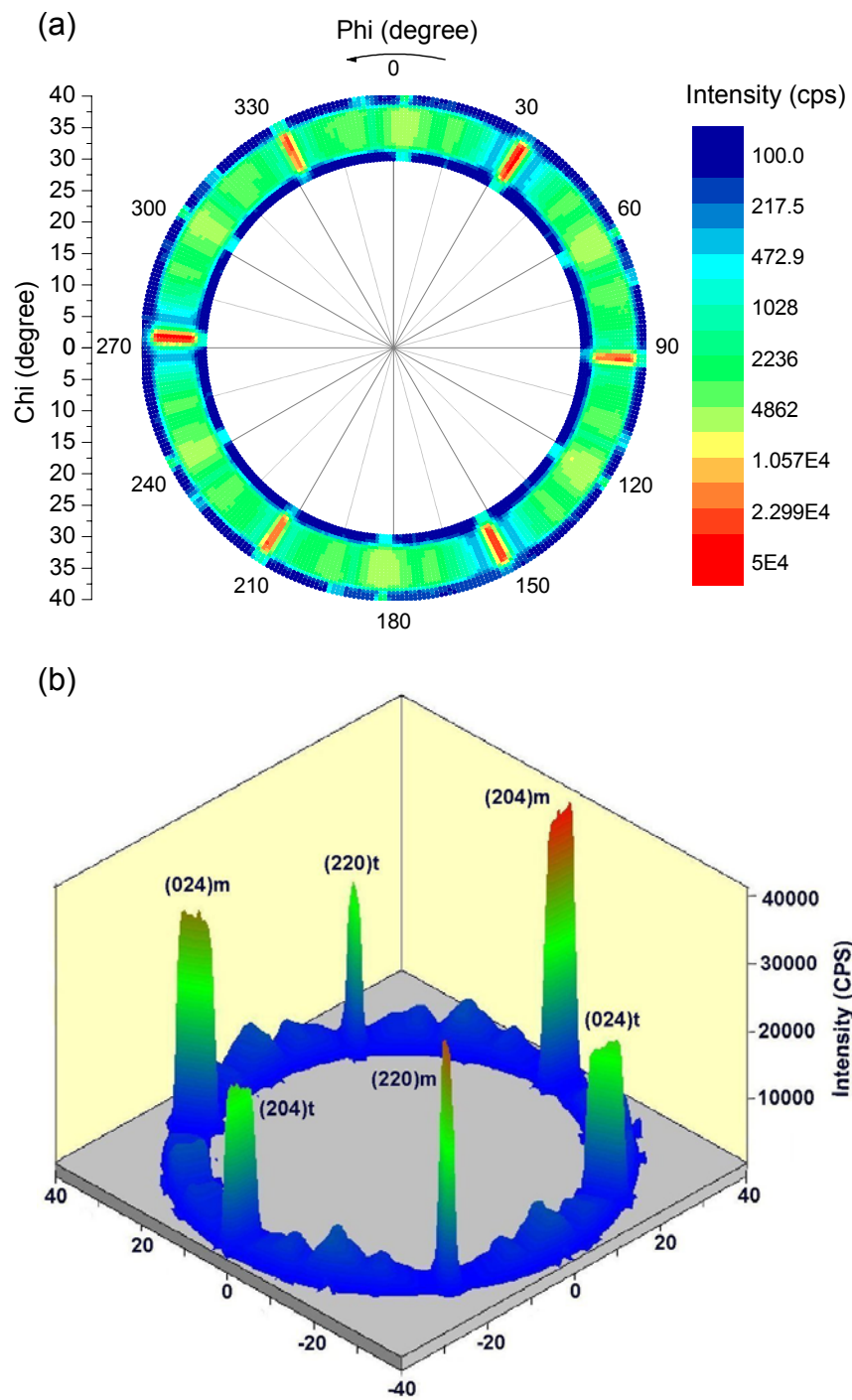
Fig. 6.13. Polefigure texture analysis of the typically sputtered doublelayer film shown in Fig. 6.10. (a) Two-dimensional, and (b) three-dimensional Phi-Chi maps at CIS {204}.

The pre-sputtered ultrathin buffer-layer, on the one hand, promotes greatly the out-of-plane ordering, on the other hand, makes the in-plane alignment more complicated. In Fig. 6.12 the 2θ-Phi map recorded on a typically sputtered thick layer is illustrated. While

graph (b) shows the whole range map of 2θ: 46.2°-46.6° and Phi: 0°-360°, graph (a) displays only the chosen Phi scans at specific 2θ of 46.3° and 46.5°, corresponding to CIS (204) and (220), respectively, and at a 2θ inbetween them (46.4°). From the Phi scans shown in graph (a), one can see the sixfold symmetry of the major peaks, as observed in the sputtered thin epilayers and highly (112)-textured thick films sputtered without a thin buffer. In between the major peaks, there are additional regular modulations present, indicating a multi-domain structure of the thick films rather than a two-domain structure as in the sputtered thin epilayers. Inserted in graph (a) is the Phi scan at sapphire $(10\bar{1}0)$, revealing an in-plane orientation relationship of CIS $[\bar{1}10]$ sapphire $(10\bar{1}0)$ between the main domain of sputtered CIS layers and sapphire substrates. The separation of reflections from (204) and (220) planes, corresponding to the well-separated two sets of modulations at 2θ of 46.3° and 46.5°, respectively, seen in (b), determines conclusively the tetragonal chalcopyrite rather than zincblende structure of the sputtered films.

For a better understanding of the complex multi-domain structure of the sputtered thick films, a polefigure texture analysis (Phi-Chi map) was implemented on the same sample. Fig. 6.13 illustrates the two-dimensional (a) and three-dimensional (b) Phi-Chi maps recorded at CIS (204) (2θ: 46.3°). Again, we see sixfold symmetry of the major peaks, as occurred in the Phi-2θ map. We have discussed in the former section, that for a perfect single-crystalline CIS film, threefold instead of sixfold symmetry is expected. The six major peaks present in the maps can actually be grouped into two sets according to their intensities and shapes (widths), each set consisting of three peaks with equal azimuthal separation of approximately 120°, as indicated in graph (b). While $(204)_m$, $(024)_m$, and $(220)_m$ represent the three equivalent planes {204} of the main domain, $(204)_t$, $(024)_t$, and $(220)_t$ denote three equivalent planes of the twinned domain. Clearly, the twinned domain is rotated by 180° with respect to the main domain, and its volume is approximately half of the main domain, providing the volume of each domain is proportional to its XRD intensity. Our observation is in good agreement with that reported by Hunger *et al*. for their MBE grown CIS epilayers on hydrogen terminated Si (111) [10]. In addition to the 180° twin, other domains with different orientations exist in the films, as reflected by the complex but regular modulations in between the major peaks. However, their intensities are much lower than those of the major peaks, as will be discussed in detail below.
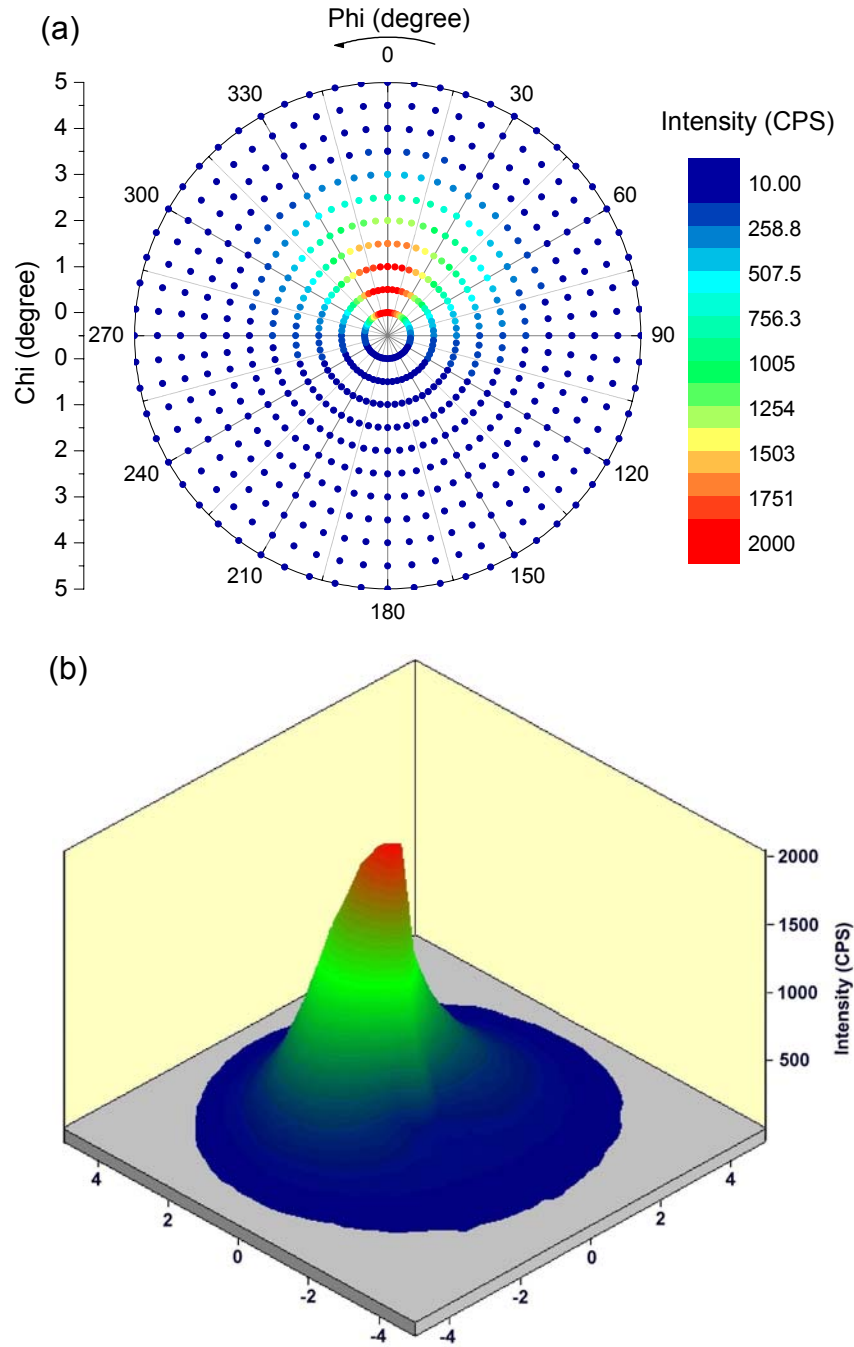
Fig. 6.14. Polefigure analysis: (a) two-dimensional and (b) three-dimensional Phi-Chi maps at CIS (112) of the typical doublelayer film in Fig. 6.10.

For the $CuGaS_2$ epilayers on Si (111) grown by MBE, it was found that epitaxial growth took place in three equivalent c-axis orientations, i.e., epitaxial relation $[221]_{CGS}$ $[111]_{Si}$ violated weakly with an angle between them of approximately 0.8° [25]. To inspect whether it is also the case for our sputtered thick $CuInS_2$ films on sapphire, we performed polefigure analysis at CIS (112) and (224) on our films. Shown in Fig. 6.14 are the two-dimensional (a) and three-dimensional (b) Phi-Chi maps at (112) of the typical film corresponding to Fig. 6.13. Only one peak is observed, though nonsymmetric (see

(a)), indicating an exclusive direction growth occurred during the sputter process. This confirms again the nearly perfect out-of-plane ordering of our sputtered films along the growth direction.
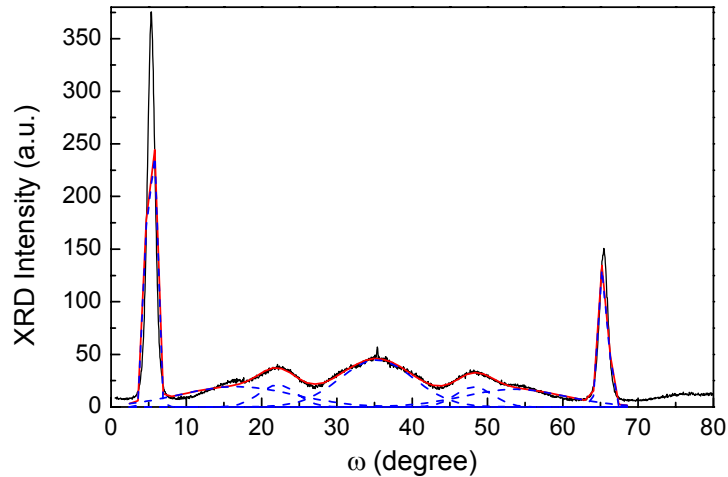

Fig. 6.15. Grazing incidence ω scan at CIS $\{20\bar{4}\}$ (2θ: 46.3°) of the same doublelayer film as in Fig. 6.10.

To achieve more information directly on the in-plane alignment of the thick films sputtered with the ultrathin buffer-layer, omega (ω) scans with grazing incidence geometry were carried out. Fig. 6.15 shows the GID ω scan at CIS $\{20\bar{4}\}$ (2θ: 46.3°) of a typical film in the range of 0°-80°. Between two major peaks, a modulation with fivefold symmetry is observed. Gaussian fitting gives seven peaks. The modulation is symmetric along the peak centered near 35.3°, as can be judged in terms of the peak center, width, and height. It thus suggests, in addition to the main domain and 180° twin, multi domains that shifted by approximately 11°, 17°, 30°, 43°, and 49° from the main domain in the (112) plane are coexisting in the thick double-layer systems. However, their volumes are smaller than that of the main domain by more than a factor of 10, as indicated by their XRD intensities with respect to the major peak.

The pre-sputtering of an ultrathin buffer-layer enhances significantly the top thick layer quality in terms of the out-of-plane ordering, and improves also the film surface morphology. In contrast to the surface of the thick films sputtered without a buffer, which is macroscopically rough, the films with an underlying buffer possess a mirror-like smooth surface. However, SEM reveals that even applying the thin buffer the surface of the thick films is still rough on a microscopic scale. Fig. 6.16 depicts the SEM micrographs imaged

at the surface and cross section of the typical film discussed above. A surface typical for sputtered films with holes and damages caused by the re-sputtering of the film is observed. Nevertheless, cross section image reflects a well-grown structure of the film in the bulk, which is much superior to that of the film sputtered without the thin buffer.

The improvement of the film quality via pre-sputtering of an ultrathin buffer could be attributed to the nearly perfect epitaxial growth nature of the ultrathin layer. The thin epilayer certainly offers better nucleation conditions for the subsequent sputtering of the thick top layer. Although the thin CIS epilayer is more or less under stress, its lattice constants are very close to those of bulk CIS crystals, leading to a better lattice match between the top CIS thick layer and the underneath sapphire substrate.
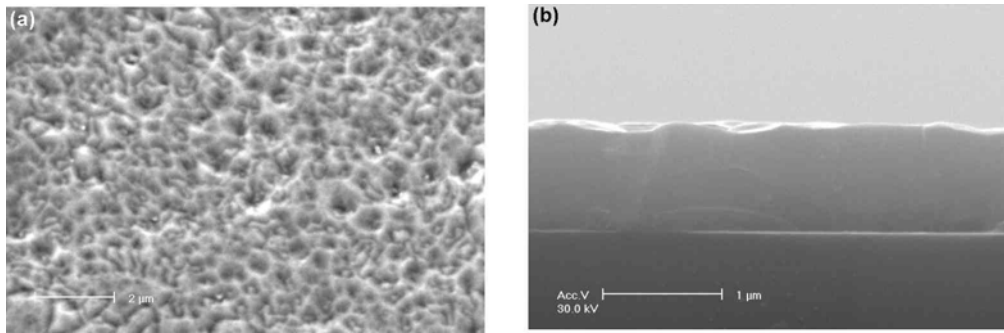

Fig. 6.16. SEM micrographs imaged at (a) the surface and (b) cross section of the typically sputtered doublelayer film as shown in Fig. 6.10.

In conclusion, we realized the quasi-epitaxial growth of thick $CuInS_2$ films on (0001)-sapphire substrates with pre-sputtering an ultrathin buffer-layer. The rocking curve half width of such a double-layer system is approximately 0.1° (360 arcsec), manifesting a nearly perfect ordering of the films along the growth direction. XRD polefigure analysis revealed, however, an in-plane multi-domain feature of the double-layer systems. In addition to a primary twin that rotated by 180° with respect to the matrix along [221], other domains with different orientations and much lower volumes coexist in the films.

6.3   Transmission electron microscopy characterization on quasi-epitaxially grown $CuInS_2$ films

In addition to XRD, AFM, and SEM, TEM was used to evaluate the structural properties of the sputtered quasi-epitaxially grown CIS films on sapphire. While XRD determines macroscopically the crystal structure, orientation as well as grain size of the films, and AFM and TEM characterize the film surface structure and morphology, TEM offers a deeper insight into the internal microstructure, especially the defect structure of the films.

For both the thin epilayers and thick quasi-epitaxial films sputtered with a thin buffer, TEM revealed a highly ordered structure, in accordance with the XRD results. Fig. 6.17 (a) displays a high resolution TEM (HRTEM) cross section image recorded at the interface region of a typical thick film sputtered with an underlying buffer. Long range lattice ordering is observed. A selected area image of the same sample is depicted in (b), where the nearly perfectly grown lattice, free of defects is well resolved. However, similar to the CIS epilayers grown on Si by MBE [26], the sputtering deposited quasi-epitaxial layers on sapphire are generally defective, with a defect density in the order of 10^{11} cm^{-2}. The dominant defects are stacking faults, dislocations, point defects like vacancies, and twins with different orientations, as revealed by XRD. Fig. 6.17 (c) shows a HRTEM image of a sputtered thin CIS epilayer. Very interestingly, while one sub-lattice shows clearly local ordering, in some of the columns in the other sub-lattice atoms are missing, indicated by arrows in the picture, demonstrating directly the vacancies included in the sputtered films. In addition, some evidence was observed for the formation of an interfacial layer with a thickness of a few angstroms between the sputtered CIS films and the sapphire substrates. An example is illustrated in picture (a), as indicated by arrows.

TEM characterizations on the sputtered quasi-epitaxially grown CIS films imply, that there are still plenty of spaces to further improve the crystalline quality of the films. For instance, reducing the RF power during sputtering could promote the epitaxial growth, since with a lower velocity the ejected atoms from the target have more time to move to and seat where they should be and get relaxed there. A modified off-axis sputtering technique, i.e., instead of being fixed along the same axis face to face, the sputter target and the substrate incline with each other by some angle, e.g. 90°, can significantly reduce the re-sputtering of the film surface, thus may lead to enhancement of the film morphology as well as reduction of the defects within the bulk of the films. Moreover, the common

technique used for epitaxial growth, i.e., preconditioning of the substrates via heating and /or chemical or sputter etching, which was omitted in our sputter process, may be introduced to further improve the film quality.
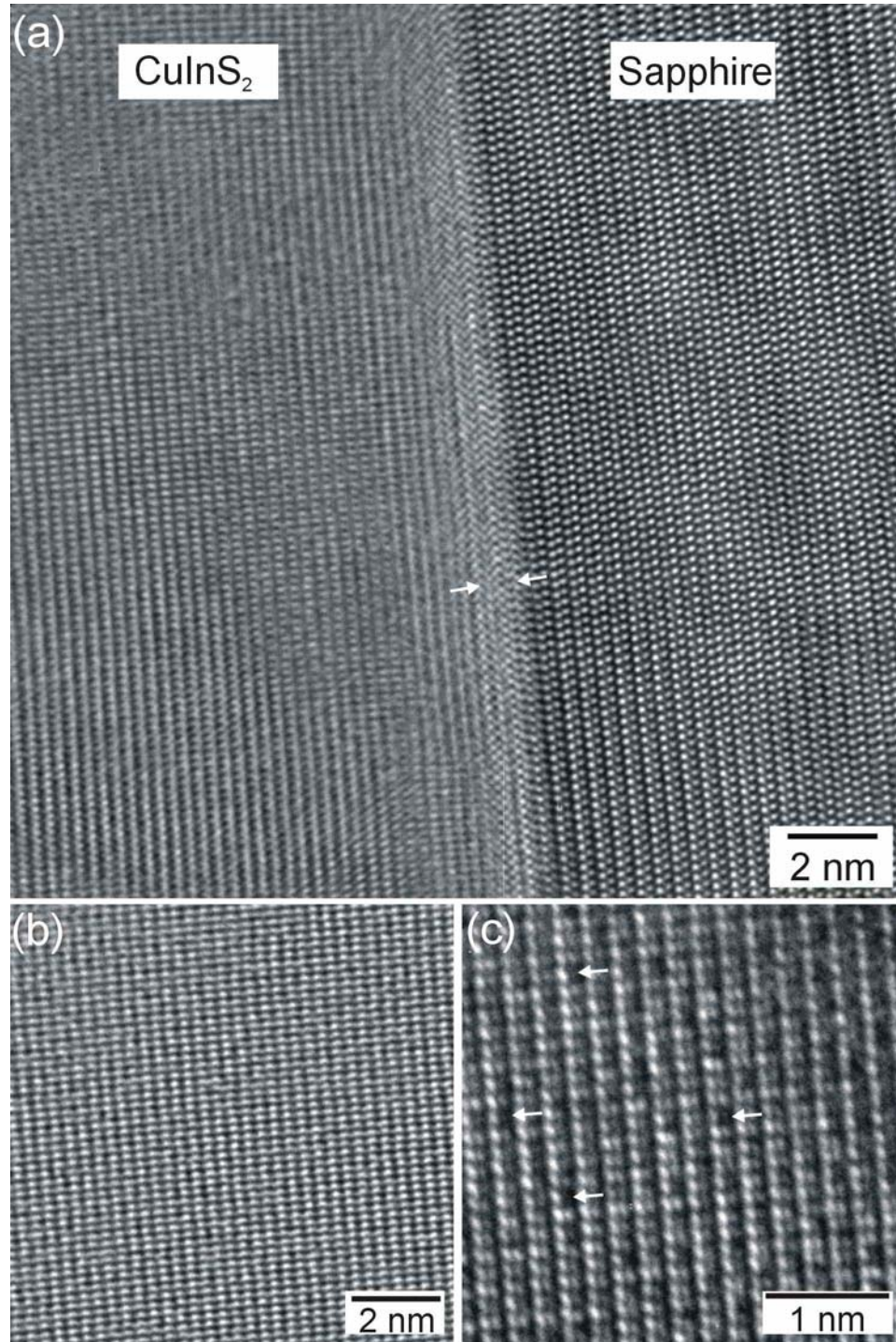

Fig. 6. 17. (a) Cross section HRTEM image recorded at the interface region of a typical thick CIS film sputtered with a thin buffer, arrows indicate the interfacial layer between the CIS film and the substrate; (b) selected area image of the same sample as in (a); (c) HRTEM image of a typically sputtered thin epilayer, arrows indicate the missing of atoms, i.e., vacancies in the film.

7   Summary and outlook

Although various techniques have been performed to produce $CuInS_2$ films, the efficiencies of solar cells based on $CuInS_2$ films have been limited to around 12 % to date, primarily due to the relatively low quality of the $CuInS_2$ absorber layers and insufficient knowledge about the fundamental properties of the absorber material. In principle, sputtering has the advantage of easy control of the film stoichiometry over a large scale at relatively low cost. It has already been utilized in industry for the production of a wide range of functional materials. Therefore, in this study, we have chosen the RF reactive sputtering technique to deposit $CuInS_2$ thin films, and characterized the sputtered films in terms of structural, optical, and electrical properties, to optimize and establish a reactive sputter process suitable for the production of $CuInS_2$ films for photovoltaic applications. This work comprises primarily two aspects: the one-stage growth process and the characterization of $CuInS_2$ films deposited on float glass substrates, and quasi-epitaxial growth of $CuInS_2$ films on single-crystalline sapphire by RF reactive sputtering.

One-stage sputtering of $CuInS_2$ films on float glass

Using a Cu-In alloy target and introducing solely H_2S as both working and reactive gas during sputtering, we achieved deposition of CIS films in one step. The main work and results concerning this aspect are summarized as follows:

- To optimize the sputtering process, we first investigated systematically the influence of sputter parameters, such as H_2S flow rate, substrate temperature, and sputter power, etc., on the film properties. There are mainly secondary Cu-In phases coexisting in the films when the H_2S flow rate is insufficient during sputtering, however, excessively injected H_2S causes a minor phase of elemental S in the sputtered films. With a RF power of 200 W and a H_2S flow in the range of 20-29 sccm, $1.93\text{-}2.93\times10^{-1}$ Pa in partial pressure, highly (112)-oriented films with good quality and very good adhesion can be sputtered on bare float glass at a substrate temperature of 400°C or above. A higher H_2S flow rate is required to avoid Cu-In alloy phases in the sputtered films when increasing the substrate temperature or sputter power. Raising the substrate temperature from 400 to 500°C leads to an improvement of the structural properties of the films, increasing the grain size from approximately 95 nm to 145 nm, and subsequently enhances the optical properties, shifting the bandgap from approximately 1.27 to 1.44 eV. With a pre-sputtered Mo- or ZnO-coating $CuInS_2$ films can be sputtered at a relatively low temperature of 200°C. In addition, the Mo-, or ZnO-

87

coating works effectively as a barrier to prevent Na diffusion from the float glass substrates into the CIS layers.

- Surface and structural properties of the one-stage sputtered $CuInS_2$ films were characterized in detail by means of AFM, SEM, EDX, GIXRD, XRR, XPS, UPS, and SIMS. The sputtered CIS films are in general oriented preferentially with CIS (112) parallel to the substrate surface, as revealed by XRD and GIXRD. XRR measurement determined a film surface density around 5.01 g/cm^3, higher than the theoretical value for pure CIS, indicating a secondary phase existing on the film surface. Additionally, by XRR the deposition rate of the one-stage sputter process was determined to be approximately 33 nm/min. Both AFM and SEM revealed a rough surface of the sputtered films, where incoherent segregations were clearly observed. SEM and EDX were used to identify the segregation on the film surfaces, which showed that the Cu/In ratio in the surface precipitates deviated extremely from that in the CIS matrix. Despite of the Cu_xS surface segregation, XPS revealed that the film surfaces remain In-rich with respect to the bulk, and the surface properties are dominated by oxidation after exposure to air. SIMS manifested a good depth homogeneity of all the films sputtered on bare, Mo- or ZnO-coated glass substrates.

- Although stoichiometric pure $CuInS_2$ phase films can be produced in one step by RF reactive sputtering, post-deposition treatments affect significantly the structual, optical and electrical properties of the sputterd films. Heating under vacuum at a temperature of 500°C for 2 hours caused recrystallization of the as-sputtered films and consequently improved the film optical properties. Annealing in a H_2S atmosphere at 500°C for suitable duration resulted in the elimination of the secondary Cu-In phases coexisting in the films sputtered with an insufficient H_2S flow during deposition. The film structural as well as the optical properties greatly improved. The direct band gap of the annealed films was at 1.49 eV at room temperature, nearly identical to the value of bulk material. Upon exposure to air, the electrical properties of the as-grown films change tremendously, switching from highly resistive electron dominated (*n*-type) conduction to highly *p*-type conduction. KCN etching removed the Cu_xS segregation on the film surfaces and recovered the film electrical properties to the initial state. Based on surface morphology and compositional analysis of the films, a model was proposed to interpret the observed drastic changes of the film electrical properties upon aging in air and etching with KCN.

The basic achievements in the present work indicate an attractive perspective for the one-stage growth of CIS films by the sputter technique. As demonstrated in this work, *n*-type conducting films can be produced using an In-rich Cu-In alloy target. It is reasonable to expect that by a Cu-rich Cu-In alloy target *p*-type films with adequate hole

concentration and mobility could be obtained. A *p*-type CIS absorber can be combined with *n*-type ZnO and/or ZnO:Al layers, which are normally prepared also by the sputter technique, to form a heterojunction solar cell, suggesting a continuous vacuum process for solar cell production. Our conception is greatly encouraged by a recently published work of Ellmer *et al.*, where a solar cell of 6.4% efficiency prepared by combining a one-step DC magnetron sputtered CIS absorber with magnetron sputtered ZnO/ZnO:Ga layers was demonstrated [1].

Quasi-epitaxial growth of CuInS$_2$ films on sapphire by RF reactive sputtering

Conclusions related to the work on quasi-epitaxial growth of CuInS$_2$ films by RF reactive sputtering can be drawn as follows:

- Thin CIS films (20-100 nm) were "epitaxially" grown on single-crystalline (0001)-sapphire substrates by RF reactive sputtering at 200W and 500°C with an appropriate H$_2$S flow. The well-defined out-of-plane and in-plane lattice ordering of the epilayers was evidenced by XRD rocking curve and Phi-scan measurements, respectively, which also determined the orientation relationship of the heteroepitaxial growth: CIS (112) sapphire (0001), CIS [$\bar{1}$10] sapphire (10$\bar{1}$0). The thin epilayers have a best rocking curve half width of less than 0.05° (180 arcsec), which is not only better than the values obtained for CIS films produced by MBE, but even superior to those for epilayers of binary compounds such as ZnO or GaN prepared by CVD or HVPE [2, 3]. Similar to CIS epilayers grown by MBE on Si (111), two domains, rotated by 180° with each other, coexist in the sputtered CIS epilayers. The similarity of the hexagonal feature of the CIS unit cell in the (112) plane and the sapphire unit cell in the (0001) plane, and the well-fitted side-length of the corresponding hexagons enable heteroepitaxy and lead to the observed orientation relationship between the CIS epilayer and the sapphire substrate. AFM demonstrates a smooth surface of the sputtered epilayers and suggests a three-dimensional island-like growth mechanism.

- Via pre-sputtering of a thin CIS epilayer, thick CuInS$_2$ films were subsequently grown quasi-epitaxially on sapphire substrates. Such a double-layered film has a typical XRD rocking curve half width of approximately 0.1° (360 arcsec), indicating a nearly perfect ordering of the film along the growth direction. The in-plane lattice alignment is, however, much more complex compared to the thin epilayers. XRD polefigure analysis revealed a multi-domain feature of the double-layered films in the (112) plane. In addition to a primary twin that rotated by 180° with respect to the matrix along [221], other domains with different orientations and much lower volumes coexist in the films.

The success of epitaxial growth of CIS on sapphire indicates that heteroepitaxy may not only occur in material systems with similar structural symmetry, e.g., cubic on cubic, tetragonal on cubic, or vice versa, but is also possible for materials with different symmetry, e.g., cubic on hexagonal, tetragonal on hexagonal, or vice versa, if a suitable growth direction is chosen. This finding along with other established examples, such as heteroepitaxy of hexagonal GaN on cubic Si (111), could extend the choice of substrates for the epitaxy technique. As the CIS films can be grown epitaxially on sapphire by sputtering, via MBE or MOCVD, typical techniques for epitaxy, epilayers with more superior quality could be expected to grow on sapphire, which may lead to a deeper insight into the fundamental properties of $CuInS_2$. Moreover, the thin buffer-layer technique introduced in this study provides a new clue for epitaxial growth. This finding is on the one hand similar to the established modulation-growth technique [3], and on the other hand would convert the heteroepitaxial growth to be homoepitaxial-like, due to the pre-deposition of such an ultra-thin nucleation layer.

8 Zusammenfassung

Obwohl eine Vielzahl von Techniken zur Herstellung von $CuInS_2$-Schichten angewendet werden, ist die Effizienz der auf diesem Material basierenden Solarzellen heutzutage auf etwa 12% limitiert. Gründe dafür sind die relativ geringe Qualität und die unzureichende Kenntnis der grundlegenden Eigenschaften des Absorbermaterials. Die Herstellung mittels eines Sputterprozesses bietet die Vorteile einer einfachen Kontrolle der Filmstöchiometrie und der Möglichkeit der Deposition auf großen Flächen bei relativ geringen Kosten. Die Sputtertechnik wird aktuell bei einer Vielzahl von Materialien in der industriellen Produktion genutzt. Aus diesen Gründen wurde in dieser Studie die reaktive RF-Sputtertechnik angewandt, um CIS-Dünnschichten zu deponieren, deren strukturelle, optische und elektrische Eigenschaften zu charakterisieren und einen Prozess, der für die Herstellung von $CuInS_2$-Schichten für photovoltaische Anwendungen geeignet ist, zu optimieren und etablieren. Die Arbeit beinhaltet zwei wesentliche Aspekte, einen Ein-Schritt-Prozess zur Herstellung von CIS-Schichten auf Floatglas und ihre Charakterisierung und das quasi-epitaktische Wachstum von CIS-Filmen auf einkristallinem Saphir mittels reaktivem RF-Sputtern.

Herstellung von $CuInS_2$-Schichten im Ein-Schritt-Sputter-Verfahren

Die untersuchten $CuInS_2$-Schichten wurden auf Floatglas in nur einem Prozessschritt deponiert. Dabei wurden ein legiertes Kupfer-Indium-Target und reiner Schwefelwasserstoff als Arbeits- und Reaktivgas in einem Sputter-Verfahren genutzt.

Zur Optimierung der Schichteigenschaften wurden die Prozessparameter, wie H_2S-Fluss, Substrattemperatur und Sputterleistung, systematisch variiert. Abbildung 8.1 zeigt XRD-Spektren von Proben, die mit unterschiedlichem H_2S-Fluss hergestellt wurden. Bei nicht ausreichendem H_2S-Fluss konnten zusätzlich zu den CIS-Phasen sekundäre Cu-In-Phasen und bei zu hohem H_2S-Fluss Nebenphasen von elementarem Schwefel nachgewiesen werden.

Mit einer RF-Sputterleistung von 200 W, bei Substrattemperaturen ab 400°C und einem H_2S-Fluss im Bereich von 20 bis 29 sccm, was einem Partialdruck von 1.93-2.93×10^{-1} Pa entsprach, konnten qualitativ gute, (112)-orientierte $CuInS_2$-Schichten auf Floatglas abgeschieden werden. Die Erhöhung der Substrattemperatur oder der Sputterleistung erforderte eine Vergrößerung des H_2S-Flusses, um Cu-In-Phasen in den gesputterten Proben zu vermeiden. Die Änderung der Substrattemperatur von 400 auf 500°C bewirkte eine Verbesserung der strukturellen Eigenschaften der Schichten, eine

Erhöhung der Korngrößen von etwa 95 auf 145 nm und eine Steigerung der optischen Qualität, die Bandlücke verschob sich von 1.27 zu 1.44 eV. Die optimierten Prozessparameter und die sich daraus ergebenden strukturellen und optischen Eigenschaften der CIS-Schichten sind in Tabelle 8.1 zusammengefasst.
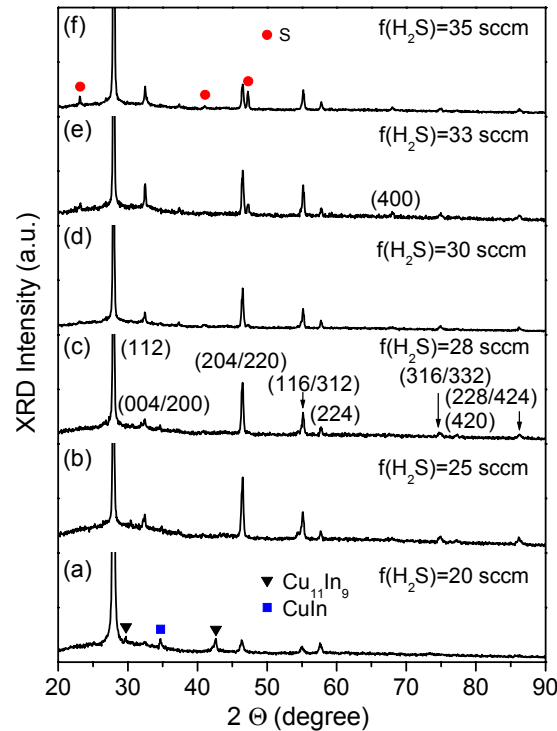

Abb. 8.1: XRD-Spektren von CIS-Schichten, die bei 500°C, mit 200 W und unterschiedlichen H_2S-Flüssen hergestellt wurden.

Tab. 8.1: Optimierte Parameter des Ein-Schritt-Sputter-Prozesses und die resultierenden optischen und strukturellen Eigenschaften typischer CIS-Filme.

Sputter conditions			Structural properties			Optical properties
Power (W)	Substrate Temperature (°C)	H_2S flow (sccm)	FWHM of (112) (°)	Grain size XRD (nm)	Grain size AFM/SEM (nm)	Optical bandgap (eV)
200	400	25 (20-29)	0.239	59	~95	1.24-1.37
200	500	28 (25-30)	0.162	132	~145	1.42-1.44
300	400	40	0.241	58	-	1.33
300	500	45	0.159	139	-	1.44

Mo- oder ZnO-Pufferschichten auf dem Floatglassubstrat ermöglichen Schicht-depositionen bei einer relativ niedrigen Temperatur von 200°C. Außerdem funktionieren

diese Zwischenschichten als wirksame Barriere gegen die Natrium-Diffusion aus dem Glas in die Funktionsschicht.
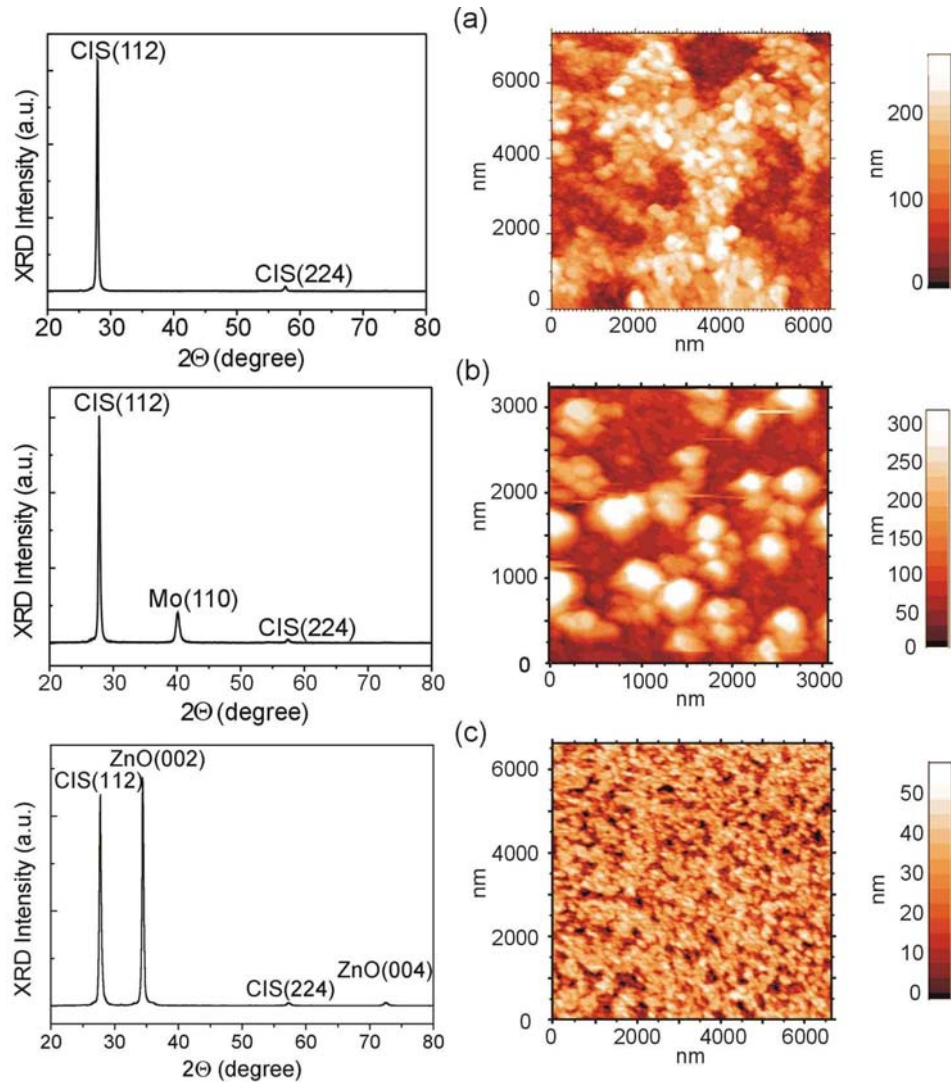
Abb. 8.2, links: XRD-Spektren von typischen CIS-Schichten auf reinem (a), mit Mo- (b) und mit ZnO-beschichtetem (c) Floatglas; rechts: AFM-Bilder von den entsprechenden Oberflächen der CIS-Schichten.

Die Oberfläche und die strukturellen Eigenschaften der synthetisierten CIS-Schichten wurden detailliert mittels AFM, SEM, EDX, GIXRD, XRR, XPS, UPS und SIMS charakterisiert. XRD- und GIXRD-Untersuchungen ergaben, dass die gesputterten $CuInS_2$-Proben generell eine bevorzugte (112)-Orientierung besitzen. Im linken Teil der Abbildung 8.2 sind XRD-Spektren von typischen $CuInS_2$-Schichten auf reinem, mit Mo- und ZnO-beschichtetem Floatglas dargestellt. Alle Spektren zeigen nur die (112)- und (224)-Reflexe von CIS, die durch dieselben Netzebenen hervorgerufen werden. Im rechten Teil von Abb. 8.2 sind die entsprechenden AFM-Aufnahmen der Oberflächen der

untersuchten CIS-Filme abgebildet. Schichten, die auf reinem und auf Mo-beschichtetem Floatglas deponiert wurden, haben typischerweise eine raue Oberfläche und inkohärente Ausscheidungen sind deutlich nachweisbar. CIS-Filme, die auf einer ZnO-Pufferschicht gewachsen sind, zeigen eine glattere Oberfläche, aber kleinere Körner.

In Tabelle 8.2 werden die wichtigsten Prozessparameter und die strukturellen Eigenschaften der CuInS$_2$-Filme auf den unterschiedlichen Substraten verglichen.

Tab. 8.2: Substrattemperatur, Halbwertsbreite des (112)-Reflexes, mittlere Korngröße und Faktor der bevorzugten Orientierung für CIS-Schichten auf verschiedenen Substraten.

Layer system	Substrate temperature (°C)	FWHM of (112) peak (°)	Grain size		f(112)
			XRD	AFM	
			(nm)		
CIS/Glass	400	0.278	54	95	0.96
CIS/Mo/Glass	200	0.288	48	85	0.95
CIS/ZnO/Glass	200	0.352	34	55	0.95

Die XRR-Messungen ergaben eine Oberflächendichte der auf Floatglas gesputterten Filme von 5.01 g/cm^{-3}, die den theoretischen Wert für reines CIS übersteigt und damit auf in der Schicht existierende sekundäre Phasen hinweist. Weiterhin wurde mittels XRR die Depositionsrate des Ein-Schritt-Sputter-Verfahrens zu etwa 33 nm/min bestimmt.

SEM- und EDX-Studien wurden genutzt, um die Segregationen auf den Schichtoberflächen zu identifizieren. Es zeigte sich, dass das Cu/In-Verhältnis in den Oberflächenausscheidungen deutlich von dem in der Schicht abweicht. Trotz der Cu$_x$S-Ausscheidungen konnte mit XPS-Messungen nachgewiesen werden, dass die Schichtoberfläche im Vergleich zum Volumen Indium-reich ist und dass die Oberflächeneigenschaften durch die Oxidation bei Lagerung an Luft dominiert werden. Die SIMS-Untersuchungen ergaben, dass unabhängig vom Substrat die Tiefenhomogenität der erzeugten CIS-Schichten gut ist.

Die strukturellen, optischen und elektrischen Eigenschaften der stöchiometrischen, einphasigen CuInS$_2$-Schichten, die mit dem Ein-Schritt-Prozess hergestellt wurden, können signifikant durch eine Nachbehandlung beeinflusst werden. Eine Ausheilung im Vakuum bei 500°C für 2 Stunden bewirkte eine Rekristallisation der gesputterten Schichten und somit eine Verbesserung ihrer optischen Eigenschaften. Abbildung 8.3 zeigt ein Transmissionsspektrum bei Raumtemperatur (a) und die Bestimmung der Bandlücke (b) für solch einen getemperten Film. Die ausgeheilten Schichten haben eine direkte Bandlücke von 1.49 eV bei Raumtemperatur, die sehr gut mit dem Wert für Volumenmaterial übereinstimmt. Die Ausheilung in H$_2$S-Athmosphäre bei 500°C von

Proben, die mit unzureichendem H_2S-Fluss hergestellt wurden, resultierte in der Beseitigung der sekundären Cu-In-Phasen in den CIS-Filmen. Die strukturellen und optischen Eigenschaften der CIS-Schichten konnten also durch Temperaturbehandlung deutlich verbessert werden.
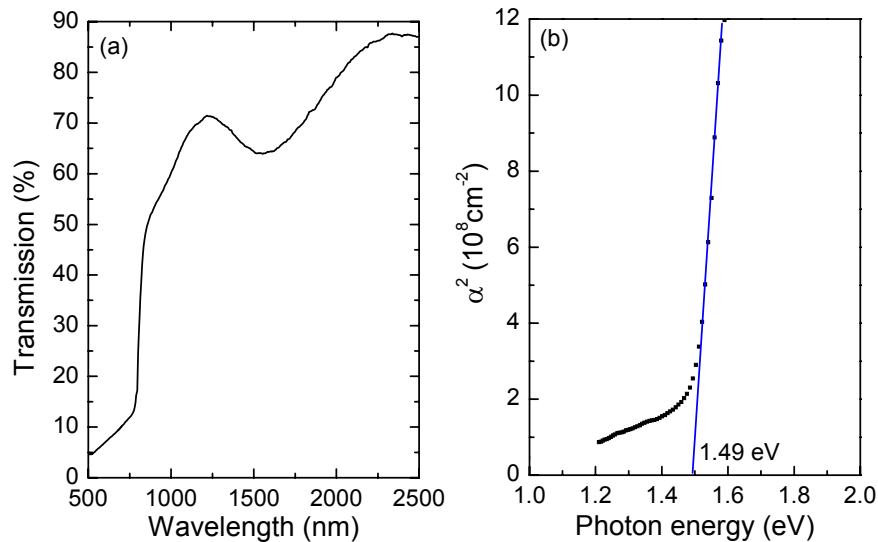

Abb. 8.3: Optisches Transmissionsspektrum (a) und Bestimmung der Bandlücke (b) für einen unter Vakuum bei 500°C für 2 h ausgeheilten CIS-Film.

Das elektrische Verhalten der gesputterten Proben änderte sich vollständig, nachdem diese der Einwirkung von Luft ausgesetzt wurden. Die direkt nach dem Wachstum hochohmigen, schwach *n*-leitenden Schichten zeigten nach Lagerung an Luft starke *p*-Leitung. Durch einen Ätzschritt mit KCN wurden die Cu_xS-Ausscheidungen und die oberflächlich gebildeten Oxide abgetragen und die ursprünglichen, elektrischen Eigen-schaften wieder erreicht. In Tabelle 8.3 sind die elektrischen Daten, die bei Raumtemperatur gemessen wurden, für $CuInS_2$-Schichten direkt nach der Herstellung, nach der Einwirkung von Luft und der anschließenden KCN-Ätzung zusammengestellt. Ein Modell, das auf die Untersuchungen zur Oberflächen-Morphologie und auf der Analyse der Zusammensetzung der Schichten basiert, wurde entwickelt, um die drastischen Änderungen der elektrischen Eigenschaften der CIS-Filme nach Alterung an Luft und nach Abätzen der Oberflächenschicht zu interpretieren.

Tab. 8.3: Elektrische Daten von CIS-Filmen direkt nach der Herstellung, nach der Einwirkung von Luft und dem anschließenden KCN-Ätzschritt.

Film	Resistivity (Ωcm)	Carrier density (cm^{-3})	Hall mobility (cm^2/Vs)	Conduction type
Fresh	2×10^3-10^4	3×10^{14}-10^{15}	2-20	n
Aged in air	0.1-2	10^{19}-10^{20}	0.2-0.7	p
KCN etched	6×10^2-2.5×10^4	4×10^{13}-3×10^{15}	2-100	n

Die grundlegenden Ergebnisse dieser Arbeit zeigen eine innovative Perspektive zur Herstellung von CIS-Dünnschichten in einem Ein-Schritt-Sputter-Prozess. Es wurde demonstriert, dass sich bei Nutzung eines In-reichen, legierten Cu/In-Targets n-leitende Filme deponieren lassen, was zu der Annahme berechtigt, dass mit einem Cu-reichen Target p-leitende Schichten mit entsprechender Löcher-Konzentration und Beweglichkeit erhalten werden können. Dies eröffnet die Möglichkeit zur Solarzellenproduktion in einem kontinuierlichen Vakuumprozess, ein p-leitender CIS-Absorber wird mit einer n-leitenden ZnO- und/oder ZnO:Al-Schicht, die auch mit Sputterverfahren hergestellt werden kann, kombiniert.

Quasi-epitaktisches Wachstum von CuInS$_2$ durch reaktives Sputtern

CuInS$_2$-Dünnschichten mit einer Dicke von 20 bis 100 nm wurden auf einkristallinen (0001)-Saphirsubstraten in einem reaktiven RF-Sputterprozess mit einer Sputterleistung von 200 W, bei einer Substrattemperatur von 500°C und einem entsprechenden H$_2$S-Fluss „epitaktisch" gewachsen.

Die eindeutige Gitterordnung für Orientierungen sowohl in der Ebene als auch aus der Ebene der epitaktischen Schichten wurde durch Röntgenbeugung anhand von Rocking-Kurven und Phi-Scans nachgewiesen. Abbildung 8.4 zeigt das Θ-2Θ-Spektrum (a) und die Rocking-Kurve der (112)-Ebene (b) einer solchen Schicht. Die Orientierung CIS(112) || Saphir(0001) konnte damit nachgewiesen werden. Das Θ-2Θ-Spektrum zeigt nur die Reflexe, die der (112)-, (224)- und (336)-Ebene von CuInS$_2$ entsprechen.

Die Halbwertsbreite der Rocking-Kurve für die gesputterten CIS-Schichten beträgt etwa 0.05° (180″). Sie sie ist zwar nicht besser als bei mit MBE gewachsenen Schichten, aber geringer als bei binären Verbindungen wie ZnO- oder GaN-Epischichten, die mit CVD oder HVPE hergestellt wurden. Auch daran wird die Natur des epitaktischen Wachstums von gesputtertem CuInS$_2$ auf Saphir deutlich. Ähnlich wie bei CIS-Epischichten, die mit MBE auf Si(111) abgeschieden wurden, koexistieren in den gesputterten, epitaktischen Schichten zwei Domänen, die gegeneinander um 180° gedreht

sind. Abbildung 8.5 verdeutlicht diesen Sachverhalt. Die Verknüpfung der Orientierung in der Ebene beim heteroepitaktischen Wachstum konnte mit Röntgenbeugung bestimmt werden: CIS[$\bar{1}$10] ∥ Saphir(10$\bar{1}$0).
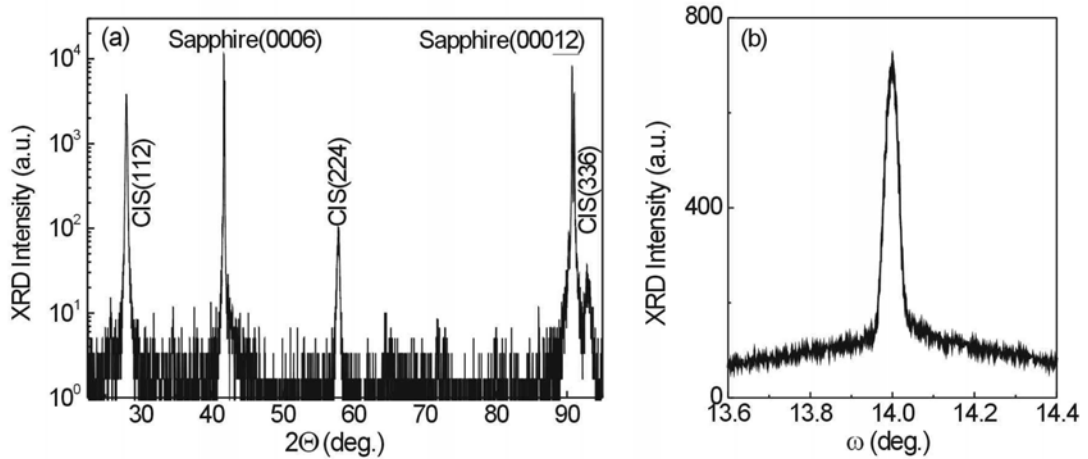

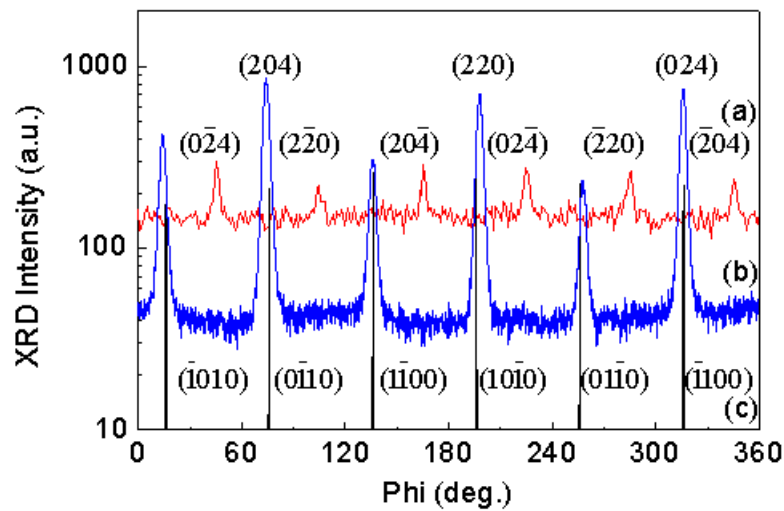Abb. 8.4: Typisches XRD-Spektrum (a) und Rocking-Kurve der (112)-Ebene (b) einer auf Saphir gesputterten CIS-Schicht.

Abb. 8.5: Phi-Scan in der Ebene einer auf Saphir gesputterten CIS-Schicht. (a) aufgenommen für CIS-{2$\bar{2}$0} mit einem Glanzwinkel von 1°, (b) aufgenommen für CIS-{204} mit einem Neigungswinkel (Chi) von 35.5°, (c) aufgenommen für Saphir-{10$\bar{1}$0} mit einem Glanzwinkel von 1°.

Die Ähnlichkeit des hexagonalen Charakters von CIS in der (112)-Ebene und von Saphir in der (0001)-Ebene und die gut übereinstimmenden Kantenlängen entsprechender

Hexagons erlauben die Heteroepitaxie und ergeben das beobachtete Orientierungs-verhältnis zwischen den CIS-Epischichten und dem Saphirsubstrat. Untersuchungen zur Morphologie zeigen eine glatte Oberfläche der epitaktischen Schichten und weisen auf einen dreidimensionalen, inselähnlichen Wachstumsmechanismus hin. In Abbildung 8.6 (a) ist eine AFM-Abbildung der CIS-Epischichten dargestellt.
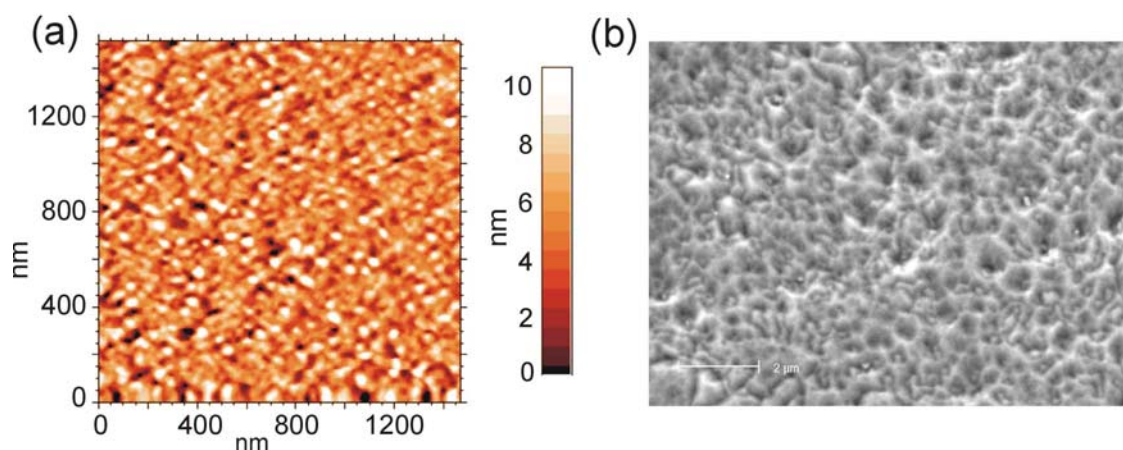
Abb. 8.6: AFM-Bild (a) einer auf Saphir gesputterten, dünnen CIS-Schicht und SEM-Bild (b) einer CIS-Doppelschicht.

Mit Hilfe von vorgesputterten, dünnen CIS-Epischichten als Nukleationsschicht wurden auch dicke (etwa 1000 nm) $CuInS_2$-Filme quasi-epitaktisch auf Saphirsubstraten abgeschieden. Die Halbwertsbreite der Rocking-Kurve für solch eine Doppelschicht betrug etwa 0.1° (360″), was auf eine nahezu perfekte Ordnung der Schichten entlang der Wachs-tumsrichtung hinweist. Die Gitterordnung in der Ebene ist aber verglichen mit der der dünnen Epischichten wesentlich komplexer. Die Analyse mittels einer XRD-Polefigur ergab einen Multi-Domänen-Charakter der CIS-Doppelschichten in der (112)-Ebene. Abbildung 8.7 illustriert die typischen 2Θ-Phi- und die Chi-Phi-Abbildungen von CIS-Schichten, die auf einer dünnen CIS-Nukleationsschicht hergestellt wurden. Zusätzlich zu der ursprünglichen Doppelstruktur, die durch eine 180°-Drehung um die [221]-Richtung entstand, konnten Domänen anderer Orientierungen und mit kleinerem Volumenanteil in den Schichten nachgewiesen werden. Eine typische Oberfläche der Doppelschichten, die Löcher und Schädigungen zeigt, ist in einem SEM-Bild in Abbildung 8.6 (b) dargestellt.
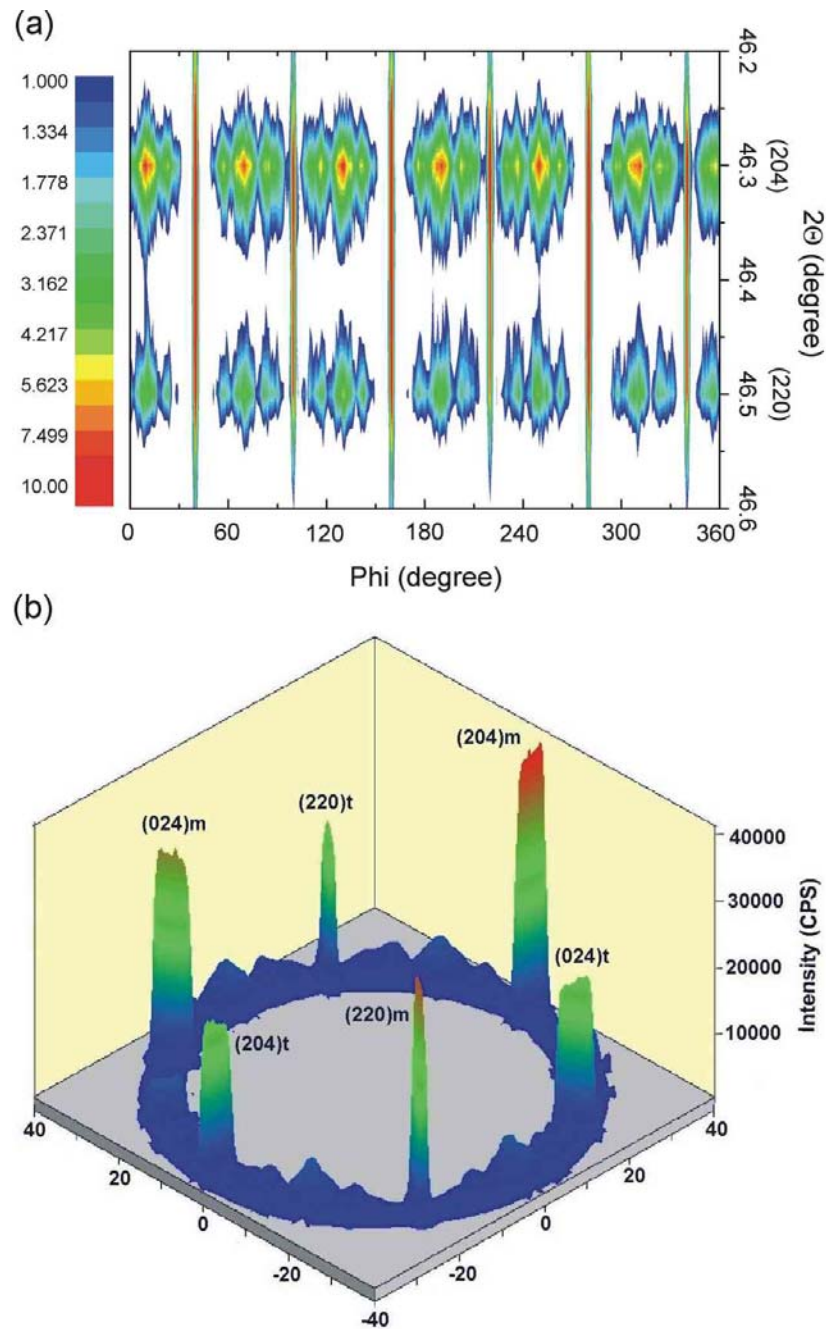
Abb. 8.7: Phi-2Θ-Bild mit einem festen Neigungswinkel Chi von 35.5° (a) und dreidimensionale Chi-Phi-Abbildung von CIS-{204} (b) einer auf Saphir gesputterten CIS-Doppelschicht.

Das erfolgreiche epitaktische Wachstum von $CuInS_2$ auf Saphir verdeutlicht, dass bei Auswahl einer geeigneten Wachstumsrichtung die Möglichkeit von Heteroepitaxie nicht nur für ähnliche strukturelle Symmetrien besteht, wie kubisch auf kubisch oder tetragonal auf kubisch und umgekehrt, sondern auch für Materialien mit unterschiedlichen Symmetrien, z.B. kubisch auf hexagonal oder tetragonal auf hexagonal und umgekehrt. Dieses Ergebnis zeigt gemeinsam mit anderen etablierten Beispielen, wie der Heteroepitaxie von hexagonalem GaN auf kubischem Si(111), dass die Auswahl für

Materialen, die bei Epitaxie-Techniken eingesetzt werden, erweitert werden kann. Die epitaktische Deposition von CIS-Schichten auf Saphir mittels Sputtern, MBE oder auch MOCVD führt zu einer Verbesserung der Qualität des Materials und somit zur Möglichkeit des tieferen Verständnisses der fundamentalen Eigenschaften von $CuInS_2$. Weiterhin liefert das hier vorgestellte Verfahren, das eine dünne CIS-Nukleationsschicht nutzt, einen neuen Schlüssel für das epitaktische Wachstum dieser Verbindung. Dieser Prozess ist einerseits ähnlich der etablierten Modulations-Wachstumstechnik, aber andererseits wird das heteroepitaktische Wachstum in quasi-homoepitaktisches auf Grund der vorgesputterten, dünnen CIS-Schicht konvertiert.

Abbreviations

AFM	**A**tomic **F**orce **M**icroscopy
at.	**at**omic
bc	**b**ody **c**entered
BF	**B**right **F**ield
BST	**(BaSr)**TiO_3
CH	**Ch**alcopyrite
CGS	**C**u**G**a**S**$_2$
CIS	**C**u**I**n**S**$_2$
CVD	**C**hemical **V**apor **D**eposition
DC	**D**irect **C**urrent
DF	**D**ark **F**ield
EDX	**E**nergy **D**ispersive **X**-ray Analysis
ESCA	**E**lectron **S**pectroscopy for **C**hemical **A**nalysis
fcc	**f**ace **c**entered **c**ubic
FWHM	**F**ull **W**idth at **H**alf **M**aximum
GID	**G**razing **I**ncidence **D**iffraction
GIXRD	**G**razing **I**ncidence **X**-**R**ay **D**iffraction
HRTEM	**H**igh **R**esolution **T**ransmission **E**lectron **M**icroscopy
HVPE	**H**ydride **V**apor **P**hase **E**pitaxy
JCPDS	**J**oint **C**ommittee on **P**owder **D**iffraction **S**tandards
MBE	**M**olecular **B**eam **E**pitaxy
MF	**M**id-**F**requency
MFC	**M**ass **F**low **C**ontroller
MOCVD	**M**etal**o**rganic **C**hamical **V**apor **D**eposition
PL	**P**hoto**l**uminescence
PV	**P**hoto**v**oltaic
PVD	**P**hysical **V**apor **D**eposition
PZT	**P**b**(ZrTi)**O$_3$
RBS	**R**utherford **B**ackscattering **S**pectrometry
RE-TM	**R**are-**E**arth-**T**ransition-**M**etal
RF	**R**adio **F**requency
RMS	**R**oot **M**ean **S**quare
RT	**R**oom **T**emperature

SADP	**S**elected **A**rea **D**iffraction **P**attern
sccm	**S**tandard **C**ubic **C**entimeter per **M**in
SEM	**S**canning **E**lectron **M**icroscopy
SIMS	**S**econdary **I**on **M**ass **S**pectrometry
TEM	**T**ransmission **E**lectron **M**icroscopy
UPS	**U**ltraviolet **P**hotoelectron **S**pectroscopy
XPS	**X**-ray **P**hotoelectron **S**pectroscopy
XRD	**X-R**ay **D**iffraction
XRR	**X-R**ay **R**eflectometry

References

Chapter 1

[1]   A. E. Becquerel, *Comt. Rend. Acad. Sci.*, vol. 9, p. 561, 1839.

[2]   A. Goetzberger, C. Hebling, and H. W. Schock, *Mater. Sci. Eng. R*, vol. 40, p. 1, 2003.

[3]   A. Catalano, *Solar Energy Mater. Solar Cells*, vol. 41/42, p. 205, 1996.

[4]   R. W. Birkmire, *Solar Energy Mater. Solar Cells*, vol. 65, p. 17, 2001.

[5]   H. W. Schock and R. Noufi, *Prog. Photovoltaic. Res. Appl.*, vol. 8, p. 151, 2000.

[6]   M. A. Contreras, B. Egaas, K. Ramanathan, J. Hiltner, F. Hasoon, and R. Noufi, *Prog. Photovolt. Res. Appl.*, vol. 7, p. 311-316, 1999.

[7]   C. H. Henry, *J. Appl. Phys.*, vol. 51, p. 4494, 1980.

[8]   S. Siebentritt, *Thin Solid Films*, vol. 403-404, p. 1, 2002.

[9]   R. Klenk, P. Dobson, M. Falz, N. Janke, J. Kaer, I. Luck, A. Perez-Rodiguez, R. Scheer, and E. Terzini, *Proceedings of 16th EPVSEC*. Glasgow, 2000.

[10]   K. Siemer, J. Klaer, I. Luck, J. Bruns, R. Klenk, and D. Bräunig, *Solar Energy Mater. Solar Cells*, vol. 67, p. 159, 2001.

[11]   L. Stolt, J. Hedström, J. Kessler, M. Ruckh, K. O. Velthaus, and H. W. Schock, *Appl. Phys. Lett.*, vol. 62, p. 597, 1993.

[12]   L. L. Kazmerski and G. A. Sanborn, *J. Appl. Phys.*, vol. 48, p. 3178, 1977.

[13]   R. Scheer, T. Walter, H. W. Schock, M. L. Fearheiley, and H. J. Lewerenz, *Appl. Phys. Lett.*, vol. 63, p. 3294, 1993.

[14]   Y. Ogawa, A. Jäger-Waldau, Y. Hashimoto, and K. Ito, *Jpn. J. Appl. Phys.*, vol. 33, p. L1775, 1994.

[15]   H. L. Hwang, C. Y. Sun, C. S. Fang, S. D. Chang, C. H. Cheng, H. M. Yang, H. H. Lin, and T.Tuwan-mu, *J. Cryst. Growth*, vol. 55, p. 116, 1981.

[16]   H. L. Hwang, C. L. Cheng, L. M. Liu, Y. C. Liu, and C. Y. Sun, *Thin Solid Films*, vol. 67, p. 83, 1980.

[17]   G. Hodes, T. Engelhard, and D. Cahen, *Thin Solid Films*, vol. 128, p. 93, 1985.

[18]   H. Onagawa and K. Miyashita, *Jpn. J. Appl. Phys.*, vol. 23, p. 965, 1984.

[19]   H. Metzner, T. Hahn, J. H. Bremer, and J. Conrad, *Appl. Phys. Lett.*, vol. 69, p. 1900, 1996.

[20]   T. Hahn, H. Metzner, B. Plikat, and M. Seibt, *Appl. Phys. Lett.*, vol. 72, p. 2733, 1998.

[21]   R. Hunger, R. Scheer, K. Diesner, D. Su, and H. J. Lewerenz, *Appl. Phys. Lett.*, vol. 69, p. 3010, 1996.

Chapter 2

[1]   J. L. Shay and J. H. Wernik, *Ternary Chalcopyrite Semiconductors: Growth, Electronic Properties and Applications*. Oxford: Pergamon Press, 1975.

[2]   S. Wagner, J. L. Shay, B. Tell, and H. M. Kasper, *Appl. Phys. Lett.*, vol. 22, p. 351, 1973.

[3]   R. C. Smith, *Journal de Physique, Colloque C3, supplement au n^0 9*, Tome 36, p. C3-89, 1975.

[4]   S. Wagner, J. L. Shay, and H. M. Kasper, *Journal de Physique, Colloque C3, supplement au n^0 9*, Tome 36, p. C3-101, 1975.

[5]   P. M. Bridenbaugh and P. Migliorato, *Appl. Phys. Lett.*, vol. 26, p. 459, 1975.

[6]   J. E. Jaffe and A. Zunger, *Phys. Rev. B*, vol. 28, p. 5822, 1983.

[7]   S. C. Abrahams and J. L. Bernstein, *J. Chem. Phys.*, vol. 59, p. 5415, 1973.

[8]   H. W. Spiess, U. Haeberlen, G. Brandt, A. Räuber, and J. Scheider, *Phys. Stat. Sol. (b)*, vol. 62, p. 183, 1974.

[9]   JCPDS powder diffraction file No. 27-0159.

[10]   J. J. M. Binsma, L. J. Giling, and J. Bloem, *J. Cryst. Growth*, vol. 50, p. 429, 1980.

[11]   S. H. Wei, L. G. Ferreira, and A. Zunger, *Phys. Rev. B*, vol. 45, p. 2533, 1992.

[12]   S. H. Wei, S. B. Zhang, and A. Zunger, *Phys. Rev. B*, vol. 59, p. R2478, 1999.

[13]   D. S. Su and S. H. Wei, *Appl. Phys. Lett.*, vol. 74, p. 2483, 1999.

[14]   JCPDS powder diffraction file No. 27-1402.

[15]   JCPDS powder diffraction file No. 05-0566.

[16]   K.-J. Range, G. Engert, and A. Weiss, *Solid State Comm.*, vol. 7, p. 1749, 1969.

[17]   J. E. Jaffe and A. Zunger, *Phys. Rev. B*, vol. 27, p. 5176, 1983.

[18]   S. Kono and M. Okusawa, *J. Phys. Soc. Jpn.*, vol. 37, p. 1301, 1974.

[19]   W. Braun, A. Goldmann, and M. Cardona, *Phys. Rev. B*, vol. 10, p. 5069, 1974.

[20]   M. I. Alonso, K. Wakita, J. Pascual, M. Garriga, and N. Yamamoto, *Phys. Rev. B*, vol. 63, p. 075203-1, 2001.

[21]   B. Tell, J. L. Shay, and H. M. Kasper, *Phys. Rev. B*, vol. 4, p. 2463, 1971.

[22]   A. N. Tiwari, D. K. Pandya, and K. L. Chopra, *Thin Solid Films*, vol. 130, p. 217, 1985.

[23]   R. W. Miles, K. T. R. Reddy, and I. Forbes, *J. Cryst. Growth*, vol. 198/199, p. 316, 1999.

[24]   Y. Ogawa, S. Uenishi, K. Tohyama, and K. Ito, *Solar Energy Mater. Solar Cells*, vol. 35, p. 157, 1994.

[25]   L. Y. Sun, L. L. Kazmerski, A. H. Clark, P. J. Ireland, and D. W. Morton, *J. Vac. Sci. Technol.*, vol. 15, p. 265, 1978.

[26]   L. L. Kazmerski and C. C. Shieh, *Thin Solid Films*, vol. 41, p. 35, 1977.

[27]   D. C. Look and J. C. Manthuruthil, *J. Phys. Chem. Solids*, vol. 37, p. 173, 1976.

[28]   B. Tell, J. L. Shay, and H. M. Kasper, *J. Appl. Phys.*, vol. 43, p. 2469, 1972.

[29]   L. L. Kazmerski, M. S. Ayyagari, and G. A. Sanborn, *J. Appl. Phys.*, vol. 46, p. 4865, 1975.

[30]   S. P. Grindle, C. W. Smith, and S. D. Mittleman, *Appl. Phys. Lett.*, vol. 35, p. 24, 1979.

[31]   H. L. Hwang, C. C. Tu, J. S. Maa, and C. Y. Sun, *Solar Energy Mater.*, vol. 2, p. 433, 1980.

[32]   Y. L. Wu, H. Y. Lin, C. Y. Sun, M. H. Yang, and H. L. Hwang, *Thin Solid Films*, vol. 168, p. 113, 1989.

[33]   H. Y. Ueng and H. L. Hwang, *J. Phys. Chem. Solids*, vol. 50, p. 1297, 1989.

[34]   A. W. Verheijen, L. J. Giling, and J. Bloem, *Mater. Res. Bull.*, vol. 14, p. 237, 1979.

[35]   G. Massé and E. Rediai, *J. Appl. Phys.*, vol. 65, p. 1154, 1987.

[36]   H. Y. Ueng and H. L. Hwang, *J. Appl. Phys.*, vol. 62, p. 434, 1987.

[37]   N. Lablou and G. Massé, *J. Appl. Phys.*, vol. 52, p. 978, 1981.

[38]   F. A. Kroger, *The Chemsitry of Imperfect Crystals, 2nd Ed, Vol. 2*. Amsterdam: North-Holland, 1974.

[39]   H. L. Hwang, L. M. Liu, M. H. Yang, J. S. Chen, J. R. Chen, and C. Y. Sun, *Solar Energy Mater.*, vol. 7, p. 225, 1982.

[40]   C. Rincon and S. M. Wasim, *MRS Symp. TMC*, p. 443, 1987.

[41]   H. J. Hsu, N. H. Yang, R. S. Tang, T. M. Hsu, and H. L. Hwang, *J. Cryst. Growth*, vol. 20, p. 83, 1984.

[42]   A. Rockett and R. W. Birkmire, *J. Appl. Phys.*, vol. 70, p. R81, 1991.

Chapter 3

[1]   K. Siemer, J. Klaer, I. Luck, J. Bruns, R. Klenk, and D. Bräunig, *Solar Energy Mater. Solar Cells*, vol. 67, p. 159, 2001.

[2]   L. L. Kazmerski and G. A. Sanborn, *J. Appl. Phys.*, vol. 48, p. 3178, 1977.

[3]   R. Scheer, T. Walter, H. W. Schock, M. L. Fearheiley, and H. J. Lewerenz, *Appl. Phys. Lett.*, vol. 63, p. 3294, 1993.

[4]   Y. Ogawa, A. Jäger-Waldau, Y. Hashimoto, and K. Ito, *Jpn. J. Appl. Phys.*, vol. 33, p. L1775, 1994.

[5]   H. L. Hwang, C. Y. Sun, C. S. Fang, S. D. Chang, C. H. Cheng, H. M. Yang, H. H. Lin, and T.Tuwan-mu, *J. Cryst. Growth*, vol. 55, p. 116, 1981.

[6]   H. L. Hwang, C. L. Cheng, L. M. Liu, Y. C. Liu, and C. Y. Sun, *Thin Solid Films*, vol. 67, p. 83, 1980.

[7]   G. Hodes, T. Engelhard, and D. Cahen, *Thin Solid Films*, vol. 128, p. 93, 1985.

[8]   H. Onagawa and K. Miyashita, *Jpn. J. Appl. Phys.*, vol. 23, p. 965, 1984.

Chapter 4

[1]   B. E. Warren, *X-ray Diffraction*: Addison-Wesley Publishing Company, 1969, p. 253.

[2]   B. D. Cullity, *Elements of X-Ray Diffraction, 2nd ed. Reading*. Mass: Addison-Wesley, 1978.

[3]   A. Krost, G. Bauer, and J. Woitok, *Optical Characterization of Epitaxial Semiconductor Layers,* G. Bauer and W. Richter (Eds). Berlin: Springer-Verlag, 1996.

[4]   G. M. Zorn, *Siemens Analytical Application Note*, vol. 337, 1994.

[5]   Bruker AXS, DIFFRAC[plus] REFSIM version 2.0.

[6]   A. H. Compton, *Philos. Mag.*, vol. 45, p. 1121, 1923.

[7]   H. Kiessig, *Ann. Phys.*, vol. 10, p. 769, 1931.

[8]   L. G. Parrat, *Phys. Rev.*, vol. 95, p. 359, 1954.

[9]   B. Vidal and P. Vincent, *Appl. Optics*, vol. 23, p. 1794, 1984.

[10]   D. K. G. d. Boer, A. J. G. Leenaers, and W. W. v. d. Hoogenhof, *X-Ray Spectrometry*, vol. 24, p. 91, 1995.

[11]   B. Lengeler, *Adv. X-Ray Anal.*, vol. 35, p. 127, 1992.

[12]   H. Zabel, *Appl. Phys. A*, vol. 58, p. 159, 1994.

[13]   D. B. Wiliams and C. B. Carter, *Transmission electron microscopy: a textbook for materials science*. New York: Plenum press, 1996.

[14]   G. Thomas, *Transmission Electron Microscopy of Metals*. New York: John Wiley and Sons Inc., 1962.

[15]   J. C. H. Spence, *Experimental High Resolution Electron Microscopy, Monographs on the Physics and Chemistry of Materials*. Oxford: Clarendon Press, 1981.

[16]   J. M. Gibson, *High Resolution Transmission Electron Microscopy, MRS Bull. (March), 27*, 1991.

[17]   I. Österreicher, Dissertation: I. Phys. Inst., Justus-Liebig-University Giessen, 2003.

[18]   S. Hüfner, *Photoelectron spectroscopy*. Berin, Heidelberg, New York: Springer-Verlag, 1996.

[19]   H. Ibach (Ed.), *Electron spectroscopy for surface analysis*. Berlin, Heidelberg, New York,: Springer-Verlag, 1977.

[20]   D. Briggs and M. P. Seah (Eds.), *Practical surface analysis by auger and X-ray photoelectron spectroscopy*. Chichester, New York: John Wiley & Sons, 1983.

[21]   J. F. Moulder, W. F. Stickle, P. E. Sobol, and K. D. Bomben, *Handbook of X- ray Photoelectron Spectroscopy; A Reference Book of Standard Spectra for Identification and Interpretation of XPS Data*. Eden Prairie, Minnesota: Perkin-Elmer Corporation, 1992.

[22] R. G. Wilson, F. A. Stevie, and C. W. Magee, *Secondary ion mass spectrometry; a practical handbook for depth profiling and bulk impurity analysis*. New York: John Wiley & Sons, 1989.

[23] J. C. Vickerman, A. Brown, and N. M. Reed, *Secondary ion mass spectrometry; Principles and applications*. Oxford: Clarendon Press, 1989.

[24] A. Benninghoven, F. G. Rüdenauer, and H. W. Werner (Eds.), *Secondary ion mass spectrometry; Basic concepts, instrumental aspects, applications and trends*. Chemical Analysis, New York: John Wiley & Sons, 1987.

[25] O. C. Wells, *Scanning Electron Microscopy*. N. Y.: McGraw-Hill Book Company, 1974.

[26] D. E. Newbury, D. C. Joy, P. Echlin, C. E. Fiori, and J. I. Goldstein, *Advanced Scanning Electron Microscopy and X-Ray Microscopy*. New York: Plenum Press, 1986.

[27] I. M. Watt, *Principles and Practice of Electron Microscopy*. Cambridge University Press, 1985.

[28] D. Rugar and P. Hansma, *Phys. Today*, vol. 43, p. 23, 1990.

[29] J. I. Pankove, *Optical processes in semiconductors*. New Jersey: Prentice-Hall, Englewood Cliffs, 1971.

[30] T. Krämer, Diplom Thesis: I. Phys. Inst., Justus-Liebig University Giessen, 2002.

Chapter 5

[1] R. W. Miles, K. T. R. Reddy, and I. Forbes, *J. Cryst. Growth*, vol. 198/199, p. 316, 1999.

[2] F. O. Adurodija, J. Song, S. D. Kim, S. K. Kim, and K. H. Yoon, *Jpn. J. Appl. Phys.*, vol. 37, p. 4248, 1998.

[3] T. Watanabe and M. Matsui, *Jpn. J. Appl. Phys.*, vol. 35, p. 1681, 1996.

[4] S. P. Grindle, C. W. Smith, and S. D. Mittleman, *Appl. Phys. Lett.*, vol. 35, p. 24, 1979.

[5] T. Watanabe, M. Matsui, and K. Mori, in *Solar Energy Mater. Solar Cells*, vol. 35, 1994, p. 239.

[6] Y. B. He, A. Polity, H. R. Alves, I. Österreicher, W. Kriegseis, D. Pfisterer, B. K. Meyer, and M. Hardt, *Thin Solid Films*, vol. 403-404, p. 62, 2002.

[7] Y. B. He, A. Polity, R. Gregor, D. Pfisterer, I. Österreicher, D. Hasselkamp, and B. K. Meyer, *Physica B*, vol. 308-310, p. 1074, 2001.

[8] Y. B. He, T. Krämer, I. Österreicher, A. Polity, R. Gregor, W. Kriegseis, D. Hasselkamp, and B. K. Meyer, *Jpn. J. Appl. Phys.*, vol. 41, p. L 484, 2002.

[9] Y. B. He, T. Krämer, A. Polity, R. Gregor, W. Kriegseis, I. Oesterreicher, D. Hasselkamp, and B. K. Meyer, *Thin Solid Films*, vol. 431-432, p. 232, 2003.

[10] T. Yamaguchi, J. Matsufusa, and A. Yoshida, *J. Appl. Phys.*, vol. 72, p. 5657, 1992.

[11]   F. K. Lotgering, *J. Inorg. Nucl. Chem.*, vol. 9, p. 113, 1959.

[12]   Y. B. He, T. Krämer, A. Polity, M. Hardt, and B. K. Meyer, *Thin Solid Films*, vol. 431-432, p. 126, 2003.

[13]   B. E. Warren, *X-ray Diffraction*: Addison-Wesley Publishing Company, 1969, p. 253.

[14]   Y. Ogawa, S. Uenishi, K. Tohyama, and K. Ito, *Solar Energy Mater. Solar Cells*, vol. 35, p. 157, 1994.

[15]   Y. B. He, W. Kriegseis, T. Krämer, A. Polity, M. Hardt, B. Szyszka, and B. K. Meyer, *Proceedings of ICTMC 13, to be published in J. Phys. Chem. Solids.*, 2003.

[16]   W. L. Zhong, Y. G. Wang, D. S. Kong, P. L. Zhang, and B. D. Qu, *Thin Solid Films*, vol. 237, p. 160, 1994.

[17]   K. Ishikawa, K. Yoshikawa, and N. Okada, *Phys. Rev. B*, vol. B 37, p. 5852, 1988.

[18]   R. Scheer and H. J. Lewerenz, *J. Vac. Sci. Technol. A*, vol. 12, p. 56, 1994.

[19]   L. D. Partain, R. A. Schneider, L. F. Donaghey, and P. S. Mcleod, *J. Appl. Phys.*, vol. 57, p. 5056, 1985.

[20]   R. Scheer and H. J. Lewerenz, *J. Vac. Sci. Technol. A*, vol. 12, p. 51, 1994.

[21]   W. Braun, A. Goldmann, and M. Cardona, *Phys. Rev. B*, vol. 10, p. 5069, 1974.

[22]   S. Kono and M. Okusawa, *J. Phys. Soc. Jpn.*, vol. 37, p. 1301, 1974.

[23]   J. E. Jaffe and A. Zunger, *Phys. Rev. B*, vol. 28, p. 5822, 1983.

[24]   R. Klenk, T. Walter, H. W. Schock, and D. Cahen, *Adv. Mater.*, vol. 5, p. 114, 1993.

[25]   R. Klenk, T. Walter, H. W. Schock, and D. Cahen, *Solid State Phenomena*, vol. 37-38, p. 509, 1994.

[26]   Y. B. He, I. Oesterreicher, T. Krämer, A. Polity, W. Kriegseis, B. K. Meyer, and M. Hardt, *Int. J. Mod. Phys. B*, vol. 16, p. 4380, 2002.

[27]   Y. B. He, T. Krämer, A. Polity, M. Hardt, and B. K. Meyer, *to be published in Inst. Phys. Conf. Ser.*, 2003.

[28]   S. Menezes, H. J. Lewerenz, and K. J. Bachmann, *Nature*, vol. 305, p. 615, 1983.

[29]   B. Lengeler, *Adv. X-Ray Anal.*, vol. 35, p. 127, 1992.

[30]   D. K. G. d. Boer, A. J. G. Leenaers, and W. W. v. d. Hoogenhof, *X-Ray Spectrometry*, vol. 24, p. 91, 1995.

[31]   Y. B. He, W. Kriegseis, J. Blaesing, A. Polity, T. Krämer, D. Hasselkamp, B. K. Meyer, M. Hardt, and A. Krost, *Jpn.J. Appl. Phys.*, vol. 41, p. 4630, 2002.

[32]   D. Cahen and R. Noufi, *Appl. Phys. Lett.*, vol. 54, p. 558, 1989.

[33]   J. Klaer, J. Bruns, R. Henninger, K. Siemer, R. Klenk, K. Ellmer, and D. Bräunig, *Semicond. Sci. Technol.*, vol. 13, p. 1456, 1998.

[34]   L. Y. Sun, L. L. Kazmerski, A. H. Clark, P. J. Ireland, and D. W. Morton, *J. Vac. Sci. Technol.*, vol. 15, p. 265, 1978.

[35]   Y. B. He, A. Polity, I. Oesterreicher, D. Pfisterer, R. Gregor, B. K. Meyer, and M. Hardt, *Physica B*, vol. 308-310, p. 1069, 2001.

Chapter 6

[1]   H. W. Schock and R. Noufi, *Prog. Photovoltaic. Res. Appl.*, vol. 8, p. 151, 2000.

[2]   C. H. Henry, *J. Appl. Phys.*, vol. 51, p. 4494, 1980.

[3]   S. Siebentritt, *Thin Solid Films*, vol. 403-404, p. 1, 2002.

[4]   B. Tell, J. L. Shay, and H. M. Kasper, *Phys. Rev. B*, vol. 4, p. 2463, 1971.

[5]   K. Siemer, J. Klaer, I. Luck, J. Bruns, R. Klenk, and D. Bräunig, *Solar Energy Mater. Solar Cells*, vol. 67, p. 159, 2001.

[6]   L. Stolt, J. Hedström, J. Kessler, M. Ruckh, K. O. Velthaus, and H. W. Schock, *Appl. Phys. Lett.*, vol. 62, p. 597, 1993.

[7]   M. A. Contreras, B. Egaas, K. Ramanathan, J. Hiltner, F. Hasoon, and R. Noufi, *Prog. Photovolt. Res. Appl.*, vol. 7, p. 311-316, 1999.

[8]   H. Metzner, T. Hahn, J. H. Bremer, and J. Conrad, *Applied Physics Letters*, vol. 69, p. 1900, 1996.

[9]   T. Hahn, H. Metzner, B. Plikat, and M. Seibt, *Appl. Phys. Lett.*, vol. 72, p. 2733, 1998.

[10]   R. Hunger, R. Scheer, K. Diesner, D. Su, and H. J. Lewerenz, *Appl. Phys. Lett.*, vol. 69, p. 3010, 1996.

[11]   S. F. Chichichu, T. Yoshida, T. Onuma, and H. Nakanishi, *J. Appl. Phys.*, vol. 91, p. 874, 2002.

[12]   M. Park, J.-p. Maria, J. J. Cuomo, Y. C. Chang, J. F. Muth, R. M. Kolbas, R. J. Nemanich, E. Carlson, and J. Bumgarner, *Appl. Phys. Lett.*, vol. 81, p. 1797, 2002.

[13]   H. Tang, J. B. Webb, S. Moisa, J. A. Bardwell, and S. Rolfe, *J. Crystal Growth*, vol. 244, p. 1, 2002.

[14]   C. B. Eom, A. F. Marshall, S. S. Laderman, R. D. Jacowitz, and T. H. Geballe, *Science*, vol. 249, p. 1549, 1990.

[15]   R. A. Rao, Q. Gan, C. B. Eom, Y. Suzuki, A. A. McDaniel, and J. W. P. Hsu, *Appl. Phys. Lett.*, vol. 69, p. 3911, 1996.

[16]   M. Ohkubo, J. Geerk, G. Linker, and O. Meyer, *Appl. Phys. Lett.*, vol. 67, p. 2403, 1995.

[17]   S. Horita, S. Horii, and S. Umemoto, *Jpn. J. Appl. Phys.*, vol. 37, p. 5141, 1998.

[18]   U. C. Oh, T. S. Kang, K. H. Park, and J. H. Je, *J. Appl. Phys.*, vol. 86, p. 163, 1999.

[19]   E. E. Fullerton, C. H. Sowers, J. P. Pearson, S. D. Bader, X. Z. Wu, and D. Lederman, *Appl. Phys. Lett.*, vol. 69, p. 2438, 1996.

[20]   E. E. Fullerton, J. S. Jiang, C. Rehm, C. H. Sowers, S. D. Bader, J. B. Patel, and X. Z. Wu, *Appl. Phys. Lett.*, vol. 71, p. 1579, 1997.

[21]   B. B. Kosicki and D. Kahng, *J. Vac. Sci. Technol.*, vol. 6, p. 593, 1969.

[22]   V. Kumar and B. S. R. Sastry, *J. Phys. Chem. Solids*, p. 107, 2002.

[23]   R. A. Rao, Q. Gan, and C. B. Eom, *Appl. Phys. Lett.*, vol. 71, p. 1171, 1997.

[24]   Y. B. He, W. Kriegseis, B. K. Meyer, A. Polity, and M. Serafin, *Submitted to Appl. Phys. Lett.*, 2003.

[25]   J. Cieslak, H. Metzner, T. Hahn, J. Kräusslich, U. Kaiser, U. Peislöhner, U. Grossner, and W. Witthuhn, *Proceedings of ICTMC 13. Oct. 14-18, Paris, France*, 2003.

[26]   R. Hunger, D. Su, A. Krost, D. Ellmer, H. J. Lewerenz, and R. Scheer, *Thin Solid Films*, vol. 361-362, p. 437, 2000.

Chapter 7

[1]   K. Ellmer, J. Hinze, and J. Klaer, *Thin Solid Films*, vol. 413, p. 92, 2002.

[2]   A. Zeuner, Diplom Thesis: I. Phys. Inst., Justus-Liebig University Giessen, 2003.

[3]   W. Zhang, Dissertation: I. Phys. Inst., Justus-Liebig University Giessen, 2001.

Publications

Parts of this Ph. D work have already been published. The papers 1-12 listed below are related to this work and 13-25 related to the work until 1999 in China.

1) <u>Y. B. He</u>, A. Polity, R. Gregor, D. Pfisterer, I. Österreicher, D. Hasselkamp, B. K. Meyer,
   Characterization of RF reactively sputtered Cu-In-S thin films,
   Physica B 308-310 (2001) 1074-1077.

2) <u>Y. B. He</u>, A. Polity, I. Österreicher, D. Pfisterer, R. Gregor, B. K. Meyer, and M. Hardt, Hall effect and surface characterization of Cu_2S and CuS films deposited by RF reactive sputtering,
   Physica B 308-310 (2001) 1069-1073.

3) <u>Y. B. He</u>, A. Polity, H. R. Alves, I. Österreicher, W. Kriegseis, D. Pfisterer, B. K. Meyer, and M. Hardt,
   Structural and optical characterization of RF reactively sputtered $CuInS_2$ thin films,
   Thin Solid Films 403-404 (2002) 62-65.

4) <u>Yunbin He</u>, Wilhelm Kriegseis, Jürgen Bläsing, Angelika Polity, Thorsten Krämer, Dietmar Hasselkamp, Bruno K. Meyer, Martin Hardt and Alois Krost,
   (001)-Textured Cu_2S Thin Films Deposited by RF Reactive Sputtering,
   Jpn. J. Appl. Phys. 41 (2002) 4630-4634.

5) <u>Yunbin He</u>, Thorsten Krämer, Ingo Österreicher, Angelika Polity, Ralf Gregor, Wilhelm Kriegseis, Dietmar Hasselkamp and Bruno K. Meyer,
   Highly (112)-Oriented $CuInS_2$ Thin Films Deposited by a One-Stage RF Reactive Sputtering Process,
   Jpn. J. Appl. Phys. 41 (2002) L 484-L 486.

6) <u>Yunbin He</u>, I. Österreicher, T. Krämer, A. Polity, W. Kriegseis and B. K. Meyer, M. Hardt,
   Surface and structural characterization of $CuInS_2$ thin films deposited by one-stage RF reactive sputtering,
   Int. J. Mod. Phys. B. 16 (2002) 4380-4386.

7) <u>Y. B. He</u>, T. Krämer, A. Polity, R. Gregor, W. Kriegseis, I. Österreicher, D. Hasselkamp, B. K. Meyer,

Preparation and characterization of highly (112) oriented $CuInS_2$ films deposited by a one-stage RF reactive sputtering process,

Thin Solid Films 431-432 (2003) 231-236.

8) <u>Y. B. He</u>, T. Krämer, A. Polity, M. Hardt, B. K. Meyer,

Influence of the preparation conditions on the properties of $CuInS_2$ films deposited by one-stage RF reactive sputtering,

Thin Solid Films 431-432 (2003) 126-130.

9) <u>Y. B. He</u>, T. Krämer, A. Polity, M. Hardt, B. K. Meyer,

Post-growth treatments on $CuInS_2$ thin films deposited by RF reactive sputtering, in:

Advanced Nanomaterials and Nanodevices (IUMRS-ICEM 2002, Xi'an, China, 10-14 June 2002), 927-942.

10) <u>Y. B. He</u>, W. Kriegseis, T. Krämer, A. Polity, M. Hardt, B. Szyszka, B. K. Meyer,

Deposition of $CuInS_2$ thin films by RF reactive sputtering with a ZnO:Al buffer layer,

J. Phys. Chem. Solids. 64 (2003) 2075-2079.

11) <u>Y. B. He</u>, W. Kriegseis, B. K. Meyer, A. Polity, and M. Serafin,

Heteroepitaxial growth of $CuInS_2$ thin films on sapphire by radio frequency reactive sputtering, ***Appl. Phys. Lett.*** 83 (2003) 1743-1745.

12) <u>Y. B. He</u>, A. Krost, J. Blaesing, W. Kriegseis, A. Polity, B. K. Meyer, C. Kisielowski,

Quasi-epitaxial growth of $CuInS_2$ films on sapphire by RF reactive sputtering,

Thin Solid Films 451-452 (2004) 229-232.

13) <u>Y. B. He</u>, T. S. Zhou, X. Z. Shang, J. Miao, A. X. Kuang,

Study on the preparation technology of manganese and stibium composition modified $PbTiO_3$ piezoelectric ceramics with large anisotropy (in Chinese),

Journal of Hubei University (Natural Science Edition), 1998, 20(4), 340-344.

14) <u>Y. B. He</u>, Y. M. Lu,

Discussion on mole heat capacity of ideal gas in polytropic process (in Chinese),

Journal of Higher Teachers Training Through Correspondence (Natural Science Edition), 1 (1999) 25-26.

15) <u>Y. B. He</u>, Y. M. Lu,

Pay attention to the limits for the integration of the state parameters (in Chinese),

Journal of Higher Teachers Training Through Correspondence (Natural Science Edition), 3 (1999) 9-10.

16) <u>Y. B. He</u>, J. Miao, T. S. Zhou, X. Z. Shang, Y. W. Zhang, A. X. Kuang,
Design and studies of modified $PbTiO_3$ piezoelectric ceramics with large anisotropy (in Chinese),
Journal of Hubei University (Natural Science Edition), 1999, 21(3), 244-248.

17) <u>Y. B. He</u>, W. Pen, T. S. Zhou, A. X. Kuang,
The research and development of modified $PbTiO_3$ piezoelectric ceramics with large anisotropy (in Chinese),
Journal of Hubei University (Natural Science Edition), 1999, 21(4), 338-344.

18) T. S. Zhou, <u>Y. B. He</u>, X. Z. Shang, Y. W. Zhang, A. X. Kuang,
Studies on a new type of $PbTiO_3$ piezoelectric ceramic materials,
Ferroelectrics, 229 (1999) 261-265.

19) T. S. Zhou, <u>Y. B. He</u>, X. Z. Shang, Y. W. Zhang, A. X. Kuang,
A new modified $PbTiO_3$ piezoelectric ceramic material (in Chinese),
Journal of Inorganic Materials, 1998, 13(4), 484-490.

20) T. S. Zhou, <u>Y. B. He</u>, A. X. Kuang,
Working principle of a piezoelectric ultrasonic motor (in Chinese),
Journal of Hubei University (Natural Science Edition), 1998, 20(3), 246-249.

21) T. S. Zhou, L. Y. Chai, C. X. He, <u>Y. B. He</u>, A. X. Kuang,
A standing wave type ultrasonic motor,
Ferroelectrics, 232 (1999) 253-257.

22) T. S. Zhou, S. M. Wang, D. H. Bao, <u>Y. B. He</u>, A. X. Kuang,
Correlation and comprehensive selection of the piezoelectric ignition material parameters,
Ferroelectrics, 195 (1997) 97-100.

23) T. S. Zhou, S. M. Wang, H. S. Gu, <u>Y. B. He</u>, A. X. Kuang,
The effect of doping Sb_2O_3 in high $d_{33}.g_{33}$ PZT piezoelectric ceramics,
Ferroelectrics, 195 (1997) 101-104.

24) X. Z. Shang, Y. W. Zhang, T. S. Zhou, <u>Y. B. He</u>, L. Y. Chai, A. X. Kuang,
Preparation of a material for piezoelectric ceramic step-down transformer (in

Chinese), *Journal of Hubei University* (Natural Science Edition), 1999, 21(3), 249-252.

25) T. S. Zhou, C. X. He, L. Y. Chai, A. X. Kuang, <u>Y. B. He</u>,
A new type of polarization unit for piezoelectric ceramics (in Chinese),
Electronic Components & Materials, 1997, 16(2), 50-53.

Curriculum vitae

Yunbin He, born on April 24, 1972, in Suizhou, Hubei, China.

Sept. 1979-Jul.1990	Primary and secondary school, Suizhou, Hubei
Sept. 1990-Jul. 1994	Bachelor of Physics, Hubei University, Wuhan, Hubei
Sept. 1994-Jul. 1997	Master of Material Science, Hubei University, Wuhan, Hubei. Master thesis: Studies on a new type of modified $PbTiO_3$ piezoelectric ceramic with high performances
Sept. 1997-Jan. 1998	Teaching Electroceramics Physics in the college of Physics and Electronic Technology, Hubei University, Wuhan, Hubei
Feb. 1998-July. 1998	Professional training on Semiconductor Physics, Huazhong University of Science and Technology
Sept. 1998-Sept. 1999	Teaching Advanced Mathematics and Semiconductor Physics in the college of Physics and Electronic Technology, Hubei University, Wuhan, Hubei
Since Oct. 1999	Ph. D student at the First Physics Institute of Giessen University, Giessen, Germany

Acknowledgements

I gratefully acknowledge all the people who contributed directly or indirectly to the accomplishment of this Ph. D work.

My greatest debt is to my advisor, Prof. Dr. Bruno. K. Meyer, who provided me the opportunity to work in his group, studying photovoltaic absorber materials, an interesting subject of great fundamental and technical importance. Under his leadership, I have been enabled to work in an active group with open and friendly atmosphere. Many opportunities he gave me to go out for the academic exchanges have stimulated many of my research interests, and enabled me to accumulate more experiences in my scientific career. He always stood by me at times of difficulty, encouraging me and showing his confidence in me. I learnt from him not only his extensive knowledge in physics and plenty of brilliant and creative ideas, but also his strict academic attitude and fair research philosophy for dealing with scientific problems, which will have influences on my whole life of scientific career. Every time of long discussion in the "Blue Saloon" has been an ever-good memory in my life. Bruno is a strict boss in science but a kindest friend in life. He helped me to invite my wife to come to Germany, getting my family reunited. He always took care of my life and health, reminding me several times for vacation. Although at the moment words are too limited to express my gratitude, I still like to say, − "Bruno, thanks a lot!"

I am deeply grateful to my group leader, Privatdozent Dr. Angelika Polity, whose detailed supervision and continuous supports laid a smooth way for my studies. From the beginning of detailed experimental work, uncountable discussions, to the final corrections of the dissertation, especially in editing of the Deutsche Zusammenfassung, she has given essential constructive and indispensable input to this dissertation. Her intrinsic carefulness and patience led to all my papers and this dissertation of much less errors and more readable. She also helped me in solving many daily life problems caused by my lacking of the knowledge of German language. Working with Angelika, sharing her fairness, intelligence, and creative ideas, is indeed an unforgotten experience in my life.

I am particularly thankful to Dr. Wilhelm Kriegseis, who has been my English tutor besides guidance in scientific aspects and SIMS measurements of my samples. He read and corrected several of my papers, especially proofreading of this dissertation, with sharp eyes and rigorous control, leading to all them certainly of much higher quality. Discussion with Willi, enabled me to learn much more about German culture and spirits, beyond German science. Willi's generous friendship, great patience, and rigorous academic attitude impressed me deeply!